

**Electronic Structure and Quantum Conductance  
of Molecular and Nano Electronics**

by

Elise Yu-Tzu Li

B.S., Chemistry National Taiwan University (2005)

Submitted to the Department of Chemistry  
in partial fulfillment of the requirements for the degree of

Doctor of Philosophy

at the

MASSACHUSETTS INSTITUTE OF TECHNOLOGY

June 2011

© Massachusetts Institute of Technology 2011. All rights reserved.

Author .....

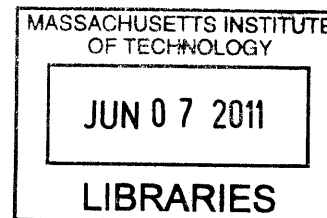
Department of Chemistry  
May 17, 2011

Certified by .....

Nicola Marzari  
Associate Professor of Materials Science and Engineering  
Thesis Supervisor

Accepted by .....

Robert W. Field  
Chairman, Department Committee on Graduate Theses



**ARCHIVES**

This doctoral thesis has been examined by a Committee of the Department of Chemistry as follows:

Professor Troy Van Voorhis . . . . .

Chairman, Thesis committee  
Associate Professor of Chemistry

Professor Nicola Marzari . . . . .

Thesis Supervisor  
Associate Professor of Materials Science and Engineering

Professor Mounqi Bawendi . . . . .

Member, Thesis committee  
Lester Wolfe Professor of Chemistry

# Electronic Structure and Quantum Conductance of Molecular and Nano Electronics

by

Elise Yu-Tzu Li

Submitted to the Department of Chemistry  
on May 17, 2011, in partial fulfillment of the  
requirements for the degree of  
Doctor of Philosophy

## Abstract

This thesis is dedicated to the application of a large-scale first-principles approach to study the electronic structure and quantum conductance of realistic nanomaterials. Three systems are studied using Landauer formalism, Green's function technique and maximally localized Wannier functions. The main focus of this thesis lies on clarifying the effect of chemical modifications on electron transport at the nanoscale, as well as on predicting and designing new type of molecular and nanoelectronic devices.

In the first study, we suggest and investigate a quantum interference effect in the porphyrin family molecules. We show that the transmission through a porphyrin molecule at or near the Fermi level varies by orders of magnitude following hydrogen tautomerization. The switching behavior identified in porphyrins implies new application directions in single molecular devices and molecular-size memory elements.

Moving on from single molecules to a larger scale, we study the effect of chemical functionalizations to the transport properties of carbon nanotubes. We propose several covalent functionalization schemes for carbon nanotubes which display switchable on/off conductance in metallic tubes. The switching action is achieved by reversible control of bond-cleavage chemistry in [1+2] cycloadditions, via the  $sp^3 \rightleftharpoons sp^2$  rehybridization it induces; this leads to remarkable changes of conductance even at very low degrees of functionalization. Several strategies for real-time control on the conductance of carbon nanotubes are then proposed. Such designer functional groups would allow for the first time direct control of the electrical properties of metallic carbon nanotubes, with extensive applications in nanoscale devices.

In the last part of the thesis we address the issue of low electrical conductivity observed in carbon nanotube networks. We characterize intertube tunneling between carbon nanotube junctions with or without a covalent linker, and explore the possibility of improving intertube coupling and enhance electrical tunneling by transition metal adsorptions on CNT surfaces. The strong hybridization between transition

metal  $d$  orbitals with the CNT  $\pi$  orbitals serves as an excellent electrical bridge for a broken carbon nanotube junction. The binding and coupling between a transition metal atom and sandwiching nanotubes can be even stronger in case of nitrogen-doped carbon nanotubes. Our studies suggest a more effective strategy than the current cross-linking methods used in carbon nanotube networks.

Thesis Supervisor: Nicola Marzari

Title: Associate Professor of Materials Science and Engineering



## Acknowledgments

First and foremost I would like to thank my thesis advisor, Prof. Nicola Marzari, for his kindness, trust, and freedom he offered during the course of my study which has helped me to become, I hope, an independent and honest researcher. I want to thank my committee members, Prof. Troy Van Voorhis and Prof. Mounji Bawendi, for their generous support when I was working in a research group outside the Department of Chemistry.

I will not forget the good old days I spent with the Quasiamore group. I would like to thank our group members: Jivtesh Garg, Nicolas Poilvert, Nicéphore Bonnet, Sejoong Kim, Nicholas Miller, Matteo Salvetti, Nicola Bonini, Oliviero Andreussi, Davide Ceresoli, Andrea Ferretti, Xiaofeng Qian, Dimitri Volja, and Samed Halilov, for being great colleagues and friends. I am indebted to Davide, Sejoong, Andrea, Xiaofeng, and Nicolas for their generous and patient help whenever I encountered a problem I couldn't solve.

I want to thank my best friends here: Amy, Yi-Chun, Liang-Yi, Tsao-Hsien, Carl, Shih-Wei, Chun-Hsiang, Hsui-Yi, Kevin, Yu-Chung, Sidney, Scott, Sam(s) and Lee-Ping who shared my tears and laughter. The list could go on and on and exceed the mere pages I have. The countless evenings we spent together with authentic Taiwanese meals and "insider jokes" have kept my heart so warm even in the coldest winter in Boston.

I can not express my deep gratitude in words to my parents and my sweet sister. Their boundless love and blessings were the source of my courage to sustain my impossible life in MIT. I cherish those long phone conversations, the advice and consolation that they never failed to provide on time, and even the heated debate about the people and feelings we all care so much.

And finally I must thank my most understanding and supportive husband, Shao-Yu. Throughout the years of our long separation, we have learned to appreciate the true value of trust and commitment. I love you.

# Contents

<b>1</b>	<b>Introduction</b>	<b>19</b>
<b>2</b>	<b>Fundamentals of Electronic Structure Theory</b>	<b>23</b>
2.1	Wavefunction methods . . . . .	25
2.1.1	Hartree-Fock theory . . . . .	25
2.1.2	Post Hartree-Fock methods . . . . .	29
2.2	Density methods . . . . .	33
2.2.1	Density functional theory . . . . .	34
2.2.2	Practical implementations of DFT . . . . .	37
2.3	Maximally localized wannier functions . . . . .	41
2.3.1	Localization procedure . . . . .	42
2.3.2	Disentanglement . . . . .	43
2.3.3	Real-space Hamiltonians . . . . .	44
<b>3</b>	<b>Quantum Transport Theory</b>	<b>45</b>
3.1	Landauer Formalism for Phase Coherent Transport . . . . .	46
3.1.1	Quantum Scattering Theory . . . . .	46
3.1.2	Current from transmission . . . . .	49
3.2	Green's Function Method in a Localized Basis Set . . . . .	50
3.2.1	Green's function method for extended systems . . . . .	51
3.2.2	The principal-layer approach for semi-infinite leads . . . . .	53
3.2.3	The surface Green's function . . . . .	54
3.2.4	Transmission probability in the Greens' function representation	56

3.2.5	Eigenchannel analysis . . . . .	59
<b>4</b>	<b>Quantum Interference Effect and Conductance Switching of Porphyrins Controlled by Hydrogen Tautomerization</b>	<b>63</b>
4.1	Quantum interference effect in single molecule transport . . . . .	63
4.1.1	The orbital view interpretation . . . . .	64
4.1.2	Molecular conductance orbital analysis . . . . .	66
4.2	Quantum interference effect in porphyrins . . . . .	68
4.2.1	Transport properties of porphyrin family molecules . . . . .	70
4.2.2	Porphyrins assembled between carbon nanotubes . . . . .	74
4.3	Porphyrin as a molecular bit . . . . .	77
<b>5</b>	<b>Conductance Switching in Functionalized Carbon Nanotubes <i>via</i> Reversible Sidewall Bond Cleavage</b>	<b>81</b>
5.1	Electrical conductivities in functionalized carbon nanotubes . . . . .	81
5.2	Mechanisms for closed-bond stabilization in [1+2] cycloaddition functionalization . . . . .	83
5.2.1	Unsaturated addend orientation effect . . . . .	85
5.2.2	Periconjugation effect . . . . .	87
5.2.3	CNT curvature effect and the bent-graphene model . . . . .	91
5.3	Conduction Switching on Functionalized Carbon Nanotubes . . . . .	95
5.3.1	Switching <i>via</i> chemical reactions . . . . .	95
5.3.2	Switching <i>via</i> optical excitations . . . . .	97
5.3.3	Switching <i>via</i> quinone-quinol transformation . . . . .	99
5.4	Quantum conductance of functionalized CNTs . . . . .	99
5.4.1	Singly functionalized CNTs . . . . .	99
5.4.2	Multiply functionalized CNTs . . . . .	100
<b>6</b>	<b>Improved Intertube Electrical Conductivity of Carbon Nanotube Networks Cross-Linked by Transition Metals</b>	<b>105</b>
6.1	Electrical conductivities in CNT networks . . . . .	105

6.2	Intertube conductivity of the polyacene model . . . . .	107
6.2.1	Band structure of the polyacene model . . . . .	107
6.2.2	Intertube tunneling without linkers . . . . .	109
6.2.3	Intertube tunneling with covalent linkers . . . . .	109
6.2.4	Intertube tunneling with transition metal coupling . . . . .	111
6.3	Intertube conductivity of carbon nanotubes . . . . .	113
6.3.1	Carbon nanotube junctions cross-linked by transition metals .	113
6.3.2	Nitrogen doped carbon nanotube junctions cross-linked by tran- sition metals . . . . .	118
<b>7</b>	<b>Conclusions</b>	<b>125</b>



# List of Figures

4-1	Transmission of the benzene molecule calculated within the Hückel model with different electrode connections. The on-site energies and the hopping terms for the $p_z$ orbitals are set to 0.0 and -0.5 eV, respectively. The coupling element between the lead and the molecule is also set to be -0.5 eV. . . . .	64
4-2	Frontier orbitals of benzene and symmetry-allowed/forbidden routes for electron transmission. . . . .	66
4-3	The porphyrin family molecules:(a) porphyrin (b) tetrabenzoporphyrin and (c) naphthalocyanin considered in this study. Also shown here are the HOMO-LUMO gaps calculated with the PBE functional and 30/360 Ry cutoffs for plane wave basis. It has been shown that the hydrogen tautomerization of (c) can be controlled by a STM tip. . . .	69
4-4	(a) the connection sites of porphyrin to the left or right electrodes considered in this study and (b) the positions and wavefunctions of the frontier molecular orbitals of porphyrin. . . . .	70
4-5	Selected orbitals of the MLWF basis of porphyrin. An $s$ -like orbital is located in the middle of all $\sigma$ bonds and a $p_z$ orbital are recovered for all carbon atoms, as well as the nitrogen atoms in the pyrrole moiety. For the other pair of nitrogen atoms involved in $\pi$ molecular orbitals, the $p_z$ orbital is found to hybridize with the long pair and give rise to two $sp^3$ like orbitals. . . . .	72

4-6	Transmission spectra calculated for (a) porphyrin (b) tetrabenzoporphyrin and (c) naphthalocyanin molecules with lead treated by WBL approximation and $\gamma_{L,R} = 0.5$ eV. The linkage sites for different paths are labeled in Fig. 4-4(a). The midgap Fermi level is marked by the dashed vertical line. . . . .	73
4-7	The real(top) and imaginary(bottom) contributions to the transmission from frontier molecular conductance orbitals of porphyrin linked to the leads through <i>AD</i> - (left) or <i>BE</i> path (right). The black curves are the sum of all contributions from all molecular conductance orbitals, and the contributions from HOMO-1(red), HOMO(green), LUMO(blue) to LUMO+1(orange) are shown in dashed curves. . . . .	75
4-8	The top view and side view of optimized structures for (5,5)CNT-porphyrin-(5,5)CNT through (a) <i>AB</i> -path (or <i>BD</i> -path in case of hydrogen tautomerization inside the porphyrin) and (b) <i>AD</i> -path (or <i>BE</i> -path for hydrogen tautomerized porphyrin) The strong coupling between the and the porphyrin $\pi$ orbital and the CNT $p_z$ orbitals is indicated by the red bond. . . . .	76
4-9	The transmission functions of (5,5)CNT-porphyrin-(5,5)CNT junctions with different linkage configurations from full DFT calculations and the lead self-energy treated atomistically. The corresponding curves of the same configurations calculated with only the porphyrin molecule and the lead part treated by wide-band-limit approximation are shown in dashed curves. . . . .	78
4-10	A 2-bit tape porphyrin system representing the "01" memory state ("0" and "1" for the hydrogen configuration for the left and right porphyrins, respectively). . . . .	79
4-11	The transmission functions of four different memory states of the 2-bit tape porphyrin via different linkage sites as shown in Fig. 4-10 . . . .	79



5-1	Two possible contributing effects for closed CNT sidewall bond stabilization: (a) through bond $\sigma$ - $\pi$ interaction in cyclopropane and (b) through space $\pi$ - $\pi$ periconjugation in quinone-type methanofullerene .	85
5-2	The molecular homologues of a functionalized CNT: 1,6-derivatized naphthalene ( <b>1</b> ) and pyrene ( <b>2</b> ). The bond length between the bridgehead carbon atoms $d_{16}$ depends primarily on the identity of the addend $X$ . The similarity between the local structure of a [1+2] cycloaddition functionalized CNT and the <b>2</b> is also shown. . . . .	86
5-3	Potential energy surface as a function of $d_{16}$ for <b>2</b> with $X=C(CHO)_2$ in different conformations. The closed-bond configuration is stabilized more when the C=O double bonds are closer to the pyrene backbone in the constrained perpendicular "O side" orientation. . . . .	87
5-4	Potential energy surface as a function of $d_{16}$ for (a) <b>1</b> (b) <b>2</b> functionalized with ring substituents. The zeros are set at $d_{16}=2.20 \text{ \AA}$ to mark the release of roughly same strain energy. . . . .	88
5-5	Walsh diagram along $d_{16}$ of <b>1</b> for systems (a) without and (b) with periconjugation. The equilibrium bond lengths are also marked. The dashed curve in (b) is an orbital in the same energy window but with the density mostly located on the substituent and should be safely left out of discussion. . . . .	89
5-6	(a) Potential energy surface as a function of $d_{16}$ for <b>1</b> with $X=C(CH_3)_2$ in staggered and eclipsed conformations. The frontier orbitals of two conformers at $d_{16} = 1.6 \text{ \AA}$ are also shown here. . . . .	90
5-7	Potential energy surface as a function of sidewall bond length $d_{16}$ for CNT and bent-graphene with (a) $X=CH_2$ and (b) $X=C(CN)_2$ . The carbon backbone of the bent graphene nanoribbon is taken from CNTs with different curvatures. The edge carbon atoms (hydrogenated carbons) are kept fixed in later relaxations to preserve the curvature. . .	93
5-8	Sidewall equilibrium bond distance $C_1-C_6$ ( $d_{16}$ ) for bent graphenes representing (n,n) CNTs . . . . .	94

5-9	Proposed conductance switching mechanism in functionalized armchair CNTs. The addends are attached to the C-C bonds perpendicular to the CNT axis labeled on the bottom of the figure. . . . .	96
5-10	Relaxed structures of a functionalized (6,6) CNT with (a) lactone and free carboxyl groups shown in Fig. 5-9(a) and (b) diketone and diol addends shown in Fig. 5-9(b). The CNT sidewall bond is closed with the lactone or diketone substituent, and is open with free carboxyl groups or diol addends. . . . .	97
5-11	Potential energy surface as a function of $d_{16}$ for (5,5)-, (6,6)-, or (8,8) bent graphenes functionalized with X=cis- or trans-cyclopentadiimine. The relaxed structure of functionalized (6,6) bent graphene in the equilibrium bond length are also shown. . . . .	98
5-12	Proposed conductance switching mechanism by tuning the intramolecular hydrogen bonding between the quinol and the cyclopentadione moiety. On a (6,6) CNT, the hydrogen bonded addend (in the middle) shall render the CNT sidewall bond open, while removal of the hydrogen bonds will induce a bond closure. . . . .	100
5-13	Quantum conductance of an infinitely long (6,6) carbon nanotube with a single functionalization. The solid lines correspond to the lactone/acid addend pair and the dashed lines correspond to the diketone/diol addend pair. The red color are for the "open" (acid and diol) and the black color are for the "closed" (lactone and diketone) conformations. The quantum conductance of the pristine tube is also given in the brown dashed line as a reference. The quantum conductance depends more on the "open" or "closed" conformations rather than on the specific addend identity in a wide energy range around the Fermi energy. . . . .	101
5-14	Illustration of the methodology used to construct Hamiltonian matrices for large disordered functionalized carbon nanotubes. Shown here is a carbon nanotube functionalized with 5 groups. The computed quantum conductance is an average from 20 different configurations. . . . .	102

5-15	Average quantum conductance (in units of $2e^2/h$ ) of 20 randomly functionalized (6,6) carbon nanotubes with 10, 20 or 30 addends. Both types of addends are considered (ketone in black and diol in red). Inside a given set of conductance curves (black or red), the highest curve represents 10 addends and the lowest curve represents 30 addends. The quantum conductance of a pristine (6,6) carbon nanotube is given in dashed line as a reference. . . . .	103
5-16	Visualization of (a) the “ $p_z$ ”-like Wannier orbitals in the “open” conformation and (b) the “ $\sigma$ ”-like orbital in the “closed” conformation in the diketone/diol addend pair. The strong scattering introduced in the “closed” conformation is caused by the disappearance of the two $p_z$ Wannier orbitals, which disrupts the $\pi$ manifold of the CNT. . . .	104
6-1	The band structure, quantum conductance, and density of states of pristine polyacene. The wannier function interpolated band structure and density of states are shown in red circles and red dashed lines, respectively. The solid curves are calculated from full plane-wave basis calculation. . . . .	108
6-2	The quantum conductance of a broken polyacene junction bridged by (a) a pentacene molecule with varying adsorption distance (b) different nanoribbon fragments in which the adsorption distance is fixed as $3\text{\AA}$	110
6-3	The quantum conductance of a broken polyacene junction bridged by a covalent pyrazene-nitrene linker . . . . .	111
6-4	The quantum conductance of A). a pristine polyacene scattered by a bis(benzene)chromium defect, B). a broken polyacene junction bridged by a chromium atom, and C). a broken polyacene junction bridged by an adsorbed pentacene and two sandwiched chromium atoms. . . . .	112

6-5	(a) The eigenchannel decomposition and the density of corresponding eigenchannels of quantum conductance of configuration B in Fig. 6-4 near the Fermi level; (b) The energy and frontier molecular orbitals of bis(benzene)chromium. . . . .	113
6-6	The (a) spin up and (b) spin down quantum conductance near the Fermi level of a (5,5)-CNT scattered by a single first-row transition metal adsorption (in the configuration of the left of Table 6.1. The quantum conductance of a pristine (5,5) CNT is shown in the black dashed curve. . . . .	117
6-7	Quantum conductance near the Fermi level of a (5,5)-CNT junction connected by a 3d transition metal. The quantum conductance of the same junction without the transition metal is shown in the "no TM" curve, with the geometry directly taken from the CNT-Cr-CNT structure by removing the central Cr atom, to show the contribution of through space tunneling between the $\pi$ orbitals unassisted by TM coordination. . . . .	118
6-8	The (a) spin up and (b) spin down quantum conductance near the Fermi level of a (5,5)-CN <sub>x</sub> NT scattered by a single first-row transition metal adsorption (in the configuration of the left of Table 6.2. The quantum conductance of a pristine (5,5) CNT is shown in the black dashed curve; the quantum conductance of a (5,5) CN <sub>x</sub> NT is shown in the black dotted curve. . . . .	120
6-9	Quantum conductance near the Fermi level of a (5,5)-CNT junction connected by a 3d transition metal. The quantum conductance of a pristine (5,5) CNT is shown in the black dashed curve. . . . .	121

# List of Tables

4.1	The equivalent paths of porphyrin-family molecules and their interconverting relationships upon hydrogen tautomerization . . . . .	72
6.1	Calculated binding energies ( $E_b^1$ , $E_b^2$ as defined in Eq. 6.1 and Eq. 6.2), average carbon-TM atom distances ( $d_{TM-C}$ ), and the absolute magnetization per unit cell $\mu_B$ (the number of unpaired electrons is listed inside the parenthesis) of a single TM atom adsorbed on (Left): the surface of a (5,5) CNT or (Right): between two (5,5) CNTs. . . .	115
6.2	Calculated binding energies ( $E_b^1$ , $E_b^2$ as defined in Eq. 6.1 and Eq. 6.2), average nitrogen-TM atom distances ( $d_{TM-N}$ ), and the absolute magnetization per unit cell $\mu_B$ (the number of unpaired electrons is listed inside the parenthesis) of a single TM atom adsorbed on (Left): the surface of a (5,5) $CN_xNT$ or (Right): between two (5,5) $CN_xNT$ s. . . .	119



# Chapter 1

## Introduction

Molecular electronics is an emerging field of research aiming at replacing traditional semiconductor circuitry with individual molecules, which are hundreds of times smaller and could circumvent the ultimate limitations of silicon-based device miniaturization. The idea of using single molecules as discrete electronic building blocks, initiated by the proposal of a single molecular rectifier [1], has attracted increasing attention during the past decades, and to date numerous single molecule electronic devices have been constructed [2, 3, 4]. Experimentally, a primitive metal-molecule-metal (MMM) configuration is usually realized by methods of MCBJ (mechanically controllable break junction) [5], c-AFM (conductive atomic force microscopy) [6], or STM (scanning tunneling microscopy) [7].

Despite the enthusiasm and effort invested in the field, molecular electronics is still far from any industrial application. Current issues for the realization of molecular electronics include the development of reproducible and robust experimental setups. In recent reviews [8] it was shown that the experimental measurements of the same system could easily differ by several orders of magnitude [9]. The variation in the measured conductance of molecular junctions mainly comes from the difference of local structures of the metal-molecule (typically Au-S linkage) contact in different junctions. Due to the lack of specific chemistry between the metal electrode and the linker group of the molecule, it is extremely difficult to fabricate a well-defined

metal-molecule contact in real experiments.

Single wall carbon nanotubes (CNTs) present an attractive alternative for single-molecule junctions. The 1-D ballistic transport property in metallic CNTs implies low power dissipation over long distances. Their stable chemical structure and strong covalent bonds allow for high mechanical and thermal stability, and the use of CNTs as molecular contacts avoids the problems associated with metal electrodes using thiol chemistry. The molecule can be connected to the CNT electrode by a covalent bond and the attachment chemistry is well defined. It is now possible to fabricate a CNT-molecule-CNT contact structure by precise oxidative cutting of a CNT followed by molecular bridge formation via amide linkages [10]. One experimental focus is now dedicated to synthetic strategies to couple the  $\pi$  system in the CNT directly to the  $\pi$  system of the conducting molecule for good contact transparency. From the application point of view, the CNT electrodes are of the same physical scale as the conducting molecules, which is essential for future molecular scale electronics.

The past twenty years have witnessed multiple experimental breakthroughs of single molecule electronics; in the meanwhile, the theory of electronic transport in mesoscopic systems has also flourished [11, 12]. Extensive theoretical studies have been carried out on metal-molecule-metal junctions [13, 14], providing an in-depth understanding of the coupling between individual molecular structures to macroscopic electrodes. Theoretical transport calculations have been shown to play an important role in clearing up uncertainties and providing direct links between the measured electrical conductivities and atomic-scale details. Nevertheless, the real power of theoretical studies is nothing but their capability to predict undiscovered properties, to design novel nanoelectronic elements, and to screen vast number of systems before tedious experimental work is attempted.

The main theme of this thesis is electron transport in nanoscale materials, and in particular carbon-nanotube electronic devices. The outline of this thesis is the follow-



ing: Chapter 1 provides the background knowledge this thesis is based on. Chapter 2 reviews the fundamentals of the electronic structure theory and the machinery of the most widely used, state-of-the-art first-principles method, *i.e.* the density functional theory. Chapter 3 introduces the basics of quantum transport theory, the Landauer approach, and the Green's function method for treating an open, infinite system such as the lead-molecule-lead junctions that we are interested in.

The major part of the thesis is devoted to the application of quantum transport theory to various systems ranging from single molecules to nanocomposite matrices. We are mainly interested in the effect of chemistry modifications and the capability to control molecular functionalities. The motivation for theoretical studies on molecular transport, other than providing explanations to experimental observations, is to acquire further insight into the mechanisms of electron transport and to help design new types of molecular devices. In Chapter 4 we study the intriguing phenomenon that has been a recent focus in molecular electronics: *the quantum interference effect*, which stresses the significant difference between electron transport through nanoscale molecular devices and that through macroscopic structures, and what interesting and unexpected event could appear when one moves into a smaller and smaller world, and constructive and destructive interference phenomena start playing a major role in electrical transports. In Chapter 5 we explore the possibility of controlling the conductivity of CNTs via covalent functionalization and identified a novel through-space interaction between carbon nanotube surface and aromatic functional groups. In Chapter 6 we investigate a relatively unexplored topic: the effect of transition metal adsorption on CNT transport. We apply this to improve the low intertube conductivity of CNT networks, which is an important issue in electronic devices based on SWNT thin films. The work in this thesis demonstrates how chemistry at the atomistic scale could affect electron transport even at the macroscopic scale, and suggests novel approaches toward conductance modulation for single-molecular and carbon-nanotube based nanoelectronics.



## Chapter 2

# Fundamentals of Electronic Structure Theory

### Introduction

It is now clear that almost all natural phenomena we experience everyday are a result of interactions of various molecules and that molecules are composed by even more basic tiny particles called atoms. The abstract concept of a chemical “bond” enables one to visualize in one’s mind how atoms are held together by an electronic “glue”. Indeed all mechanical, thermal, optical, magnetic or any other unique properties one can think of about a material are derived from the interactions between various nuclei and electrons in atoms or molecules. The interactions were made computable with the emergence of electronic-structure theory, thanks to the invention of a whole new discipline, quantum mechanics, which describes systems at infinitesimal space and time scales.

At the heart of electronic-structure theory lies the fundamental law of quantum mechanics, the time-independent Schrödinger equation

$$\hat{H}\Psi(\{\mathbf{r}_i\}, \{\mathbf{R}_I\}) = E\Psi(\{\mathbf{r}_i\}, \{\mathbf{R}_I\}) \quad (2.1)$$

where the system is described by an antisymmetric wavefunction  $\Psi$ , a function that depends on both the coordinates of the nuclei  $\{\mathbf{R}_I\}$  and the electrons  $\{\mathbf{r}_i\}$ . The Hamiltonian  $\hat{H}$  operates on the wavefunction to give the total energy  $E$  of the system. The problem can be further simplified according to Born-Oppenheimer approximation, which separates the nucleus and electronic degrees of freedom and allows one to study the electronic behavior while considering the ionic positions at rest as parameters:

$$\Psi(\{\mathbf{r}_i\}, \{\mathbf{R}_I\}) = \Phi(\{\mathbf{R}_I\})\Psi_R(\{\mathbf{r}_i\}) \quad (2.2)$$

The Hamiltonian for a system containing  $N$  electrons includes the kinetic energy of the electrons  $\hat{T}_e$ , the attractive Coulomb energy between the electrons and the nuclei  $\hat{V}_{ne}$ , the Coulomb repulsion between electron pairs  $\hat{V}_{ee}$  and finally, the coulomb repulsion between the positively charged nuclei  $\hat{W}_{nn}$ <sup>1</sup>:

$$\hat{H} = \hat{T}_e + \hat{V}_{ne} + \hat{V}_{ee} + \hat{W}_{nn} = \sum_i^N \left( -\frac{1}{2} \nabla_i^2 + v(\mathbf{r}_i) \right) + \sum_{i < j}^N \frac{1}{|\mathbf{r}_i - \mathbf{r}_j|} + \hat{W}_{nn} \quad (2.3)$$

$$v(r_i) = - \sum_I \frac{Z_I}{|\mathbf{r}_i - \mathbf{R}_I|} \quad (2.4)$$

$$\hat{W}_{nn} = \frac{1}{2} \sum_{I < J} \frac{Z_I Z_J}{|\mathbf{R}_I - \mathbf{R}_J|} \quad (2.5)$$

Under the assumptions of quantum mechanics, all physical properties can be derived from the ground state wavefunction. In practice, however, solving the Schrödinger equation is a formidable task as the motion of electrons are intercorrelated to each other. As a result, the problem is equivalent to solving a set of heavily coupled nonlinear integro-differential equations, and in fact, no exact solutions exist once one goes beyond one-electron systems, that is to say, except for the H atom, H<sub>2</sub><sup>+</sup> molecular ion, and a few other simplest systems, one has to rely on various approximations which usually involve variational minimization of the total energy to obtain the ground state energy and wavefunction. These approximations typically fall into two broad

---

<sup>1</sup>Throughout this chapter atomic units are used:  $\hbar = m_e = 4\pi\epsilon_0 = 1$

categories housed under the roof of wavefunction methods and density methods. This chapter aims at offering a brief overall introduction of the two distinct methods used in the following studies in this thesis; more details can be found *e.g.* in the books of Szabo and Ostlund [15], Parr and Yang [16], and Koch and Holthausen [17].

## 2.1 Wavefunction methods

### 2.1.1 Hartree-Fock theory

Wavefunction methods, as the name suggests, focus on solving for the ground state wavefunctions explicitly, and most often start from Hartree-Fock (HF) theory. In reality, the electronic wavefunction for  $N$  electrons is a highly complex function that depends on  $3N$  coordinates and the exact form is not known. Central to Hartree-Fock theory is the assumption of searching for an approximate solution in the form of a Slater determinant of single-particle spin orbitals  $\phi_i$ , which represents one and maybe the simplest way of satisfying the antisymmetry requirement and Pauli exclusion principle:

$$\begin{aligned} \Psi(r_1\sigma_1, r_2\sigma_2, \dots, r_N\sigma_N) &= |\phi(r_1\sigma_1)\phi(r_2\sigma_2)\dots\phi(r_N\sigma_N)\rangle \\ &= \frac{1}{\sqrt{N!}}(-1)^P \sum_P P[\phi(r_1\sigma_i)\phi(r_2\sigma_2)\dots\phi(r_N\sigma_N)] \quad (2.6) \end{aligned}$$

where  $r$  and  $\sigma$  denote the space and spin coordinates of the electrons, respectively, and  $P$  is a permutation operator that operates on the spin orbital product such that upon any exchange between two particles, the spin orbital product takes up an additional minus sign.

With this assumption at hand and some mathematical manipulations, the energy calculated from the expectation value of the electronic Hamiltonian can then be written as:

$$\begin{aligned}
E &= \langle \Psi(r_1\sigma_1, r_2\sigma_2, \dots, r_N\sigma_N) | H_e | \Psi(r_1\sigma_1, r_2\sigma_2, \dots, r_N\sigma_N) \rangle \\
&= \sum_i^N \langle i | \hat{H}_1 | i \rangle + \frac{1}{2} \sum_{ij} \langle ij | \hat{H}_2 | ij \rangle - \langle ij | \hat{H}_2 | ji \rangle \quad (2.7)
\end{aligned}$$

where  $\hat{H}_1$  and  $\hat{H}_2$  stand for one-body and two-body terms of the Hamiltonian:

$$\langle i | \hat{H}_1 | i \rangle = \int dr_1 \phi_i^*(r_1) \left( -\frac{1}{2} \nabla_i^2 + v(r_i) \right) \phi_i(r_1) = h_{ii} \quad (2.8)$$

$$\langle ij | \hat{H}_2 | ij \rangle = \iint dr_1 dr_2 \phi_i^*(r_1) \phi_j^*(r_2) \frac{1}{r_{12}} \phi_i(r_1) \phi_j(r_2) = J_{ij} \quad (2.9)$$

$$\langle ij | \hat{H}_2 | ji \rangle = \iint dr_1 dr_2 \phi_i^*(r_1) \phi_j^*(r_2) \frac{1}{r_{12}} \phi_i(r_2) \phi_j(r_1) = K_{ij} \quad (2.10)$$

The two-body integrals  $J_{ij}$  and  $K_{ij}$  are the classical Coulomb energy and the non-classical exchange energy, respectively. The special thing about using Slater determinant is the natural emergence of exact exchange interaction between electrons of parallel spin. Another advantage of the Slater determinant class is that when  $i = j$ , the Coulomb term  $J_{ii}$  cancels exactly with the exchange term  $K_{ii}$ , corresponding to the physical situation where an electron does not interact with itself, *i.e.* it does not have any *self-interaction*. This marks a central difference between Hartree-Fock and density-functional methods, which inevitably suffer from some form of self-interaction error, to be discussed in later sections.

The second important consequence coming from Hartree-Fock theory is that the variational minimization of the total energy is equivalent to solving the pseudoeigenvalue problems of the effective one-electron operators, the Fock operators  $f$ , for the spin orbitals  $\phi$ 's:

$$f(r_1) \phi_a(r_1) = \varepsilon_a \phi_a(r_1) \quad (2.11)$$

$$f(r_1) = h(r_1) + v^{HF}(r_1) \quad (2.12)$$

where  $h(r_1)$  and  $v^{HF}(r_1)$  correspond to the one-electron core-Hamiltonian operator and an effective one-electron potential operator, the Hartree-Fock potential, respectively.

$$h(r_1) = -\frac{1}{2}\nabla^2 - \sum_I \frac{Z_I}{|r_1 - R_I|} \quad (2.13)$$

$$v^{HF}(r_1) = \sum_b \mathcal{J}_b(r_1) - \mathcal{K}_b(r_1) \quad (2.14)$$

here  $\mathcal{J}_b(r_1)$  and  $\mathcal{K}_b(r_1)$  are the Coulomb and exchange operators which act on the spin orbital via

$$\mathcal{J}_b(r_1)\phi_a(r_1) = \left[ \int dr_2 \phi_b^*(r_2) \frac{1}{r_{12}} \phi_b(r_2) \right] \phi_a(r_1) \quad (2.15)$$

$$\mathcal{K}_b(r_1)\phi_a(r_1) = \left[ \int dr_2 \phi_b^*(r_2) \frac{1}{r_{12}} \phi_a(r_2) \right] \phi_b(r_1) \quad (2.16)$$

$\mathcal{K}_b$  is a *non-local* operator, and in contrast to the *local* operator  $\mathcal{J}_b$ , it involves an exchange of orbitals. For one electron in  $\phi_a$  the expectation values of  $\mathcal{J}_b$  and  $\mathcal{K}_b$  are just the Coulomb and exchange integrals  $J_{ab}$  and  $K_{ab}$ . The problem now becomes a pseudo-eigenvalue equation that involves solving  $f(r_1)\phi_a(r_1) = \varepsilon_a\phi_a(r_1)$  for all spin orbitals  $\phi_i(r_1)$ . As the operators depend on the orbitals, it can only be solved iteratively by a procedure called the self-consistent-field (SCF) method, which calculates the effective potential  $v^{HF}(i)$  from an initial guess set of all the spin orbitals, solves the eigenvalue problem for a new set of spin orbitals, takes them as the new input in a second iteration and repeats the procedure until self-consistency is reached, *i.e.* no more changes from one iteration to the next.

In practice, the Hartree-Fock one-particle eigenvalue equations are transformed into a matrix algebraic problem by introducing a set of known spatial basis functions  $\varphi$ 's<sup>2</sup>. The unknown HF spatial orbitals  $\psi$ 's (the spin coordinate is integrated out for

---

<sup>2</sup>In modern quantum chemical programs, they are usually localized Gaussian or Slater orbitals plus some diffusion and polarization functions

simplicity) to be solved are then linearly expanded as

$$\psi_a = \sum_i C_{ia} \varphi_i \quad (2.17)$$

Eq. 2.11 becomes

$$f(r_1) \sum_i C_{ia} \varphi_i(r_1) = \varepsilon_a \sum_i C_{ia} \varphi_i(r_1) \quad (2.18)$$

Multiplying by  $\varphi_j^*(r_1)$  on both sides of the above equation and integrate over space gives the Roothaan equations

$$\sum_i F_{ji} C_{ia} = \varepsilon_a \sum_i S_{ji} C_{ia} \quad (2.19)$$

$$\text{Fock matrix elements } F_{ji} = \int \varphi_j^*(r_1) f(r_1) \varphi_i(r_1) dr_1 \quad (2.20)$$

$$\text{and overlap-matrix elements } S_{ji} = \int \varphi_j^*(r_1) \varphi_i(r_1) dr_1 \quad (2.21)$$

Roothaan equations can be written more compactly in the matrix form:

$$\mathbf{FC} = \mathbf{SC}\varepsilon \quad (2.22)$$

Solving this generalized eigenvalue problem gives the coefficients for  $\psi(r)$  via the matrix  $\mathbf{C}$  and the orbital eigenvalues  $\varepsilon$ . The  $\{\psi_i(r)\}$ 's that diagonalize the  $\varepsilon$  matrix are called canonical Hartree-Fock spin orbitals. They are generally delocalized and have the symmetry properties of the molecule. Each eigenvalue represents the mean-field electronic energy an electron feels when it occupies that particular spin orbital.

$$\varepsilon_a = f_{aa} = h_{aa} + \sum_{ab}^N J_{ab} - K_{ab} \quad (2.23)$$

The eigenvalue of the occupied ( $\varepsilon_a$ ) and unoccupied ( $\varepsilon_r$ ) spin orbitals in Hartree-Fock theory have a special physical meaning, demonstrated by Koopmans' theorem.



Each one represents the negative of the removal energy or the addition energy of the electron occupying that orbital, under the assumption that the shape of the spin orbital does not further relax upon adding or removing the electron to or from the system.

Finally, the total energy in Hartree-Fock theory can be written as:

$$E_{0,HF} = \sum_a h_{aa} + \frac{1}{2} \sum_{ab}^N J_{ab} - K_{ab} = \sum_a \varepsilon_a - \frac{1}{2} \sum_{ab}^N J_{ab} - K_{ab} \quad (2.24)$$

### 2.1.2 Post Hartree-Fock methods

Although Hartree-Fock theory treats the exchange between same-spin electrons exactly, it lacks “correlation” between electrons (especially between different-spin electrons) and its energy by construction lies higher than the real value. The correlation energy is sometimes defined as the difference between the exact energy  $\mathcal{E}_0$  of the system and the Hartree-Fock energy  $E_{0,HF}$  obtained in the limit of complete basis set:

$$E_{corr} = \mathcal{E}_0 - E_{0,HF} \quad (2.25)$$

Post Hartree-Fock methods, usually known as high-level quantum chemistry methods, take Hartree-Fock theory as a starting point and increase the complexity of the approximation for more accurate descriptions of the system.

#### Many-body perturbation theory

The most straightforward approach to include the effects of electron correlation is through many-body perturbation theory. In particular, Møller and Plesset suggested that the zeroth-order Hamiltonian  $H_0$  could be chosen as the Hartree-Fock Hamiltonian, *i.e.* the total Hamiltonian could be written as

$$H = H_0 + V \quad (2.26)$$

$$H_0 = \sum_i^N f(i) \quad (2.27)$$

the unperturbed zeroth-order state  $|\Psi_0^{(0)}\rangle$  is the exact solution to  $H_0$  and is nothing else but the Hartree-Fock Slater determinant. The zeroth-order energy can be written as

$$H_0|\Psi_0^{(0)}\rangle = E_0^{(0)}|\Psi_0^{(0)}\rangle \quad (2.28)$$

$$E_0^{(0)} = \sum_a^N \varepsilon_a = \sum_a^N f_{aa} = \sum_a^N h_{aa} + \sum_{ab}^N J_{ab} - K_{ab} \quad (2.29)$$

and the perturbation  $V$  is

$$V = H - H_0 = \left( \sum_i^N h(i) + \sum_{i<j}^N r_{ij}^{-1} \right) - \sum_i^N f(i) = \sum_{i<j}^N r_{ij}^{-1} - \sum_i^N v^{HF}(i) \quad (2.30)$$

After some manipulation, the total energy up to the first-order in the perturbation can be written:

$$E = E_0^{(0)} + E_0^{(1)} = \langle \Psi_0 | H_0 | \Psi_0 \rangle + \langle \Psi_0 | V | \Psi_0 \rangle = \sum_a^N \varepsilon_a - \frac{1}{2} \sum_{ij}^N J_{ij} - K_{ij} = E_0^{HF} \quad (2.31)$$

First order Møller-Plesset theory (MP1) is equivalent to the Hartree-Fock approximation. More correlations can be included by going to higher orders of perturbation, e.g. MP2 (with computational costs scaling as  $N^5$ , where  $N$  is the number of electrons), MP3 ( $N^6$ ) or MP4 ( $N^7$ ). MP perturbative approaches work quite successfully for main group compounds, but they can become unstable when the orbitals are nearly degenerate, and as a result it often fails dramatically for transition metal complexes.

## Multi-configurational methods

*Dynamical* correlation comes mainly from the instantaneous electronic repulsion that can not be captured accurately by the mean-field  $v^{HF}$ ; in comparison, the *non-dynamical* correlation refers to the case when one Slater determinant is not a good

representation to the true ground state, as is often the case in dissociation problems, open-shell species and transition-metal complexes. For such systems improvement can be made by allowing more Slater determinants to be included. This is the case in "multiconfigurational" methods as opposed to the single Slater determinant (configuration) of the Hartree-Fock. Conceptually, the simplest way forward is given by configuration-interaction (CI) method, which writes the wavefunction as a superposition of many Slater determinants constructed from excitations of the HF orbitals:

$$|\Psi_{CI}\rangle = c_0|\Phi_0\rangle + \sum_{ar} c_a^r|\Phi_a^r\rangle + \sum_{a<b,r<s} c_{ab}^{rs}|\Phi_{ab}^{rs}\rangle + \sum_{a<b<c,r<s<t} c_{abc}^{rst}|\Phi_{abc}^{rst}\rangle \dots \quad (2.32)$$

Here  $|\Phi_0\rangle$  is the ground state Slater determinant of HF,  $|\Phi_a^r\rangle$  represents the singly excited determinant obtained by promoting one electron from an occupied  $\phi_a$  to an unoccupied  $\phi_r$ , and *etc.*. The coefficients of the ground, singly excited, doubly excited determinant,  $c_0$ ,  $c_a^r$ ,  $c_{ab}^{rs}$  and so on are then optimized variationally, keeping the orbitals fixed. In practice, full-CI (considering up to  $N$ -electron excited determinants) is too computationally demanding and is almost never considered apart from very simple systems such as  $H_2$ . A quick compromise can be met by truncating the expansion up to only singly excited determinant (CIS), or singly and doubly excited determinants (CISD). Unfortunately, truncated CI suffers from size-inconsistency, that is to say, for a supramolecular system, the CISD energy of a dimer does not equal to the sum of CISD energies of the monomer, although an extension that corrects the size-consistency error exists, which is called quadratic configuration interaction (QCI). QCI gives results comparable to this more commonly used and closely-related coupled-cluster (CC) method, which solves this problem via the use of the cluster operator  $\hat{T}$  and writes the wavefunction as:

$$|\Psi_{CC}\rangle = e^{\hat{T}}|\Phi_{HF}\rangle \quad (2.33)$$

$$\hat{T} = \hat{T}_1 + \hat{T}_2 + \hat{T}_3 + \dots \hat{T}_N \quad (2.34)$$

where  $\hat{T}_1$ ,  $\hat{T}_2$ , etc are excitation operators to generate multiply excited determinants which, in the notation of second quantization, can be expressed as:

$$\hat{T}_1 = \sum_{ar} c_a^r \hat{a}_r^\dagger \hat{a}_a \quad (2.35)$$

$$\hat{T}_2 = \frac{1}{4} \sum_{abrs} c_{ab}^{rs} \hat{a}_r^\dagger \hat{a}_s^\dagger \hat{a}_a \hat{a}_b \quad (2.36)$$

and so forth. The cluster operator can be truncated at different levels and is known by acronyms accordingly, *e.g.* CCD for  $\hat{T} = \hat{T}_2$ , CCSD for  $\hat{T} = \hat{T}_1 + \hat{T}_2$  and CCSD(T) for  $\hat{T} = \hat{T}_1 + \hat{T}_2$  and  $\hat{T}_3$  treated perturbatively. The Taylor expansion of the cluster operator  $\hat{T}$  takes into account higher excitations even when  $\hat{T}$  is truncated; for example, in CCD:

$$e^{\hat{T}} = e^{\hat{T}_2} = 1 + \hat{T}_2 + \frac{1}{2!} \hat{T}_2^2 + \dots \quad (2.37)$$

where  $\hat{T}_2^2$  generates quadruple excitations,  $\hat{T}_2^3$  generates hextuple excitations... In comparison, CID is defined only by the first two terms  $1 + \hat{T}_2$ . This allows CC method for the superiority with respect to CI in terms of size-consistency.

CCSD(T) is considered to be the gold standard for most transition-metal complexes, but it is a single-reference method in construction and should be used with caution. One measure of multireference character is called  $T_1$  diagnostic, the root mean square of the single excitation amplitudes  $T_1 = \sqrt{\frac{1}{N} \sum_{ar} (c_a^r)^2}$ . A large  $T_1$  value indicates substantial multi-determinantal character and over-interpretation of coupled-cluster results for such systems might be problematic.

### Multi-reference methods

CI and CC are multi-configurational methods, but they are built from only one single “frozen” reference (a single Hartree-Fock ground state Slater determinant). The jargons of quantum chemistry can look here a bit misleading and bewildering: multi-

configurational self-consistent field (MCSCF) methods refer to using more than one Slater determinant (in contrast to HF) in the self-consistent calculation, thus not only the *weight* but also the *shape* of the orbitals are variationally optimized. MCSCF methods are especially important when the ground state is highly degenerate (*e.g.* the closed-shell singlet cyclobutadiene) or in bond dissociation reactions. One special version of MCSCF is CASSCF, complete active space SCF, in which all Slater determinants that can be formed within a predefined chemical active space (a limited number of occupied and unoccupied orbitals) are considered in the self-consistent procedure. MCSCF is also the starting point for many multi-reference approaches such as MRCI (multi-reference configuration interaction), which differs from CI by using a MCSCF wavefunction rather than using a HF wavefunction. As it can be guessed, multi-reference methods require a lot of experience in their use and some *a priori* knowledge of the answer one is seeking in order to select the best approach.

## 2.2 Density methods

Different from the wavefunction methods which focus on solving for the wavefunction that depends on  $3N$  coordinates, density-functional theory developed an entirely different approach by taking the electron density as a basic variable. This simplifies the problem by enabling one to work directly with a physical observable, the *density*, rather than some abstruse entity, the *wavefunction*. The earliest attempt along this line was given by Thomas and Fermi who came up with a total energy based on a kinetic energy functional derived from the uniform electron gas. Insightful as it was, Thomas-Fermi model was over-simplified and failed to describe accurately real systems. In particular, the atoms as described by TF theory do not bind in molecular systems.

## 2.2.1 Density functional theory

### Hohenberg-Kohn Theorem

The real breakthrough came in 1964 when Hohenberg and Kohn [18] proved in their famous theory that (a) the density  $\rho(r)$  is a basic variable that has a one-to-one correspondence to the external potential  $v(r)$  within an additive constant and (b) that total energy,  $E_v$  can be written as a functional of the density  $E[\rho] = E[\rho(r)]$  and is an upper bound for the real ground state energy. Hohenberg and Kohn showed that the sum of the electron kinetic energy and electron-electron Coulomb repulsion energy can be written as a universal functional independent of the external potential:

$$F[\rho] = \langle \Phi | \hat{T} + \hat{V}_{ee} | \Phi \rangle \quad (2.38)$$

So now for a given external (e.g. nucleus) potential, the total energy functional can be written as:

$$E_v[\rho] = F[\rho] + \int v(r)\rho(r)dr \quad (2.39)$$

The Hohenberg-Kohn variational theorem states that the true ground state electron density  $\rho_0$  minimizes the energy functional to ground state energy  $E_0$ , which is lower than the energy from any arbitrary electron density :

$$E_0 = E_v[\rho_0] < E_v[\rho] \quad (2.40)$$

### Kohn-Sham approach

The HK theorem reduces greatly the complexity of the problem from  $3N$  to 3 variables, if only one knew how to write explicitly the form of  $F[\rho]$ . A significant progress was made when Kohn and Sham [19] introduced a reference system of  $N$  non-interacting electrons and  $N$  one-particle states  $\psi_i$ . The density of this reference system is required to be equal to that of the real one:

$$\rho(r) = \sum_i^N |\psi_i(r)|^2 \quad (2.41)$$

The wavefunction for the reference system  $\Psi_s$  can be written as a Slater determinant and the kinetic energy  $T_s$  of the noninteracting system can be solved exactly as:

$$T_s[\rho] = \sum_i^N \langle \psi_i | -\frac{1}{2} \nabla_i^2 | \psi_i \rangle \quad (2.42)$$

The total energy functional now treats the real kinetic energy  $T[\rho]$  as  $T_s[\rho] + (T[\rho] - T_s[\rho])$ , and the real electron-electron interaction  $V_{ee}[\rho]$  as  $E_H[\rho] + (V_{ee}[\rho] - E_H[\rho])$ , where  $E_H$  is the Hartree energy that represents the classical Coulomb interaction for an electron gas

$$E_H[\rho] = \frac{1}{2} \iint \frac{\rho(r)\rho(r')}{|r-r'|} dr dr' \quad (2.43)$$

The universal functional  $F[\rho]$  now picks up  $T_s[\rho]$  and  $E_H[\rho]$ , and collects the residual terms in the unknown *exchange-correlation energy*  $E_{xc}[\rho]$ :

$$F[\rho] = T_s[\rho] + E_H[\rho] + E_{xc}[\rho] \quad (2.44)$$

$$E_{xc}[\rho] = T[\rho] - T_s[\rho] + V_{ee}[\rho] - E_H[\rho] \quad (2.45)$$

So, in a form reminiscent of Hartree-Fock, the Kohn-Sham approach recasts the N-particle problem into a set of N one-particle equations:

$$\left[ -\frac{1}{2} \nabla_i^2 + v^{KS}(r_i) \right] \psi_i = \varepsilon_i \psi_i \quad (2.46)$$

whose effective one-electron Kohn-Sham potential is defined as

$$v^{KS}(r) = v_{ext}(r) + \frac{\delta E_H[\rho]}{\delta \rho(r)} + \frac{\delta E_{xc}[\rho]}{\delta \rho(r)} = v_{ext}(r) + \int \frac{\rho(r')}{|r-r'|} dr' + v_{xc}(r) \quad (2.47)$$

Similar to Hartree-Fock, these equations are non-linear and need to be solved iteratively. The total energy at self-consistency is then given by

$$E_0 = \sum_i^N \varepsilon_i - E_H[\rho] + E_{xc}[\rho] - \int v_{xc}(r)\rho(r)dr \quad (2.48)$$

### Exchange-correlation functionals

The theory remains exact up to this point but relies on an unknown exchange-correlation functional. The merit of the Kohn-Sham approach is that by mapping the system onto a noninteracting reference, it is able to capture a large part of the energy in terms we know exactly how to calculate,  $T_s[\rho]$  and  $E_H[\rho]$ , shifting the difficulty of the problem into finding the small residual energy functional  $E_{xc}(r)$ , which still has no explicit form. Approximations dedicated to improving the accuracy of the theory follow a Jacob's ladder of increasing complexity. The simplest approximation is local density approximation (LDA), which takes the exchange-correlation energy density at a position  $r$  as that of a homogeneous electron gas with the same density, and writes  $E_{xc}[\rho]$  as

$$E_{xc}^{LDA}[\rho] = \int \rho(r)\varepsilon_{xc}^{hom}(\rho)dr \quad (2.49)$$

where  $\varepsilon_{xc}^{hom}(\rho)$  is the exchange and correlation energy per particle of the uniform electron gas of density  $\rho$ . The corresponding exchange-correlation potential then becomes

$$v_{xc}^{LDA}(r) = \frac{\delta E_{xc}^{LDA}[\rho]}{\delta \rho(r)} = \varepsilon_{xc}^{hom}(\rho) + \rho(r)\frac{\partial \varepsilon_{xc}^{hom}(\rho)}{\partial \rho} \quad (2.50)$$

The second rung is the generalized gradient approximation (GGA), which adds the density gradient  $\nabla\rho(r)$  into the functional as a first order improvement over inhomogeneities [20]. The higher rungs include meta-GGAs, which contain higher order terms such as gradient squared  $(\nabla\rho(r))^2$  and the Laplacians  $\nabla^2\rho(r)$ , and hyper-GGAs, that employ fully non-local exact exchange such as the hybrid functionals. Despite all attempts, however, it is almost impossible to improve  $E_{xc}[\rho]$  systemat-



ically and one usually relies on fitting to high-level Quantum Monte Carlo results or a pre-determined set of experimental values. Thus a certain exchange-correlation functional (denoted by numerous acronyms from its inventor: PBE, PW91, B3LYP, *etc.*) could work moderately well for certain properties of a particular class of materials (*e.g.* metals), but perform poorly for other properties or another class (*e.g.* molecules).

## 2.2.2 Practical implementations of DFT

Similar to the case of Hartree-Fock, the Kohn-Sham equations are usually solved by expanding the orbitals in a basis set and iteratively diagonalizing the Hamiltonian matrix until self-consistency. But unlike wavefunction methods, which were originally developed for isolated molecular species, density-functional theory first appeared as a solid-state electronic-structure theory. Rather than localized atomic orbital basis set, in extended systems with periodic boundary condition, a plane-wave basis set is the most straight-forward and economical choice as had been implemented in many packages. This section intends to outline this framework, as implemented in the Quantum-ESPRESSO [21] distribution, which is the primary DFT tool used in this thesis and is open-source under the GNU public license. General details can be found in Ref. [22] and [23].

### Bloch theorem and plane-wave basis expansion

For a crystal with a periodic potential  $U(\mathbf{r}) = U(\mathbf{r} + \mathbf{R})$ , the Bloch theorem states that the Hamiltonian shares with the translational operator the same eigenstates in the form of

$$\psi_{n\mathbf{k}}(\mathbf{r}) = e^{i\mathbf{k}\mathbf{r}} u_{n\mathbf{k}}(\mathbf{r}) \quad (2.51)$$

where  $u_{n\mathbf{k}}(\mathbf{r})$  satisfies the periodicity of the crystal

$$u_{n\mathbf{k}}(\mathbf{r}) = u_{n\mathbf{k}}(\mathbf{r} + \mathbf{R}) \quad (2.52)$$

Each Bloch wavefunction  $\psi_{n\mathbf{k}}(\mathbf{r})$  is labeled with a wavevector  $\mathbf{k}$  that represents the crystal momentum and a band index  $n$  for different energy levels at a given  $\mathbf{k}$ .

Applying the Hamiltonian on the Bloch wavefunction gives

$$\left[ \frac{1}{2}(\nabla + i\mathbf{k})^2 + U(r) \right] u_{n\mathbf{k}}(\mathbf{r}) = \varepsilon_{n\mathbf{k}} u_{n\mathbf{k}}(\mathbf{r}). \quad (2.53)$$

Thus different  $k$ 's are independent and the Schrödinger equation can be solved separately for each  $\mathbf{k}$ . The charge density self-consistently depends on all  $k$ , and enters into  $U(r)$  so the iterative solution is still coupled at all  $k$ .

The  $u_{n\mathbf{k}}(\mathbf{r})$ , satisfying crystal periodicity, is best described by a plane-wave expansion as

$$u_{n\mathbf{k}}(\mathbf{r}) = \sum_{\mathbf{G}} c_{n\mathbf{k}\mathbf{G}} e^{i\mathbf{G}\mathbf{r}} \quad (2.54)$$

giving

$$\psi_{n\mathbf{k}}(\mathbf{r}) = \sum_{\mathbf{G}} c_{n\mathbf{k}\mathbf{G}} e^{i(\mathbf{k}+\mathbf{G})\mathbf{r}} \quad (2.55)$$

where  $\mathbf{G}$ 's are the reciprocal lattice vectors and satisfy  $e^{i\mathbf{G}\mathbf{R}} = 1$ . Usually  $\mathbf{G}$  runs over all plane-waves within a sphere in reciprocal space with a cut-off energy  $E_{cut}$ , namely for all values of  $\mathbf{G}$  that satisfy

$$\frac{\hbar^2 |\mathbf{k} + \mathbf{G}|^2}{2m_e} \leq E_{cut} \quad (2.56)$$

An appropriate  $E_{cut}$  value needs to be tested for convergence prior to any theoretical investigation. In practice, however, the orthonormality wiggles of the atomic wavefunctions near the nucleus usually imply a very high value of  $E_{cut}$  is required to accurately describe any system, making calculations computationally unfavorable. This eventually led to the idea of pseudopotentials to separate the chemically inert core and reactive valence electrons to greatly reduce the number of plane-waves used, as well as the number of electrons (these will be described later).

## BZ integrations and k-point sampling

For each  $\mathbf{k}' = \mathbf{k} + \mathbf{G}$ , one can derive  $u_{n\mathbf{k}'}(\mathbf{r}) = e^{i\mathbf{G}\mathbf{r}}u_{n\mathbf{k}}(\mathbf{r})$  from Eq. 2.54, or equivalently

$$\psi_{n\mathbf{k}}(\mathbf{r}) = \psi_{n,\mathbf{k}+\mathbf{G}}(\mathbf{r}) \quad (2.57)$$

as well as

$$\varepsilon_{n\mathbf{k}} = \varepsilon_{n,\mathbf{k}+\mathbf{G}} \quad (2.58)$$

Therefore Bloch theorem allows one to represent the macroscopic crystal within a small unit cell consisting just a few inequivalent atoms. Ideally physical quantities should be integrated over all possible  $\mathbf{k}$ 's within the first Brillouin Zone (BZ) to represent an infinite crystal, but in reality periodic-boundary conditions on the electronic wavefunctions (called Born-von Karman (BvK)) are often applied to reduce the number of  $\mathbf{k}$  points. BvK boundary conditions are

$$\psi_{n\mathbf{k}}(\mathbf{r}) = \psi_{n\mathbf{k}}(\mathbf{r} + \sum_{i=1}^3 N_i \hat{a}_i) \quad (2.59)$$

where  $N_1, N_2, N_3$  are integers and  $\hat{a}_i$ 's are unit lattice vectors. Therefore one has

$$e^{i\mathbf{k}\mathbf{r}}u_{n\mathbf{k}}(\mathbf{r}) = e^{i\mathbf{k}\mathbf{r}}e^{i\mathbf{k}\sum N_i \hat{a}_i}u_{n\mathbf{k}}(\mathbf{r}) = e^{i(\mathbf{k}+\sum N_i \hat{a}_i)\mathbf{r}}u_{n\mathbf{k}}(\mathbf{r} + N_i \hat{a}_i) \quad (2.60)$$

so that

$$\mathbf{k}_i N_i \hat{a}_i = 2n_i \pi \quad (2.61)$$

or

$$\mathbf{k}_i = \frac{n_i}{N_i} \frac{2\pi}{\hat{a}_i} = \frac{n_i}{N_i} \hat{b}_i \quad (2.62)$$

where  $n_i = 1, 2, 3 \dots N_i$  and  $\hat{b}_i$ 's are the unit reciprocal lattice vectors. In other words, the Born-von Karman boundary conditions state that a supercell containing  $N_1 \times N_2 \times N_3$  unit cells can be accurately described by the wavefunction of a unit cell modulated by  $e^{i\mathbf{k}\mathbf{r}}$  where  $\mathbf{k}$  is constrained by the above equation. Thus the entire BZ integration is reduced to summation of discrete  $k$ -points. The simplest method

samples all the allowed  $k$ -points in Eq. 2.62 in equal spacing within the first BZ, also called Monkhorst-Pack sampling [24].

## Pseudopotentials

The concept of pseudopotentials refers to approximating the real asymptotic Coulomb potential of atoms by an effective potential  $V^{PS}$  that includes the screening of the core electrons. Pseudopotentials are devised in a way such that the corresponding pseudo valence wavefunctions have the ideal properties of (1) perfectly matching the real valence wavefunctions outside some cut-off radius  $R_c$  and (2) the eigenvalues reproduce the true eigenvalues for each pseudo-wavefunction  $\varepsilon_v^{PS} = \varepsilon_v^{AE}$ . Since each wavefunction “feels” the screening differently according to their different angular nature, the pseudo-potential naturally has to be composed of a local radial part and a non-local, angular-dependent part:

$$V^{PS}(r) = \begin{cases} V^{loc}(r) = V^{AE}(r) & \text{if } r \geq R_c \\ V^{loc}(r) + \sum_{l,m} |Y_{lm}\rangle V_l^{nloc}(r) \langle Y_{lm}| & \text{if } r \leq R_c \end{cases} \quad (2.63)$$

where  $Y_{lm}$  are spherical harmonics. In *norm-conserving* pseudopotentials, the pseudo-wavefunctions are constrained under the orthonormality requirement  $\langle \psi_i^{NC} | \psi_j^{NC} \rangle = \delta_{ij}$ . Nevertheless, although many valence electron orbitals have most of the density outside the cut-off radius and can be approximated as node-less smoothly varying pseudo-wavefunctions by norm-conserving pseudopotentials, the  $2p$ ,  $3d$ , and  $4f$  orbitals, being the first angular momentum to appear of its kind, retain most of the density close to the core region. Thus a norm-conserving pseudopotential does little to reduce the plane-wave cut-off for these orbitals. The solution for this is the *ultrasoft* pseudopotential, which relaxes the norm-conserving constraint and rewrites the Schrödinger equation as a generalized eigenvalue problem:

$$\hat{H}|\psi_n^{US}\rangle = \varepsilon_n \hat{S}|\psi_n^{US}\rangle \quad (2.64)$$

with an orthonormality condition redefined as

$$\langle \psi_n^{US} | \hat{S} | \psi_n^{US} \rangle = \delta_{ij} \quad (2.65)$$

where  $\hat{S}$  is an overlap operator that contains the "augmentation charge" that ensures correct charge density in the core region.

$$\hat{S} = 1 + \sum_{i,j,I} Q_{ij}^I |\beta_i^I\rangle \langle \beta_j^I| \quad (2.66)$$

$\beta_i^I$ 's are projector functions that run over different angular momentum channels and depend on the ionic positions, while  $Q_{ij}^I$  is an augmentation function given by:

$$Q_{ij} = \int_0^{R_c} (\psi_i^{AE*}(r) \psi_j^{AE}(r) - \psi_i^{US*}(r) \psi_j^{US}(r)) dr \quad (2.67)$$

## 2.3 Maximally localized wannier functions

Wannier functions (WFs), originally introduced by Wannier in 1937 [25], are orthonormal atomic-like wavefunctions that span the same space represented by Bloch states. For an isolated set of  $N$  Bloch bands  $\psi_n \mathbf{k}(r)$ , a set of WFs  $w_{n\mathbf{R}}(r) = w_n(r - \mathbf{R})$ ,  $n \in [1, N]$ , labeled by Bravais lattice vectors  $\mathbf{R}$ , can be constructed by the Fourier transformation of Bloch states over the Brillouin zone (BZ):

$$|w_{n\mathbf{R}}(r)\rangle = \frac{V}{(2\pi)^3} \int_{BZ} \left[ \sum_{m=1}^N \mathbf{U}_{mn}^{\mathbf{k}} |\psi_{n\mathbf{k}}\rangle \right] e^{-i\mathbf{k}\mathbf{R}} d\mathbf{k} \quad (2.68)$$

where  $\mathbf{U}^{(\mathbf{k})}$  is a unitary matrix that mixes the bands at wave-vector  $\mathbf{k}$ , and  $V$  is the volume of the real-space primitive cell.

Due to the phase indeterminacy  $e^{i\phi_n(\mathbf{k})}$  of an isolated Bloch state  $\psi_n \mathbf{k}(r)$  at each wave vector  $\mathbf{k}$ , the choice of  $\mathbf{U}^{(\mathbf{k})}$  is not unique. One strategy to determine  $\mathbf{U}^{(\mathbf{k})}$  is to choose one that minimizes the spatial spread of the WFs:

$$\Omega = \sum_n [\langle w_{n\mathbf{0}}(r) | r^2 | w_{n\mathbf{0}}(r) \rangle - \langle w_{n\mathbf{0}}(r) | \mathbf{r} | w_{n\mathbf{0}}(r) \rangle^2] \quad (2.69)$$

Wannier functions obtained this way are named *maximally localized wannier functions* (MLWFs) [26]. This formulation offers an extension of the *localized molecular orbitals* for molecular systems [27] to the solid-state case. In many instances, MLWFs are the most natural choice for a set of localized orbitals that span the same Hilbert space of the Hamiltonian eigenfunctions, and they provide a clear picture of chemical bonding.

### 2.3.1 Localization procedure

In a reciprocal space, the expectation values in Eq. 2.69 can be expressed as [26]:

$$\langle w_{n\mathbf{0}}(r) | \mathbf{r} | w_{n\mathbf{0}}(r) \rangle = \langle \mathbf{r} \rangle_n = i \frac{V}{(2\pi)^3} \int e^{i\mathbf{k}\cdot\mathbf{R}} \langle u_{n\mathbf{k}} | \nabla_{\mathbf{k}} | u_{n\mathbf{k}} \rangle d\mathbf{k} \quad (2.70)$$

$$\langle w_{n\mathbf{0}}(r) | r^2 | w_{n\mathbf{0}}(r) \rangle = \langle r^2 \rangle_n = i \frac{V}{(2\pi)^3} \int e^{i\mathbf{k}\cdot\mathbf{R}} \langle u_{n\mathbf{k}} | \nabla_{\mathbf{k}}^2 | u_{n\mathbf{k}} \rangle d\mathbf{k} \quad (2.71)$$

where  $u_{n\mathbf{k}} = e^{-i\mathbf{k}\cdot\mathbf{r}} \psi_{n\mathbf{k}}$  is the periodic part of the Bloch function  $\psi_{n\mathbf{k}}$ .

In a uniformly-discretized BZ, the overlap matrix between Bloch orbitals can be defined as

$$M_{mn}^{(\mathbf{k},\mathbf{b})} = \langle u_{m\mathbf{k}} | u_{n,\mathbf{k}+\mathbf{b}} \rangle = \langle \psi_{m\mathbf{k}} | e^{-i\mathbf{b}\cdot\mathbf{r}} | \psi_{n,\mathbf{k}+\mathbf{b}} \rangle \quad (2.72)$$

where  $\mathbf{b}$  is a set of vectors that connect a mesh point  $\mathbf{k}$  to its near neighbors. After some algebra, the gradient and the Laplacian can be rewritten in terms of the overlap matrix [28], giving for

$$\langle \mathbf{r} \rangle_n = -\frac{1}{N_{kp}} \sum_{\mathbf{k}} \sum_{\mathbf{b}}^{N_b} W_b \mathbf{b} \operatorname{Im} \ln M_{mn}^{(\mathbf{k}, \mathbf{b})} \quad (2.73)$$

$$\langle r^2 \rangle_n = \frac{1}{N_{kp}} \sum_{\mathbf{k}} \sum_{\mathbf{b}}^{N_b} W_b \{ [1 - |M_{nn}^{(\mathbf{k}, \mathbf{b})}|^2] + [|\operatorname{Im} \ln M_{nn}^{(\mathbf{k}, \mathbf{b})}|^2] \} \quad (2.74)$$

where  $N_{kp}$  is the number of  $\mathbf{k}$ -points,  $N_b$  is the number of  $b$  vectors, and  $W_b$  is the weighting factor for the corresponding vector  $\mathbf{b}$ . The spread functional  $\Omega$  can now be expressed in terms of  $M_{mn}^{(\mathbf{k}, \mathbf{b})}$ , and the minimization of  $\Omega$  with respect to  $U^{\mathbf{k}}$  is then performed using steepest descent or conjugate gradients, until the stationary condition  $\frac{d\Omega}{dU^{\mathbf{k}}} = 0$  is reached.

### 2.3.2 Disentanglement

For an isolated set of bands such as the valence states in an insulator, the above procedure is straightforward. When a system is metallic, however, a *disentanglement* procedure [29] is needed to separate a group of bands since all bands near the Fermi level are mixed together and there is no visible gap in between. This is done by performing another unitary transformation  $U^{\text{dis}(\mathbf{k})}$  prior to localization. At each  $\mathbf{k}$ -point, an energy window that contains  $N_{\text{win}}^{\mathbf{k}}$  states is defined and a subspace  $S(\mathbf{k})$  spanned by  $N$  ( $N < N_{\text{win}}^{\mathbf{k}}$ ) Bloch states is determined:

$$|u_{\mathbf{n}\mathbf{k}}^{\text{opt}}\rangle = \sum_{m \in N_{\text{win}}^{\mathbf{k}}} U_{mn}^{\text{dis}(\mathbf{k})} |u_{m\mathbf{k}}\rangle \quad (2.75)$$

where  $U^{\text{dis}(\mathbf{k})}$  is a rectangular  $N_{\text{win}}^{\mathbf{k}} \times N$  matrix. The disentanglement procedure is equivalent to selecting a subspace out of the entangled space that is *maximally-connected* across each  $\mathbf{k}$ -point, *i.e.* with maximum overlap between  $S(\mathbf{k})$  and  $S(\mathbf{k} + \mathbf{b})$ .

### 2.3.3 Real-space Hamiltonians

In the Bloch representation, the Hamiltonian by definition is diagonal  $H_{mn}(\mathbf{k}) = \epsilon_{n\mathbf{k}}\delta_{mn}$ . After finding the unitary matrix  $U(\mathbf{k})$  that minimizes the spread, we obtain the Hamiltonian in a transformed representation

$$H^{(rot)}(\mathbf{k}) = U(\mathbf{k})^\dagger H(\mathbf{k})U(\mathbf{k}) \quad (2.76)$$

that can then be Fourier transformed to give the Hamiltonian in the MLWF basis

$$H_{mn}^{(rot)}(\mathbf{R}) = \frac{1}{N_{kp}} \sum_{\mathbf{k}} e^{-i\mathbf{k}\cdot\mathbf{R}} H_{mn}^{(rot)}(\mathbf{k}) = \langle w_{m\mathbf{0}} | \hat{H} | w_{n\mathbf{R}} \rangle \quad (2.77)$$

Due to the strong localization of MLWFs, the matrix elements  $H_{mn}(\mathbf{R})$  decay rapidly with  $\mathbf{R}$ , making the Hamiltonian a sparse matrix. In the following chapter, we would see how MLWFs offer a bridge between plane-wave electronic structure and Green's function formalism for transport calculations.



# Chapter 3

## Quantum Transport Theory

### Introduction

Classical theories of transport treat electrons as particles. Electrons move unimpeded and are freely accelerated by the external field for a characteristic relaxation time until they are scattered by a defect, a phonon, or another electron. The direct result of this classical particle assumption gives the well-known Ohm's law, which states that the conductance ( $G$ ) of a rectangular two-dimensional conductor is directly proportional to its width ( $W$ ) and inversely proportional to its length ( $L$ ):

$$G = \frac{\sigma W}{L} \quad (3.1)$$

where  $\sigma$  is the conductivity of the material. As the size of devices begins to shrink, however, the wave nature of electrons becomes non-negligible and consequently, classical transport theory can no longer hold. The quantum characteristics of the transport phenomena must be taken into account as the device dimensions  $L$  reach the scale of the following characteristic lengths: (1) the de Broglie wavelength  $\lambda_F$  determined by the kinetic energy of the electrons, (2) the momentum-relaxation length  $L_m$  which is the distance that an electron travels before its initial momentum is destroyed, and (3) the phase-relaxation length  $L_\psi$  which is the distance that an electron travels before it

loses the initial phase information. In this chapter, we focus on the phase-coherent transport regime where  $L_\psi$  is a lot larger than the device length, i.e.  $L \ll L_\phi$ , as is the case in single molecule transport, and we introduce some formal approaches to quantum conductance, namely Landauer’s approach in a Green’s function technique.

## 3.1 Landauer Formalism for Phase Coherent Transport

### 3.1.1 Quantum Scattering Theory

The theory for electron transport through nanoscale devices is in essence scattering theory [30]. Consider the 1-D case where a plane wave is scattered by a step potential barrier:

$$U(z) = \begin{cases} 0 & z < 0 \\ U_0 & z > 0 \end{cases} \quad (3.2)$$

The solution for the scattered state wavefunction is given by

$$\psi(z) = \begin{cases} A_+^i e^{ikz} + A_-^o e^{-ikz} & z < 0 \\ B_+^o e^{ik'z} + B_-^i e^{-ik'z} & z > 0 \end{cases} \quad (3.3)$$

The “+” and “−” subscripts are for right-moving and left moving wavefunctions, and the “i” and “o” superscripts mark the incoming and outgoing waves toward the barrier boundary, respectively. The coefficients are related to each other from the boundary conditions expressed in the matrix  $\mathbf{M}$ :

$$\begin{pmatrix} A_+^i \\ A_-^o \end{pmatrix} = \mathbf{M} \begin{pmatrix} B_+^o \\ B_-^i \end{pmatrix} = \begin{pmatrix} \frac{1+\alpha}{2} & \frac{1-\alpha}{2} \\ \frac{1-\alpha}{2} & \frac{1+\alpha}{2} \end{pmatrix} \begin{pmatrix} B_+^o \\ B_-^i \end{pmatrix} \quad (3.4)$$

where  $\alpha = \sqrt{\frac{E - U_0}{E}} = \frac{v_R}{v_L}$ . Alternatively, the incoming and outgoing waves can also be related by the *scattering matrix*  $\mathbf{S}$ :

$$\begin{pmatrix} A_-^o \\ B_+^o \end{pmatrix} = \mathbf{S} \begin{pmatrix} A_+^i \\ B_-^i \end{pmatrix} = \begin{pmatrix} \frac{1-\alpha}{1+\alpha} & \frac{2\alpha}{1+\alpha} \\ \frac{2\alpha}{1+\alpha} & \frac{-1+\alpha}{1+\alpha} \end{pmatrix} \begin{pmatrix} A_+^i \\ B_-^i \end{pmatrix} \quad (3.5)$$

To find the transmission and reflection coefficients we set  $B_-^i = 0$  (*i.e.* the wave is only coming in from the left), then the transmission probability  $T(E)$  and the reflection probability  $R(E)$  become

$$T(E) = \frac{v_R |B_+^o|^2}{v_L |A_+^i|^2} = \frac{4\alpha}{(1+\alpha)^2} \quad (3.6)$$

$$R(E) = \frac{|A_-^o|^2}{|A_+^i|^2} = \frac{(1-\alpha)^2}{(1+\alpha)^2} \quad (3.7)$$

$$T(E) + R(E) = 1 \quad (3.8)$$

The elements in the matrices  $\mathbf{M}$  and  $\mathbf{S}$  are expressed in terms of the amplitudes of the *waves*. One can define another matrix  $\mathbf{S}'$  in terms of the amplitudes of the *currents* to satisfy the current conservation rule and the unitary condition,  $\mathbf{S}'^\dagger \mathbf{S}' = \mathbf{I}$ :

$$S'_{nm} = \sqrt{\frac{v_n}{v_m}} S_{nm} \quad (3.9)$$

The elements inside the unitary scattering matrix  $\mathbf{S}'$  are related to the *transmission* and *reflection* coefficients in the following way:

$$\mathbf{S}' = \begin{pmatrix} \frac{1-\alpha}{1+\alpha} & \frac{2\sqrt{\alpha}}{1+\alpha} \\ \frac{2\sqrt{\alpha}}{1+\alpha} & \frac{-1+\alpha}{1+\alpha} \end{pmatrix} = \begin{pmatrix} r & t' \\ t & r' \end{pmatrix} \quad (3.10)$$

where  $r$  and  $t$  describe transmission and reflection of left-incident waves, and  $r'$

and  $t'$  for right-incident waves. As shown in this case, in general  $t = t'$  holds, i.e. the left-incident and the right-incident waves have the same transmission probability given by time-reversal symmetry. The transmission probability  $T(E)$  comes naturally from the square modulus of  $t$

$$T(E) = \frac{4\alpha}{(1 + \alpha)^2} = t^\dagger t = |t|^2 \quad (3.11)$$

The example shown here is the so-called *single-channel* transmission where only one possible  $|k|$  exists for any given energy. In the three-dimensional case, if the  $(x, y)$  dimensions are constrained and only certain transverse modes exist for a given energy, multiple  $k_z$ 's can exist and scatter into each other.

$$E = \frac{\hbar^2 k_z^2}{2m} + E_{x,y}^n \quad n = 1, 2, 3 \dots N_{L,R} \quad (3.12)$$

For the *multi-channel* case, the scattering matrix  $\mathbf{S}'$  is a square matrix with dimension  $N = N_L + N_R$ , where  $N_L$  and  $N_R$  are the number of channels for the left and right side of the system.  $\mathbf{S}'$  can be written in the form

$$\mathbf{S}' = \begin{pmatrix} \mathbf{r} & \mathbf{t}' \\ \mathbf{t} & \mathbf{r}' \end{pmatrix} \quad (3.13)$$

where  $\mathbf{r}$ ,  $\mathbf{t}$ ,  $\mathbf{r}'$ , and  $\mathbf{t}'$  now also become matrices and have the dimensions of  $N_L \times N_L$ ,  $N_R \times N_L$ ,  $N_R \times N_R$  and  $N_L \times N_R$ , respectively.  $T_{\beta\alpha} = |t_{\beta\alpha}|^2$  are the probabilities of transmission from the left mode  $\alpha$  into the right mode  $\beta$ . The total transmission from left to right is

$$T(E) = \sum_{\beta \in R} \sum_{\alpha \in L} T_{\beta\alpha} = \text{Tr}(\mathbf{t}^\dagger \mathbf{t}) = \sum_n T_n \quad (3.14)$$

where  $T_n$ 's are the *eigenvalues* of the  $\mathbf{t}^\dagger\mathbf{t}$  matrix and represent the transmission probabilities of the non-mixing *eigenchannels*.

### 3.1.2 Current from transmission

Landauer approach [31] describes the current through a conductor as the probability that an electron can transmit through it. For a single-channel conductor connected to reservoirs both on the left and the right sides, the current is

$$J(V) = \frac{2e}{L} \sum_k v f(k) T(k) = \frac{2e}{L} \frac{L}{2\pi} \int dk \left(\frac{\hbar k}{m}\right) f(k) T(k) \quad (3.15)$$

since

$$E = \frac{\hbar^2 k^2}{2m} \quad dE = \left(\frac{\hbar k}{m}\right) \hbar dk \quad (3.16)$$

The net current that passes through the conductor under finite bias  $V$  would be

$$J(V) = J_{L \rightarrow R} - J_{R \rightarrow L} = \frac{2e}{h} \int_{-\infty}^{\infty} T(E, V) [f_L(E + eV) - f_R(E)] dE = \frac{2e^2}{h} T(E, V) V \quad (3.17)$$

and the conductance

$$G = \frac{dJ}{dV} = \frac{2e^2}{h} T(E, V) = T(E, V) G_0 \quad (3.18)$$

where  $G_0$  is the conductance quantum,  $G_0 = \frac{2e^2}{h} = 77.5 \mu S$ . For multi-channel conductors, the total transmission is the sum of the contribution from all channels, and the generalized two-terminal Landauer transport is given by the Fisher-Lee formula [32]:

$$G = \frac{2e^2}{h} \sum_{\beta \in R} \sum_{\alpha \in L} T_{\beta\alpha}(E, V) = \frac{2e^2}{h} \text{Tr}(\mathbf{t}^\dagger \mathbf{t}) \quad (3.19)$$

## 3.2 Green's Function Method in a Localized Basis Set

In principle, the transmission function  $T(E)$  for a coherent conductor must be calculated from the scattering matrix, which can be obtained from the solution of the Schrödinger equation. Nevertheless, in the atomistically defined LCR systems, solving for the scattering states requires the non-trivial task of calculating the complex band structure in the electrodes. This difficulty can be circumvented by the powerful method of Green's functions, which express the elements of the scattering matrix in terms of the Green's function of the conductor part [33, 34, 35] and is simpler to compute.

For a system represented by an Hamiltonian  $H$ , the retarded and advanced Green's functions are defined as follows:

$$[(E + i\eta)I - H]G^r = I \quad (3.20a)$$

$$G^r = [(E + i\eta)I - H]^{-1} \quad (3.20b)$$

and

$$[(E - i\eta)I - H]G^a = I \quad (3.21a)$$

$$G^a = [(E - i\eta)I - H]^{-1} \quad (3.21b)$$

$$G^a = (G^r)^\dagger. \quad (3.22)$$

where  $\eta$  is an infinitesimally small positive number ( $\eta \rightarrow 0^+$ ) that ensures the correct boundary conditions.

### 3.2.1 Green's function method for extended systems

Consider a “left lead-conductor-right lead” (LCR) structure described by some localized basis such as atomic orbitals or Wannier functions. The wavefunctions are represented by a linear combinations of the localized basis set,  $\psi = \sum_{\alpha} c_{\alpha} |\alpha\rangle$ . The matrix elements of the Hamiltonian  $H_{\alpha\beta} = \langle \alpha | H | \beta \rangle$  gradually decay to zero as the distance between the basis functions  $|\alpha\rangle$  and  $|\beta\rangle$  increases. If the conductor region is long enough such that there is no interaction between the left and the right leads, the full Hamiltonian of the system has the following block form:

$$\mathbf{H} = \begin{pmatrix} \mathbf{H}_L & \mathbf{H}_{LC} & 0 \\ \mathbf{H}_{LC}^{\dagger} & \mathbf{H}_C & \mathbf{H}_{CR} \\ 0 & \mathbf{H}_{CR}^{\dagger} & \mathbf{H}_R \end{pmatrix} \quad (3.23)$$

where  $\mathbf{H}_L$ ,  $\mathbf{H}_C$ ,  $\mathbf{H}_R$  are Hamiltonians of the left lead, the system, and the right lead, respectively. The off-diagonal terms  $\mathbf{H}_{LC}$  and  $\mathbf{H}_{CR}$  describe the coupling between the leads and the conductor. The matrix form of the Green's function (from now on we only look at the retarded Green's function  $G^r$ ) for this system can be further partitioned into submatrices corresponding to the conductor and the leads:

$$\begin{pmatrix} \mathbf{E} - \mathbf{H}_L & -\mathbf{H}_{LC} & 0 \\ -\mathbf{H}_{LC}^{\dagger} & \mathbf{E} - \mathbf{H}_C & -\mathbf{H}_{CR} \\ 0 & -\mathbf{H}_{CR}^{\dagger} & \mathbf{E} - \mathbf{H}_R \end{pmatrix} \begin{pmatrix} \mathbf{G}_L & \mathbf{G}_{LC} & \mathbf{G}_{LR} \\ \mathbf{G}_{CL} & \mathbf{G}_C & \mathbf{G}_{CR} \\ \mathbf{G}_{RL} & \mathbf{G}_{RC} & \mathbf{G}_R \end{pmatrix} = \mathbf{I} \quad (3.24)$$

where we have substituted  $\mathbf{E}$  for  $(E + i\eta)\mathbf{I}$ . Take each row of the first matrix and multiply by the second column of the second matrix and we have:

$$(\mathbf{E} - \mathbf{H}_L)\mathbf{G}_{LC} - \mathbf{H}_{LS}\mathbf{G}_C = 0 \quad (3.25)$$

$$-\mathbf{H}_{LC}^\dagger\mathbf{G}_{LC} + (\mathbf{E} - \mathbf{H}_C)\mathbf{G}_C - \mathbf{H}_{CR}^\dagger\mathbf{G}_{RC} = \mathbf{I} \quad (3.26)$$

$$-\mathbf{H}_{CR}^\dagger\mathbf{G}_C + (\mathbf{E} - \mathbf{H}_R)\mathbf{G}_{CR} = 0 \quad (3.27)$$

$$(3.28)$$

After some manipulations one can get a simplified expression for  $\mathbf{G}_C$ :

$$\mathbf{G}_C = [\mathbf{E} - \mathbf{H}_C - \boldsymbol{\Sigma}_L - \boldsymbol{\Sigma}_R]^{-1} \quad (3.29)$$

where  $\boldsymbol{\Sigma}_L = \mathbf{H}_{LC}^\dagger\mathbf{G}_L\mathbf{H}_{LC}$  and  $\boldsymbol{\Sigma}_R = \mathbf{H}_{CR}^\dagger\mathbf{G}_R\mathbf{H}_{CR}$  are the *self-energy* terms for the left and the right lead, respectively [11].  $\mathbf{H}_C + \boldsymbol{\Sigma}_L + \boldsymbol{\Sigma}_R$  can be viewed as the effective Hamiltonian for the conductor interacting with semi-infinite leads. The *spectral function*  $\mathbf{A}_C$  is defined as the imaginary part of the Green's function, which gives the local density of states for the conductor [11].

$$\mathbf{A}_C = i(\mathbf{G}_C - \mathbf{G}_C^\dagger) \quad (3.30)$$

$$N_C(E) = \frac{1}{2\pi}\text{Tr}[\mathbf{A}_C(E)] = -\frac{1}{\pi}\text{Im}\{\text{Tr}[\mathbf{G}_C(E)]\} \quad (3.31)$$

The complex self-energy terms contain a few important physical aspects. The real part describes the energy shift of the level of the conductor region when it is connected to the leads, and the imaginary part describes the level broadening, which is a measure of the coupling strength. The *coupling functions* are therefore defined as

$$\Gamma_{L,R} = i(\boldsymbol{\Sigma}_{L,R}^r - \boldsymbol{\Sigma}_{L,R}^a) \quad (3.32)$$



where the advanced self-energy  $\Sigma_{L,R}^a$  is the Hermitian conjugate of  $\Sigma_{L,R}^r$ .

### 3.2.2 The principal-layer approach for semi-infinite leads

As our system involves semi-infinite left and right leads, the submatrices of the Hamiltonian have infinite dimensions, except for  $\mathbf{H}_C$ . Therefore, the evaluation of the self-energy terms require manipulation of matrices with infinite dimensions. It is convenient to adopt the *principal layer* approach [36, 37] in which one can define the minimal length it takes between two basis functions  $|\alpha\rangle$  and  $|\beta\rangle$  in the lead to have negligible interactions (*i.e.*  $\langle\alpha|H|\beta\rangle \sim 0$ ) as the length of a *principal layer*. The principal layer of the lead should contain enough unit cells such that the interactions between the  $i$ -th and  $i + 2$ -th layer is negligible, and the Hamiltonian can be recast as

$$\mathbf{H} = \begin{pmatrix} \mathbf{H}_L & \mathbf{H}_{LC} & 0 \\ \mathbf{H}_{LC}^\dagger & \mathbf{H}_C & \mathbf{H}_{CR} \\ 0 & \mathbf{H}_{CR}^\dagger & \mathbf{H}_R \end{pmatrix} = \begin{pmatrix} \ddots & \vdots & \vdots & \vdots & \vdots & \vdots & \ddots \\ \dots & \mathbf{H}_L^{00} & \mathbf{H}_L^{10} & 0 & 0 & 0 & \dots \\ \dots & \mathbf{H}_L^{10\dagger} & \mathbf{H}_L^{00} & \mathbf{h}_{LC} & 0 & 0 & \dots \\ \dots & 0 & \mathbf{h}_{LC}^\dagger & \mathbf{H}_C & \mathbf{h}_{CR} & 0 & \dots \\ \dots & 0 & 0 & \mathbf{h}_{CR}^\dagger & \mathbf{H}_R^{00} & \mathbf{H}_R^{01} & \dots \\ \dots & 0 & 0 & 0 & \mathbf{H}_R^{01\dagger} & \mathbf{H}_R^{00} & \dots \\ \ddots & \vdots & \vdots & \vdots & \vdots & \vdots & \ddots \end{pmatrix} \quad (3.33)$$

As shown in Eq. 3.33, all information of the infinitely-dimensional  $\mathbf{H}_{LC}$  is now contained within a small submatrix  $\mathbf{h}_{LC}$  with dimension  $N_C \times N_L$ , where  $N_L$  and  $N_C$  are the number of basis functions in the principal layer of the lead and in the conductor region, respectively.

The self-energy term for the left lead now becomes

$$\Sigma_L = \mathbf{H}_{LC}^\dagger \mathbf{G}_L \mathbf{H}_{LC} = \left( \dots \quad \dots \quad \dots \quad \mathbf{h}_{LC}^\dagger \right) \times \mathbf{G}_L \times \begin{pmatrix} \vdots \\ \vdots \\ \vdots \\ \vdots \\ \mathbf{h}_{LC} \end{pmatrix} \quad (3.34)$$

$$\mathbf{G}_L = \begin{pmatrix} \ddots & \vdots & \vdots & \vdots \\ \dots & \mathbf{E} - \mathbf{H}_L^{00} & \mathbf{H}_L^{10} & 0 \\ \dots & \mathbf{H}_L^{10\dagger} & \mathbf{E} - \mathbf{H}_L^{00} & \mathbf{H}_L^{10} \\ \dots & 0 & \mathbf{H}_L^{10\dagger} & \mathbf{E} - \mathbf{H}_L^{00} \end{pmatrix}^{-1} = \begin{pmatrix} \ddots & \vdots & \vdots & \vdots \\ \dots & \mathbf{g}_L^{22} & \mathbf{g}_L^{21} & \mathbf{g}_L^{20} \\ \dots & \mathbf{g}_L^{10\dagger} & \mathbf{g}_L^{11} & \mathbf{g}_L^{10} \\ \dots & \mathbf{g}_L^{20\dagger} & \mathbf{g}_L^{10\dagger} & \mathbf{g}_L^{00} \end{pmatrix} \quad (3.35)$$

Inserting Eq. 3.35 into Eq. 3.34 we get  $\Sigma_L = \mathbf{H}_{LC}^\dagger \mathbf{G}_L \mathbf{H}_{LC} = \mathbf{h}_{LC}^\dagger \mathbf{g}_L^{00} \mathbf{h}_{LC}$ , where  $\mathbf{g}_L^{00}$  is called the *surface Green's function*.

### 3.2.3 The surface Green's function

With the help of the principal-layer approach, one can transform the infinite-dimensional problem into a finite-dimensional matrix multiplication, and we are now left with the task of evaluating the surface Green's function  $\mathbf{g}_L^{00}$  [38, 39].

From the definition of  $\mathbf{G}_L$

$$\begin{pmatrix} \ddots & \vdots & \vdots & \vdots \\ \dots & \mathbf{E} - \mathbf{H}_L^{00} & \mathbf{H}_L^{10} & 0 \\ \dots & \mathbf{H}_L^{10\dagger} & \mathbf{E} - \mathbf{H}_L^{00} & \mathbf{H}_L^{10} \\ \dots & 0 & \mathbf{H}_L^{10\dagger} & \mathbf{E} - \mathbf{H}_L^{00} \end{pmatrix} \begin{pmatrix} \ddots & \vdots & \vdots & \vdots \\ \dots & \mathbf{g}_L^{22} & \mathbf{g}_L^{21} & \mathbf{g}_L^{20} \\ \dots & \mathbf{g}_L^{10\dagger} & \mathbf{g}_L^{11} & \mathbf{g}_L^{10} \\ \dots & \mathbf{g}_L^{20\dagger} & \mathbf{g}_L^{10\dagger} & \mathbf{g}_L^{00} \end{pmatrix} = \mathbf{I} \quad (3.36)$$

Multiplication between each row of the first matrix and the last column of the second matrix gives

$$(\mathbf{E} - \mathbf{H}_L^{00})\mathbf{g}_L^{00} = \mathbf{I} + \mathbf{H}_L^{10\dagger}\mathbf{g}_L^{10} \quad (3.37)$$

$$(\mathbf{E} - \mathbf{H}_L^{00})\mathbf{g}_L^{10} = \mathbf{H}_L^{10\dagger}\mathbf{g}_L^{20} + \mathbf{H}_L^{10}\mathbf{g}_L^{10} \quad (3.38)$$

.....

$$(\mathbf{E} - \mathbf{H}_L^{00})\mathbf{g}_L^{n0} = \mathbf{H}_L^{10\dagger}\mathbf{g}_L^{n+1,0} + \mathbf{H}_L^{10}\mathbf{g}_L^{n-1,0} \quad (3.39)$$

or equivalently

$$\mathbf{g}_L^{n0} = t_0\mathbf{g}_L^{n-1,0} + \tilde{t}_0\mathbf{g}_L^{n+1,0} \quad (3.40)$$

$$\mathbf{t}_0 = (\mathbf{E} - \mathbf{H}_L^{00})^{-1}\mathbf{H}_L^{10} \quad (3.41a)$$

$$\tilde{\mathbf{t}}_0 = (\mathbf{E} - \mathbf{H}_L^{00})^{-1}\mathbf{H}_L^{10\dagger} \quad (3.41b)$$

Applying Eq. 3.40 recursively, one can derive the following relations and the transfer matrices  $\mathbf{T}$  and  $\bar{\mathbf{T}}$ :

$$\mathbf{g}_L^{10} = \mathbf{T}\mathbf{g}_L^{00} \quad (3.42a)$$

$$\mathbf{g}_L^{00} = \bar{\mathbf{T}}\mathbf{g}_L^{10} \quad (3.42b)$$

$$\mathbf{T} = \mathbf{t}_0 + \tilde{\mathbf{t}}\mathbf{t}_1 + \tilde{\mathbf{t}}_0\tilde{\mathbf{t}}_1\mathbf{t}_2 + \cdots + \tilde{\mathbf{t}}_0\tilde{\mathbf{t}}_1\tilde{\mathbf{t}}_2 \cdots \mathbf{t}_n \quad (3.43a)$$

$$\bar{\mathbf{T}} = \tilde{\mathbf{t}}_0 + \mathbf{t}_0\tilde{\mathbf{t}}_1 + \mathbf{t}_0\mathbf{t}_1\tilde{\mathbf{t}}_2 + \cdots + \mathbf{t}_0\mathbf{t}_1\mathbf{t}_2 \cdots \tilde{\mathbf{t}}_n \quad (3.43b)$$

where  $\mathbf{t}_i$  and  $\tilde{\mathbf{t}}_i$  are defined via the recursion formulas:

$$\mathbf{t}_i = (\mathbf{I} - \mathbf{t}_{i-1}\tilde{\mathbf{t}}_{i-1} - \tilde{\mathbf{t}}_{i-1}\mathbf{t}_{i-1})^{-1}\mathbf{t}_{i-1}^2 \quad (3.44a)$$

$$\tilde{\mathbf{t}}_i = (\mathbf{I} - \mathbf{t}_{i-1}\tilde{\mathbf{t}}_{i-1} - \tilde{\mathbf{t}}_{i-1}\mathbf{t}_{i-1})^{-1}\tilde{\mathbf{t}}_{i-1}^2 \quad (3.44b)$$

The process is repeated until  $\mathbf{t}_n$  and  $\tilde{\mathbf{t}}_n \leq \delta$  with  $\delta$  arbitrarily small. Usually only 5 or 6 iterations are required to converge  $\mathbf{T}$  and  $\bar{\mathbf{T}}$ .

Finally, the surface Green's function is

$$\mathbf{g}_L^{00} = (\mathbf{E} - \mathbf{H}_L^{00} - \mathbf{H}_L^{10\dagger}\mathbf{T})^{-1} \quad (3.45)$$

### 3.2.4 Transmission probability in the Greens' function representation

We have introduced the matrix Green's function for the LCR system, and shown how to convert the infinite-dimensional problem into finite matrix manipulations. We are now in the position to derive the the Fisher-Lee formula, Eq. 3.19, in the Green's function representation to show the full power and elegance of this method [40].

Consider again the tight-binding Hamiltonian of Eq. 3.23. The Shrödinger equation can be written in the following form

$$\begin{pmatrix} \mathbf{H}_L & \mathbf{H}_{LC} & 0 \\ \mathbf{H}_{LC}^\dagger & \mathbf{H}_C & \mathbf{H}_{CR} \\ 0 & \mathbf{H}_{CR}^\dagger & \mathbf{H}_R \end{pmatrix} \begin{pmatrix} \Psi_L \\ \Psi_C \\ \Psi_R \end{pmatrix} = E \begin{pmatrix} \Psi_L \\ \Psi_C \\ \Psi_R \end{pmatrix} \quad (3.46)$$

where  $\Psi_L = \Psi_L^0 + \Psi_L^r$ .  $\Psi_L^0$  is the "incoming wave" and is the eigenstate of  $\mathbf{H}_L$  with energy  $E$ , i.e.  $\mathbf{H}_L\Psi_L^0 = E\Psi_L^0$ .  $\Psi_L^r$  is the reflected wave and  $\Psi_R$  is the transmitted wave. With these conditions one can solve the scattering state as

$$\Psi_L = (1 + \mathbf{G}_L \mathbf{H}_{HS} \mathbf{G}_C^r \mathbf{H}_{LS}^\dagger) \Psi_L^0 \quad (3.47a)$$

$$\Psi_S = \mathbf{G}_R \mathbf{H}_{RS} \mathbf{G}_C^r \mathbf{H}_{LS}^\dagger \Psi_L^0 \quad (3.47b)$$

$$\Psi_R = \mathbf{G}_C^r \mathbf{H}_{LS}^\dagger \Psi_L^0 \quad (3.47c)$$

The current carried by this left-incident scattering state is

$$j_{L \rightarrow R} = -e \frac{\partial}{\partial t} \langle \Psi_R | \Psi_R \rangle = -e \left( \frac{\partial \langle \Psi_R |}{\partial t} | \Psi_R \rangle + \langle \Psi_R | \frac{\partial | \Psi_R \rangle}{\partial t} \right) \quad (3.48)$$

From  $H\Psi = i\hbar \frac{\partial}{\partial t} \Psi$  and Eq. 3.46, one can find the current to be

$$j_{L \rightarrow R} = \frac{ie}{\hbar} \left( \Psi_L^\dagger \mathbf{H}_{LS} \Psi_S - \Psi_S^\dagger \mathbf{H}_{LS}^\dagger \Psi_L \right) \quad (3.49)$$

Inserting in these expressions the solutions given in Eq. 3.47, we have

$$\begin{aligned} j_{L \rightarrow R} &= \frac{ie}{\hbar} \left( \Psi_L^\dagger \mathbf{H}_{LS} \Psi_S - \Psi_S^\dagger \mathbf{H}_{LS}^\dagger \Psi_L \right) \\ &= \frac{ie}{\hbar} \left( \Psi_L^{0\dagger} \mathbf{H}_{LS} \mathbf{G}_C^a \mathbf{H}_{RS}^\dagger \left( \mathbf{G}_R^\dagger - \mathbf{G}_R \right) \mathbf{H}_{RS} \mathbf{G}_C^r \mathbf{H}_{LS}^\dagger \Psi_L^0 \right) \\ &= -\frac{e}{\hbar} \left( \Psi_L^{0\dagger} \mathbf{H}_{LS} \mathbf{G}_C^a \Gamma_R \mathbf{G}_C^r \mathbf{H}_{LS}^\dagger \Psi_L^0 \right) \end{aligned} \quad (3.50)$$

Eq. 3.50 is the current for this specific scattering state. For total current one needs to sum up this current from all left-incident transverse modes at a given energy. From Eq. 3.15 and Eq. 3.17, the transmission function is related to the current by

$$\begin{aligned}
T(E) &= \frac{\hbar}{e} j_{L,R} = 2\pi \sum_{\lambda} \delta(E - E_{\lambda}) \left( \Psi_{L\lambda}^{0\dagger} \mathbf{H}_{LS} \mathbf{G}_C^a \mathbf{\Gamma}_R \mathbf{G}_C^r \mathbf{H}_{LS}^{\dagger} \Psi_{L\lambda}^0 \right) \\
&= 2\pi \sum_{\lambda} \delta(E - E_{\lambda}) \left( \Psi_{L\lambda}^{0\dagger} \mathbf{H}_{LS} \left( \sum_i \phi_i \phi_i^{\dagger} \right) \mathbf{G}_C^a \mathbf{\Gamma}_R \mathbf{G}_C^r \mathbf{H}_{LS}^{\dagger} \Psi_{L\lambda}^0 \right) \\
&= 2\pi \sum_{\lambda} \sum_i \delta(E - E_{\lambda}) \left( \phi_i^{\dagger} \mathbf{G}_C^a \mathbf{\Gamma}_R \mathbf{G}_C^r \mathbf{H}_{LS}^{\dagger} \Psi_{L\lambda}^0 \right) \left( \Psi_{L\lambda}^{0\dagger} \mathbf{H}_{LS} \phi_i \right) \\
&= \sum_i \left( \phi_i^{\dagger} \mathbf{G}_C^a \mathbf{\Gamma}_R \mathbf{G}_C^r \mathbf{H}_{LS}^{\dagger} \left( 2\pi \sum_{\lambda} \delta(E - E_{\lambda}) \Psi_{L\lambda}^0 \Psi_{L\lambda}^{0\dagger} \right) \mathbf{H}_{LS} \phi_i \right) \quad (3.51)
\end{aligned}$$

Recall that the Green's functions can also be expressed in terms of eigenvectors of the system:

$$G^r = \sum_{\lambda} \frac{\psi_{\lambda} \psi_{\lambda}^{\dagger}}{E - E_{\lambda} + i\eta} \quad (3.52a)$$

$$G^a = \sum_{\lambda} \frac{\psi_{\lambda} \psi_{\lambda}^{\dagger}}{E - E_{\lambda} - i\eta} \quad (3.52b)$$

Using the SokhatskyWeierstrass theorem

$$\frac{1}{x + i\eta} = P(1/x) - i\pi\delta(x) \quad (3.53)$$

$$P(1/x) = \lim_{\delta \rightarrow 0} \left[ \int_{-\infty}^{\delta} \frac{1}{x} dx + \int_{\delta}^{\infty} \frac{1}{x} dx \right] \quad (3.54)$$

We can get

$$(G^a - G^r) = i2\pi\delta(E - E_{\lambda}) \quad (3.55)$$

Part of the right-hand side of Eq. 3.51 becomes

$$\mathbf{H}_{LS}^{\dagger} \left( 2\pi \sum_{\lambda} \delta(E - E_{\lambda}) \Psi_{L\lambda}^0 \Psi_{L\lambda}^{0\dagger} \right) \mathbf{H}_{LS} = -i\mathbf{H}_{LS}^{\dagger} (\mathbf{G}_L^a - \mathbf{G}_L^r) \mathbf{H}_{LS} = \Gamma_L \quad (3.56)$$

Finally Eq. 3.51 can be rewritten as

$$T(E) = \text{Tr}(\Gamma_L \mathbf{G}_C^a \Gamma_R \mathbf{G}_C^r) \quad (3.57)$$

and we have the Fisher-Lee formula in the Greens' function representation [40]

$$G(E) = \frac{2e^2}{h} T(E) = \frac{2e^2}{h} \text{Tr}(\Gamma_L \mathbf{G}_C^a \Gamma_R \mathbf{G}_C^r) \quad (3.58)$$

### 3.2.5 Eigenchannel analysis

In scattering theory, the  $\mathbf{S}$  matrix is usually represented in the basis of the Bloch wavefunctions of the left and right electrodes (or plane waves for free-electron electrodes). In Sec. 3.1.1 we have shown in Eq. 3.14 that one can diagonalize  $\mathbf{t}^\dagger \mathbf{t}$  and get a set of non-mixing *eigenchannels*, each with a well-defined transmission probability

$$\mathbf{U}_L^\dagger \mathbf{t}^\dagger \mathbf{t} \mathbf{U}_L = \text{diag}\{T_n\} \quad (3.59)$$

The eigenvectors of  $\mathbf{t}^\dagger \mathbf{t}$  given by the columns of the unitary matrix  $\mathbf{U}_L [N_L \times N_L]$  are linear combinations of the incoming wavefunctions from the left, and represent a new set of eigenchannel wavefunctions with well defined transmission probabilities,  $0 \leq T_n \leq 1$ . The individual eigenchannel transmissions add up to the total transmission  $T = \sum_n T_n$ . One can also define a rectangular unitary matrix  $\mathbf{U}_R [N_R \times N_L]$  for the right lead such that

$$\mathbf{U}_R^\dagger \mathbf{t} \mathbf{U}_L = \text{diag}\{\sqrt{T_n}\} \quad (3.60)$$

The columns of  $\mathbf{U}_R$  represent the *outgoing* part of the eigenchannel wavefunctions at the right, formed by mixing the Bloch wavefunctions of the right lead, with a one-to-one correspondence to the *incoming* channels at the left as shown in columns of  $\mathbf{U}_L$ .

The eigenchannel decomposition has the advantage of breaking up the transmission into a set of "non-mixing" channels and thus the total transmission is the direct sum of all contribution without any cross (interference) terms. Alternatively one can also diagonalize the rectangular matrices  $\mathbf{t}^\dagger$  and  $\mathbf{t}$  using single value decomposition:

$$\mathbf{t}^\dagger = \mathbf{U}_R \mathbf{D} \mathbf{U}_L \text{ and } \mathbf{t} = \mathbf{U}_L^\dagger \mathbf{D}^\dagger \mathbf{U}_R^\dagger \quad (3.61)$$

The norm of the eigenvalues of the complex diagonal matrix gives the transmission  $\mathbf{D} \mathbf{D}^\dagger = \mathbf{D}^\dagger \mathbf{D} = \text{diag}\{T_n\}$ , and the phase information for the transmitted waves are retained as  $\theta_n = \arg(D_n)$ .

Scattering theory assumes no knowledge about the scattering region and only gives the description of the incoming and outgoing waves far from the scattering center. The Green's function's method, on the other hand, works in the device subspace without solving for the scattering states in the leads. To relate the two one must recover the implicit scattering states within the device subspace. It can be shown that the spectral function of the device region can be written as the sum of the left and right contribution [41]:

$$\mathbf{A}_C = i(\mathbf{G}_C - \mathbf{G}_C^\dagger) = i\mathbf{G}_C(\mathbf{G}_C^{\dagger-1} - \mathbf{G}_C^{-1})\mathbf{G}_C^\dagger = \mathbf{G}_C \mathbf{\Gamma}_L \mathbf{G}_C^\dagger + \mathbf{G}_C \mathbf{\Gamma}_R \mathbf{G}_C^\dagger = \mathbf{A}_L + \mathbf{A}_R \quad (3.62)$$

where  $\mathbf{A}_{L,R} = \mathbf{G}_C \mathbf{\Gamma}_{L,R} \mathbf{G}_C^\dagger$  represents the projection of the scattering states with left and right incoming waves onto the device region. Diagonalization of the transmission matrix  $\mathbf{t}^\dagger \mathbf{t}$  in the left lead space is equivalent to diagonalization in the eigenbasis of  $\mathbf{A}_L$ . It was shown that the eigenchannel transmissions and wavefunctions in the device region can be obtained by diagonalization of the Hermitianized matrix [41]:

$$T(E) = \text{Tr}(\mathbf{\Gamma}_L \mathbf{G}_C^a \mathbf{\Gamma}_R \mathbf{G}_C^r) = \text{Tr}((\mathbf{G}_C^r \mathbf{\Gamma}_L \mathbf{G}_C^a)^{\frac{1}{2}} \mathbf{\Gamma}_R (\mathbf{G}_C^a \mathbf{\Gamma}_L \mathbf{G}_C^r)^{\frac{1}{2}}) \quad (3.63)$$



$$\mathbf{U}((\mathbf{G}_C^r \mathbf{\Gamma}_L \mathbf{G}_C^a)^{\frac{1}{2}} \mathbf{\Gamma}_R (\mathbf{G}_C^a \mathbf{\Gamma}_L \mathbf{G}_C^r)^{\frac{1}{2}}) \mathbf{U}^\dagger = \text{diag}\{\sqrt{T_n}\} \quad (3.64)$$



## Chapter 4

# Quantum Interference Effect and Conductance Switching of Porphyrins Controlled by Hydrogen Tautomerization

### 4.1 Quantum interference effect in single molecule transport

One of the main interests in single molecule electronics is to employ the wave nature of the electron to control current flow in nanoscale devices. The interference effects in transport through aromatic systems, in particular the prototypical example, benzene, have been studied both experimentally [42, 43] and theoretically [44, 45, 46, 47]. The transmission of benzene varies by orders of magnitude when relative orientation of thiol disubstitution is changed from para, ortho, to meta. In transport theory, it is known that for single molecules, transmission at the Fermi level is dominated by the tunneling mechanism in which the transmission coefficient  $T$  decays exponentially with electrode spacing,  $T \propto e^{-\beta L}$ , and the decay constant  $\beta$  is proportional to the gap between HOMO and LUMO,  $\sqrt{\frac{E_{LUMO} - E_{HOMO}}{2}}$  [48]. Since the HOMO - LUMO gap is

affected negligibly for all three systems in dithiobenzene, one may naively expect the transmission ordering to be ortho > meta > para based on the tunneling length between the two electrodes. Nevertheless, both experiments and theory have confirmed that the transmission follows the order of para  $\sim$  ortho  $\gg$  meta.

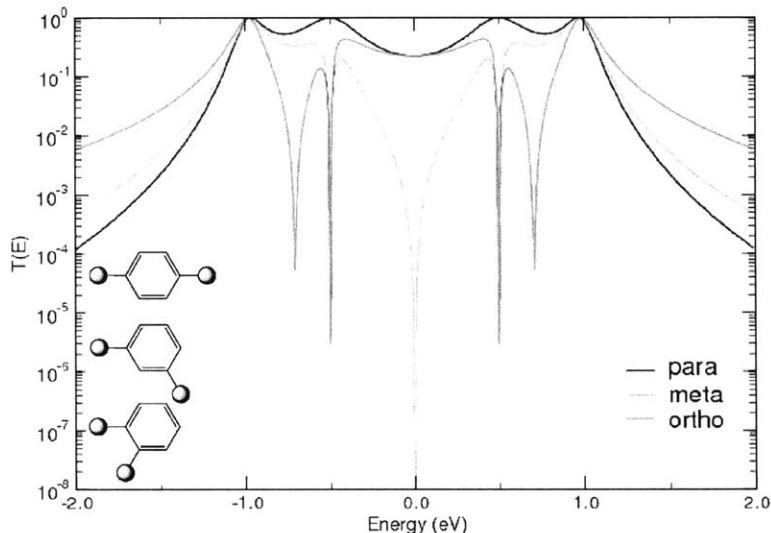


Figure 4-1: Transmission of the benzene molecule calculated within the Hückel model with different electrode connections. The on-site energies and the hopping terms for the  $p_z$  orbitals are set to 0.0 and -0.5 eV, respectively. The coupling element between the lead and the molecule is also set to be -0.5 eV.

#### 4.1.1 The orbital view interpretation

This effect is generally attributed to the so-called *quantum interference* effect, which implies that the electron goes through the molecule via multiple paths and the phase difference between different paths determines constructive or destructive interference for the transmitted wavefunctions, as in common wave interference experiments. Nevertheless, the “branch current” interpretation is hardly applicable to molecular systems since the wavefunctions span the entire molecule and are not limited within

certain parts of the molecule as the current flows through. The origin of the quantum interference effect is essentially embedded in the underlying molecular symmetry and the inherent electronic structure, and more specifically, the phase and the amplitude of the frontier orbitals on the anchoring atoms linking the molecule to the electrodes [49]. In the *orbital view interpretation* proposed by Yoshizawa *et. al.* [49], the Green's function of the central region for a weak coupling system is approximated by the zeroth-order Green's function, which neglects the effect of lead self-energies, and is expanded in terms of the molecular orbital basis  $|i\rangle$  of the molecule:

$$G^{(0)}(E) = \sum_i \frac{|i\rangle\langle i|}{E + i\eta - \epsilon_i} \quad (4.1)$$

where  $\epsilon_i$  runs over all molecular orbital eigenenergies. Transforming to the localized atomic orbital basis, we can get the Green's function element between the linkage  $r$ -th and  $s$ -th atomic orbitals to be

$$G_{rs}^{(0)}(E) = \sum_i \frac{c_{ri}c_{si}^*}{E + i\eta - \epsilon_i} \quad (4.2)$$

where  $c_{ri}$  is the  $i$ th molecular orbital expansion coefficient for the  $r$ th atomic orbital. Assuming the Fermi energy to be at the midgap between HOMO and LUMO, for polyaromatic hydrocarbons (PAH) such as benzene, the occupied and unoccupied orbitals are symmetric with respect to the Fermi level in terms of energy and AO composition. It is then straight forward to show that the transmission at the Fermi energy solely depends on the relative sign of  $c_{ri}$  and  $c_{si}$  of the HOMO- $n$  and LUMO+ $n$  orbital pairs:

$$G_{rs}^{(0)}(E) = \left( \frac{c_{r,homo}c_{s,homo}^*}{E_F + i\eta - \epsilon_{homo}} + \frac{c_{r,lumo}c_{s,lumo}^*}{E_F + i\eta - \epsilon_{lumo}} \right) + \left( \frac{c_{r,homo-1}c_{s,homo-1}^*}{E_F + i\eta - \epsilon_{homo-1}} + \frac{c_{r,lumo+1}c_{s,lumo+1}^*}{E_F + i\eta - \epsilon_{lumo+1}} \right) + \dots \quad (4.3)$$

If the  $C_{rHOMO}C_{sHOMO}^*$  has the same sign as  $C_{rLUMO}C_{sLUMO}^*$ , each pair inside the brackets cancels out and  $G_{rs}$  equals to zero, as in the case of meta-benzene shown in Fig. 4-2

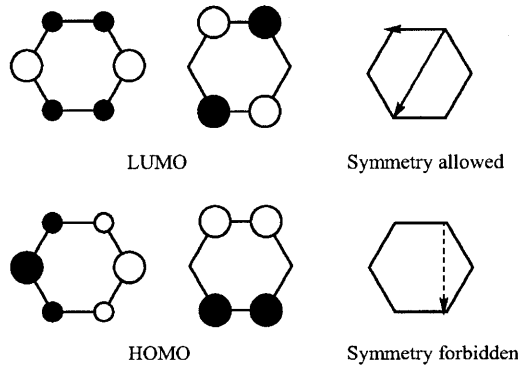


Figure 4-2: Frontier orbitals of benzene and symmetry-allowed/forbidden routes for electron transmission.

### 4.1.2 Molecular conductance orbital analysis

A different approach to interpret the quantum interference effect known as the *molecular conductance orbital (MCO) analysis* has also been proposed [47]. Different from the eigenchannel analysis, which has the advantage that by mixing orbitals one acquires a set of non-mixing transmission channels with no cross terms, the MCO analysis decomposes the transmission into the contributions from each molecular orbital. As the name implies, molecular conductance orbitals resemble molecular orbitals of the discrete molecular systems, but also account for lead-molecule interactions. In other words, molecular conductance orbitals are the eigenvectors of the

effective Hamiltonian  $H_{eff} = H_C + \Sigma_L + \Sigma_R$ , or equivalently, the eigenvectors of the Green's function  $G^r = (E - H_{eff})^{-1}$ . Since the self-energy terms are not Hermitian, molecular conductance orbitals are generally complex, but still retain the one-to-one correspondence to the unperturbed molecular orbitals. This is seen by first rewriting the coupling functions  $\Gamma_L$  into

$$\Gamma_L = h_{CL} \left( i(g_L^{00} - g_L^{00\dagger}) \right) h_{LC} = \left( h_{CL} a_L^{\frac{1}{2}} \right) \left( a_L^{\frac{1}{2}} h_{LC} \right) = \gamma_L \gamma_L^\dagger \quad (4.4)$$

and similarly for the right lead; here  $a_{L,R}$  is the spectral function of the leads. In the matrix representation  $\gamma_{L(R)} = \mathbf{h}_{CL(R)} \mathbf{a}_{L(R)}^{1/2}$  is a rectangular matrix with dimension  $L(R) \times C$ . Transmission can then be rearranged in the following form

$$\begin{aligned} T(E) &= \text{Tr}[\Gamma_L G^r \Gamma_R G^a] = \text{Tr}[\gamma_L \gamma_L^\dagger G^r \gamma_R \gamma_R^\dagger G^a] \\ &= \text{Tr} \left[ \left( \gamma_L^\dagger G^r \gamma_R \right) \left( \gamma_R^\dagger G^a \gamma_L \right) \right] = \text{Tr}(\mathbf{t}^\dagger \mathbf{t}) \quad (4.5) \end{aligned}$$

A new transmission matrix with dimension  $L \times R$  can then be defined as  $\mathbf{t}^\dagger = \gamma_L^\dagger G^r \gamma_R$ . The matrix element  $t_{\alpha\beta}^\dagger(E)$  represents the transmission coefficient from the  $\alpha$ -th orbital in the left lead to the  $\beta$ -th orbital in the right lead and the total transmission  $T = \sum_{\alpha\beta} |t_{\alpha\beta}^\dagger|^2$  is a sum over all lead orbital transmissions.

We can do a further simplification by adopting the wide band limit (WBL) approximation for the lead, in which the self-energy of the lead can be represented by a constant imaginary number, and  $\mathbf{t}$  essentially has dimension one by one and becomes a number. Following the notation used in the previous orbital view discussions, if we assume that the central region is connected to the left and right leads only through the  $r$ -th and  $s$ -th orbitals respectively, then the  $\gamma_L^\dagger$  and  $\gamma_R$  matrices have only one nonzero element each,  $(\gamma_L^\dagger)_{1r} = \sqrt{\gamma_L}$  and  $(\gamma_R)_{s1} = \sqrt{\gamma_R}$ . Matrix multiplication then reduces to

$$\mathbf{t}^\dagger = \mathbf{t}^\dagger = \sqrt{\gamma_L}(G^r)_{rs}\sqrt{\gamma_R} = \sqrt{\gamma_L\gamma_R}G_{rs}^r(E) = \sqrt{\gamma_L\gamma_R}\sum_i \frac{c_{ri}c_{si}^*}{E+i\eta-\epsilon_i} = \sum_i t_i \quad (4.6)$$

One can immediately see the similarity of the above formulae to Eq. 4.2, except that instead of expanding in *molecular* orbitals. Eq. 4.6 contains full lead coupling effect and is expanded in terms of the *molecular conductance* orbitals, while  $\epsilon_i$ ,  $c_{ri}$  are generally complex rather than real numbers, as in the zero-th order Green's function expansion. In the limit that electrode coupling goes to zero, the MCO analysis is reduced to the simple orbital view of Sec. 4.1.1. Also note that the transmission probability  $T = |t|^2 = |t_1|^2 + |t_2|^2 + \dots + t_1 t_2^* + t_1^* t_2 + \dots$  now contains the cross terms which naturally rationalize the interference effect from the molecular orbital point of view.

## 4.2 Quantum interference effect in porphyrins

The discovery of the quantum interference effect has raised a lot of interest in designing single molecular switches as functional electrical elements towards the miniaturization of electronic circuits. A transformation based on isomerization [50], bond cleavage [51] or an electrochemical reaction [52] often induces a change in molecular symmetry which can in turn cause a change in transmission by orders of magnitude. A quantum interference effect transistor (QUIET) [45] was recently proposed in which the destructive interference of meta-connected benzene can be controlled by decoherence and/or elastic scattering introduced by a third voltage probe or a side group. Nonetheless, most of the proposed strategies to date remain at the “conceptual” stage, either lacking controllable means or involving drastic conformational changes that are incompatible with device setup. An ideal molecular switch, other than being bistable and reversible, should have similar molecular frames and binding strengths to the substrate before and after the switching event. These criteria can be fulfilled by



the recently discovered hydrogen tautomerization reaction in naphthalocyanin [53], in which the tautomerization reaction was induced by electron injection through a STM tip under a bias voltage above the LUMO resonance, and can even be coupled to neighboring molecules in an assembly. It would be interesting to investigate if the aromatic porphyrin families as shown in Fig. 4-3, whose small bandgaps and planar structures make them a perfect candidate for nanoscale device fabrication, also possess the quantum interference characteristic that can be accurately maneuvered by the hydrogen tautomerization reaction.

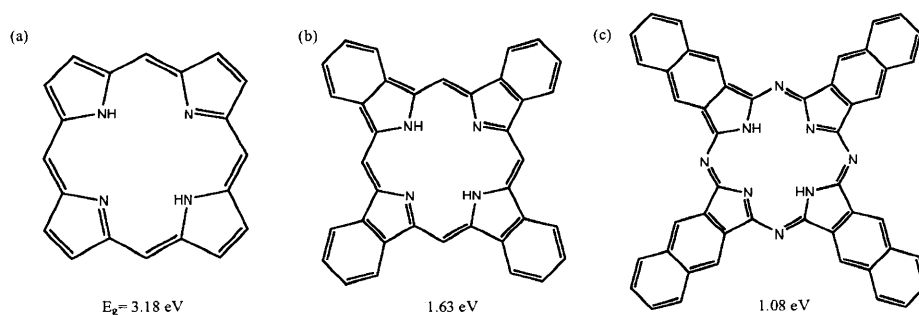


Figure 4-3: The porphyrin family molecules: (a) porphyrin (b) tetrabenzoporphyrin and (c) naphthalocyanin considered in this study. Also shown here are the HOMO-LUMO gaps calculated with the PBE functional and 30/360 Ry cutoffs for plane wave basis. It has been shown that the hydrogen tautomerization of (c) can be controlled by a STM tip.

We first examine the symmetry of the frontier orbitals of the  $D_{2h}$  symmetric porphyrin molecule. As shown in Fig. 4-4, the HOMO has  $a_1$  symmetry with respect to both  $yz$  and  $xz$  planes and the almost degenerate LUMO and LUMO+1 orbitals have the same nodal structure but are rotated by 90 degrees with respect to each other as have been previously observed in STM measurement [53]. Considering the shape of molecular frame and the most possible connection points common to all porphyrin family molecules, we first look at four possible connection paths to the left and right electrodes, namely  $AB$ ,  $AC$ ,  $DE$ , and  $DF$ . A close examination at the relative phase and magnitude of the  $p_z$  orbital coefficient in the frontier orbitals indicates that only in the  $AB$  connection there might exist a destructive interference

near the Fermi level since  $c_{A,HOMO}c_{B,HOMO}^*$  and  $c_{A,LUMO}c_{B,LUMO}^*$  have the same sign, while all the other connections have opposite signs for the two products and therefore interfere constructively. Note that although porphyrins do not belong to the PAH family and therefore do not have the symmetry between the occupied and unoccupied  $\pi$  orbitals, the HOMO and LUMO terms are still the dominant contribution in Eq. 4.2 since all the non-zero terms are much smaller and merely shift the position of the conductance dip. Using Eq. 4.2 and considering only the HOMO and LUMO orbital pairs, a transmission zero can be predicted for an  $AB$  connection to lie at  $E = -3.84$  eV, only  $-0.6$  eV away from the midgap Fermi level.

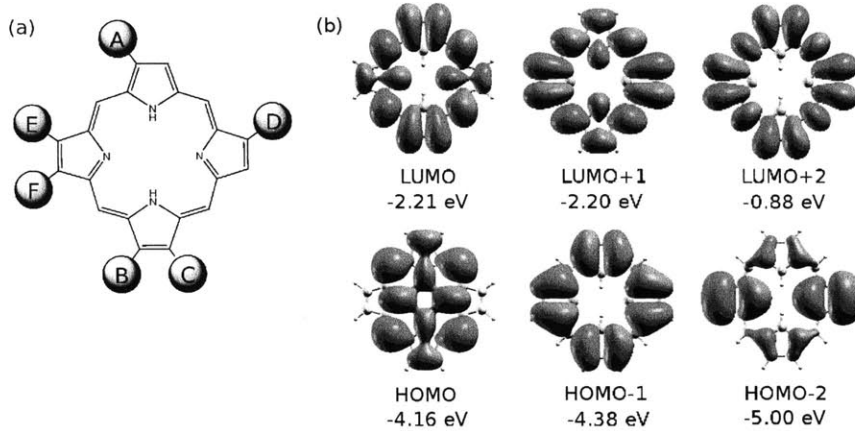


Figure 4-4: (a) the connection sites of porphyrin to the left or right electrodes considered in this study and (b) the positions and wavefunctions of the frontier molecular orbitals of porphyrin.

#### 4.2.1 Transport properties of porphyrin family molecules

We perform the NEGF calculation in the zero-bias limit to find the transport properties for all possible paths between  $A - F$  connection sites. The electronic structure of the molecular part is first calculated with plane wave basis under periodic boundary conditions and then a unitary transformation to maximally-localized Wannier functions (MLWF) is performed to obtain the smallest possible orthogonal localized

basis set that is compatible with the lead-conductor-lead formalism of the Green's function's method. In order to represent in the MLWF basis not only the occupied manifold but also  $\pi^*$  orbitals close to the Fermi level that are relevant to the transmission, we include unoccupied states up to 10 eV above HOMO, and followed the disentanglement procedure to separate localized molecular states from diffuse Rydberg states. A selection of the MLWF orbitals for a porphyrin are shown in Fig. 4-5. An  $s$ -like orbital is located in the middle of all  $\sigma$  bonds and a  $p_z$  orbital are recovered for all carbon atoms, as well as the nitrogen atoms in the pyrrole moiety. For the other pair of nitrogen atoms the  $p_z$  orbital is found to hybridize with the long pair and give rise to two  $sp^3$  long pair orbitals. In any case, the transformed MLWF basis set accurately reproduces the electronic structure of the porphyrin and all molecular orbital eigenenergies up to 5 eV above the HOMO level. For the lead part we adopt the wide band limit (WBL) approximation. It is known that the use of WBL approximation is applicable to Au leads since the density of states of gold is quite flat around the Fermi energy [44]. The self-energy of the lead can be represented by a constant imaginary number,  $\Sigma_{L,R} = -i\frac{\gamma_{L,R}}{2}|\alpha_{L,R}\rangle\langle\alpha_{L,R}|$  where  $|\alpha_{L,R}\rangle$  is the  $p_z$  orbital of the linkage carbon atom, and the coupling constant  $\gamma_{L,R}$  is set to be 0.5 eV, following typical estimates in other studies [45].

The transmission function for porphyrin, tetrabenzoporphyrin and naphthalocyanin with the wide-band-limit approximation are shown in Fig. 4-6. Conforming to what we have expected, a transmission zero appears for the  $AB$ -path within 1 eV from the Fermi level for all three systems, and there are some other transmission paths, for example,  $BD$  and  $AD$ , that show strong destructive interference effect near the Fermi level. Since these transmission zeros are all rather accessible, an electrical switch can simply be made by applying a gate voltage to tune the position of the Fermi level [54]. More excitingly, the specific symmetry of the porphyrin-family molecules allows for another degree of freedom. Upon hydrogen tautomerization, the  $AB$ -path and  $DE$ -path change into one another and same for  $AD$  and  $BE$  (Table.4.1). If a gate voltage can be applied to the molecule to tune the Fermi level to the energy where a

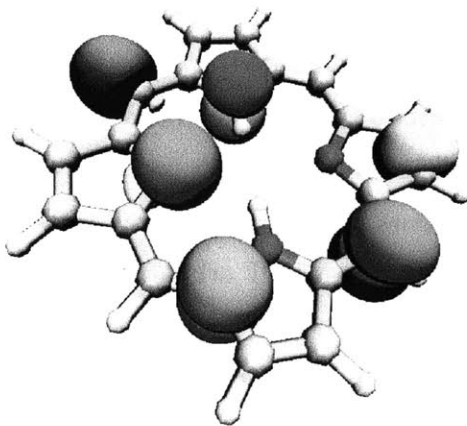


Figure 4-5: Selected orbitals of the MLWF basis of porphyrin. An  $s$ -like orbital is located in the middle of all  $\sigma$  bonds and a  $p_z$  orbital are recovered for all carbon atoms, as well as the nitrogen atoms in the pyrrole moiety. For the other pair of nitrogen atoms involved in  $\pi$  molecular orbitals, the  $p_z$  orbital is found to hybridize with the long pair and give rise to two  $sp^3$  like orbitals.

transmission zero occurs, what is non-conducting ( $AB$  or  $AD$ ) becomes conducting ( $DE$  or  $AF$ ) after the tautomerization, and vice versa, differing by orders of magnitude as in an ideal electrical switch. Even without any gate voltage fine-tuning, at the Fermi energy the transmission between  $AD$  and  $BE$  already differs by at least one order of magnitude caused by the nearby conductance dip.

$$\begin{array}{rcl}
 AB & \leftrightarrow & DE \\
 AC & \leftrightarrow & DF \\
 AD=CF & \leftrightarrow & BE=AF=CD \\
 AE & = & BF \\
 BD & = & CE
 \end{array}$$

Table 4.1: The equivalent paths of porphyrin-family molecules and their interconverting relationships upon hydrogen tautomerization

To quantify the molecular orbital contribution to the destructive interference, we perform the *molecular conductance orbital (MCO) analysis* following the procedure proposed by Solomons et.al [47]. We can now separate the contributions to the transmission from each of the molecular conductance orbitals. For a generic transmission

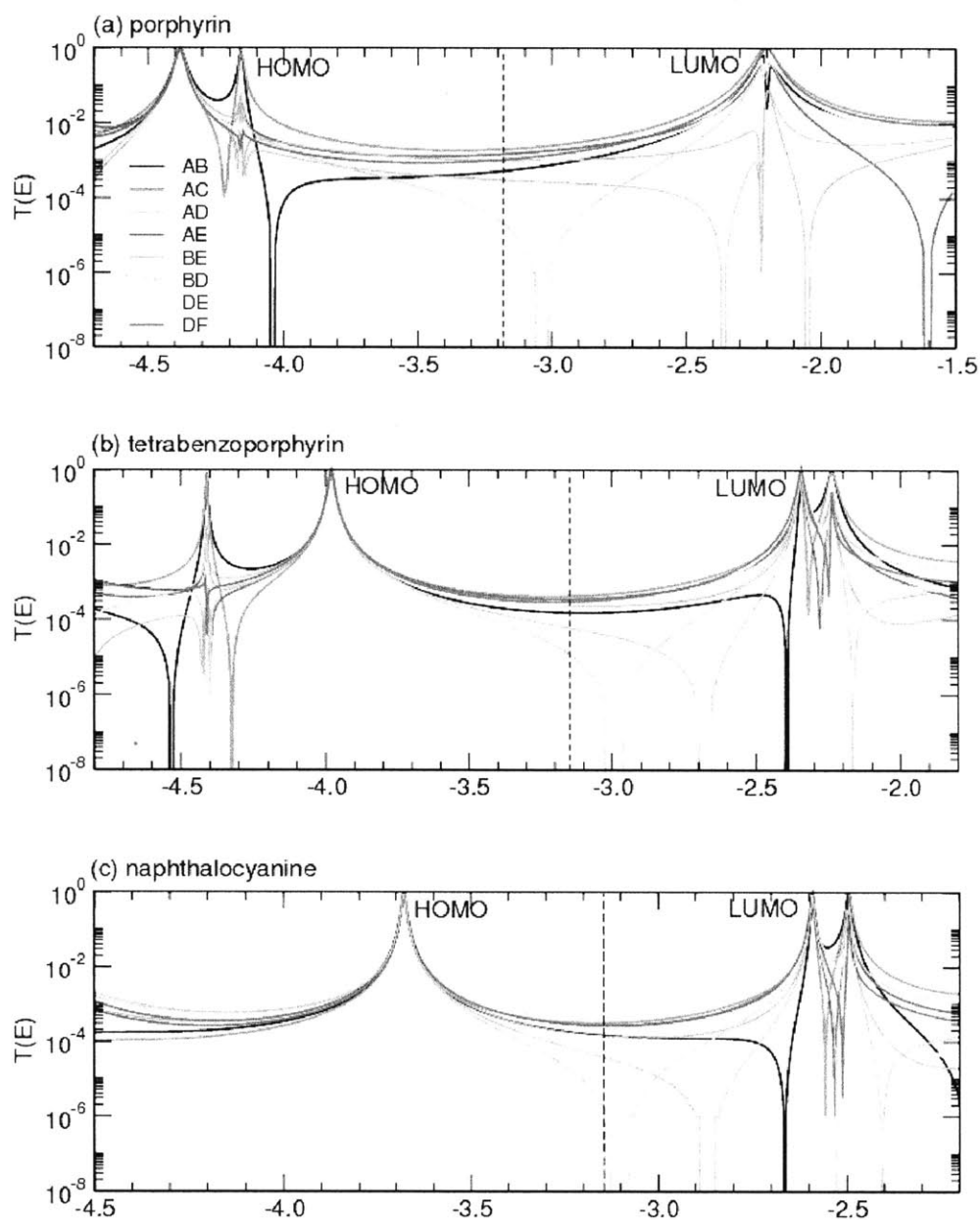


Figure 4-6: Transmission spectra calculated for (a) porphyrin (b) tetrabenzoporphyrin and (c) naphthalocyanine molecules with lead treated by WBL approximation and  $\gamma_{L,R} = 0.5$  eV. The linkage sites for different paths are labeled in Fig. 4-4(a). The midgap Fermi level is marked by the dashed vertical line.

zero, both the real and imaginary component of  $t$  summed over all MCO's has to be zero. Fig. 4-7 shows the real and imaginary parts of the coupling coefficient in  $AD$  and  $BE$  connections along with four biggest contributions from four nearest orbitals to the Fermi level, from HOMO-1 to LUMO+1. Whenever the energy sweeps across an MO energy, the real component crosses zero and the imaginary component shows a spike. Any other zeros shown in the real components that do not correspond to an MO energy level are caused by destructive interference. For the  $AD$ -path, both the real and imaginary components are equal to zero at around  $E = -2.8$  eV (the midgap Fermi level is around 3.2 eV), giving rise to an absolute transmission zero. In comparison, for the hydrogen tautomerized  $BE$ -path, the transmission always has finite values across the Fermi level. The coupling coefficients of the  $BD$ -path and  $AE$ -path are very similar for both real and imaginary components except for a few sign differences, revealing the close relationship between the two configurations, but differ slightly at absolute magnitude which makes a zero in one case but not the other.

### 4.2.2 Porphyrins assembled between carbon nanotubes

We want to emphasize that although the above calculations are calculated with the wide band approximation for the lead rather than the full LCR calculation including also the metal lead atomistic details, this simpler analysis does capture the majority of physics and is appropriate to describe and predict the transmission and interference effects near the Fermi level. The difference between the present calculation and a full LCR calculation would possibly come from the following: (1) the structural relaxation of the molecule, which does not alter the molecular symmetry properties in the absence of drastic distortion; (2) the lead-molecule coupling strength, which should affect the peak broadening and the transmission between two closely-spaced molecular orbitals (which does not happen at the Fermi level, but indeed happens between HOMO-1 and HOMO, or between LUMO and LUMO+1. ), and (3) inclusion of  $\sigma$  transmission, which would contribute extra non-zero terms to the  $\pi$  destructive interference but is generally much smaller than  $\pi$  transmission at the Fermi level.

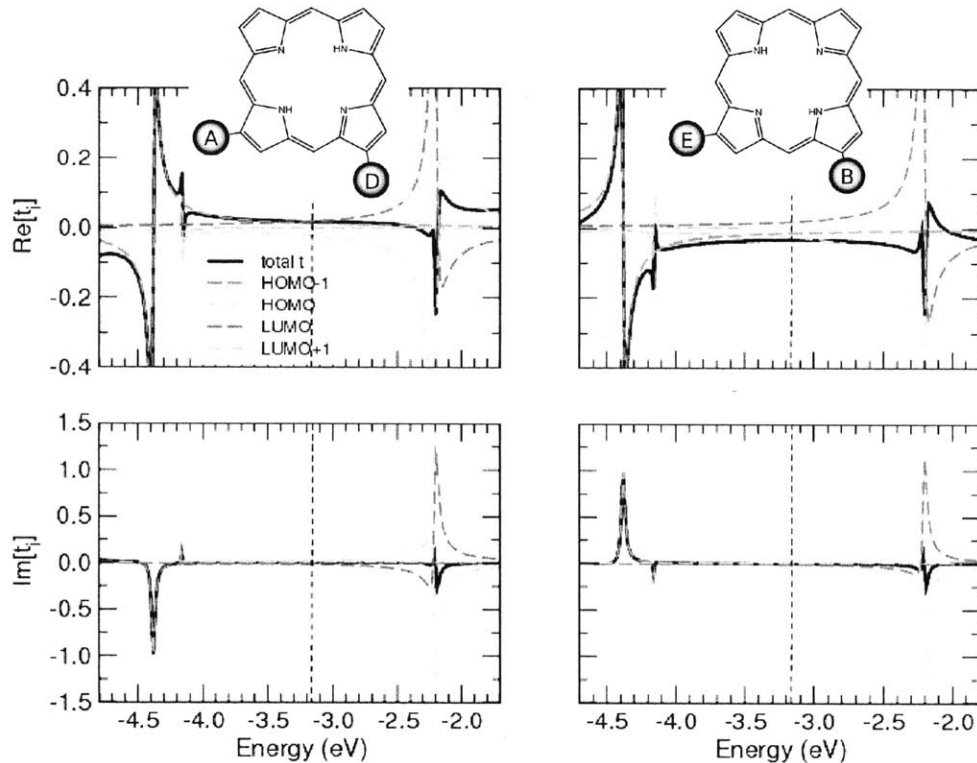


Figure 4-7: The real(top) and imaginary(bottom) contributions to the transmission from frontier molecular conductance orbitals of porphyrin linked to the leads through *AD*- (left) or *BE* path (right). The black curves are the sum of all contributions from all molecular conductance orbitals, and the contributions from HOMO-1(red), HOMO(green), LUMO(blue) to LUMO+1(orange) are shown in dashed curves.

As a comparison, we also perform the full atomistic calculation using metallic (5,5) CNT as the leads. Such systems have been made possible by the the recent experimental breakthrough in manufacturing a spatial gap in single-wall carbon nanotubes and assembling organic molecules in between two CNT electrodes [10, 55]. The optimized structures of our systems are shown in Fig. 4-8 for the *AB* and *AD* configurations. The porphyrin molecule is directly linked to a CNT edge atom, and an extra linkage through the alkyl groups is inserted to maintain a rough coplanar structure,

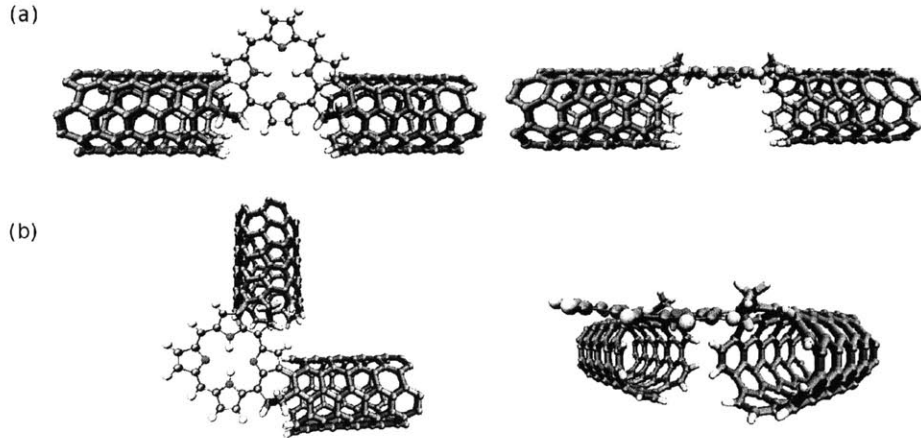


Figure 4-8: The top view and side view of optimized structures for (5,5)CNT-porphyrin-(5,5)CNT through (a)  $AB$ -path (or  $BD$ -path in case of hydrogen tautomerization inside the porphyrin) and (b)  $AD$ -path (or  $BE$ -path for hydrogen tautomerized porphyrin) The strong coupling between the and the porphyrin  $\pi$  orbital and the CNT  $p_z$  orbitals is indicated by the red bond.

which is known to provide good contact transparency. The transmission functions of the (5,5)CNT-porphyrin-(5,5)CNT junctions with different linkage configurations are shown in Fig. 4-9 along with the WBL counterparts shown in dashed curves. A high similarity can immediately be noticed between the full atomistic calculation and the one that contains only the porphyrin molecular Hamiltonian and a virtual lead. The strong molecule-lead  $\pi - \pi$  coupling results in larger peak broadening and, in general, higher transmissions at the Fermi energy. The absolute transmission zeros observed in the WBL approximation, which considers only pure  $\pi$  transmission, are smeared out in real CNT junctions due to  $\sigma$  contributions, but the overall shape and symmetry still closely resemble those calculated in the WBL approximation. The destructive interference “dip” is particularly apparent in the  $BD$  and  $AD$  configurations. In case of the  $AD$ ( $BE$ ) linkage to CNT electrodes, the hydrogen tautomerization could bring a conductance difference by two orders of magnitude. Comparing with previous theoretical studies on molecular switches assembled between carbon nanotubes [56], the system proposed in this study has the advantage that the switching mechanism



is well-established and has been proven to be viable experimentally.

### 4.3 Porphyrin as a molecular bit

Last, we would like to propose another potential application of conductance switching in porphyrins controlled by hydrogen tautomerization, that is, to serve as the smallest memory unit in a computer. As an attractive building block for supramolecular systems, porphyrins have long been considered as potential candidates in nanoelectronics [57]. Recently there has been a strong interest in developing multiporphyrinic systems with linear, cyclic, and cross-linked geometries through covalent or noncovalent linkage strategies. The synthesis of the tetrameric porphyrins has also been achieved in which four porphyrin units are linearly linked by three conjugated C-C bonds and form a square planar sheet [58]. The superb structure, stability and flexibility in terms of supramolecular assembly of the multiporphyrinic systems have inspired us to consider porphyrin as the smallest possible molecular bit with the "0" and "1" represented by the two hydrogen tautomeric states.

Take the 2-bit system made by a tape-porphyrin as shown in Fig. 4-10, the triply linked fused diporphyrin [59], for example, the combination of the hydrogen tautomeric states of each porphyrin gives rise to four memory states, 00, 01, 10, and 11. Depending on the contact structures and symmetry properties, the four states can be all uniquely defined or involve some degeneracies. The transmission functions of the tape-porphyrin via different connection paths are shown in Fig. 4-11. Some connections give more striking transmission difference between the three or four memory states, such as  $\beta\delta$ , but even in connections where a definite transmission zero near the Fermi level is missing, one can still easily differentiate memory states that differ by one order of magnitude in electrical conductance. A more complex multiporphyrinic system is likely to offer more striking difference between different memory states.

In summary, we have performed a detailed study of the quantum interference effect

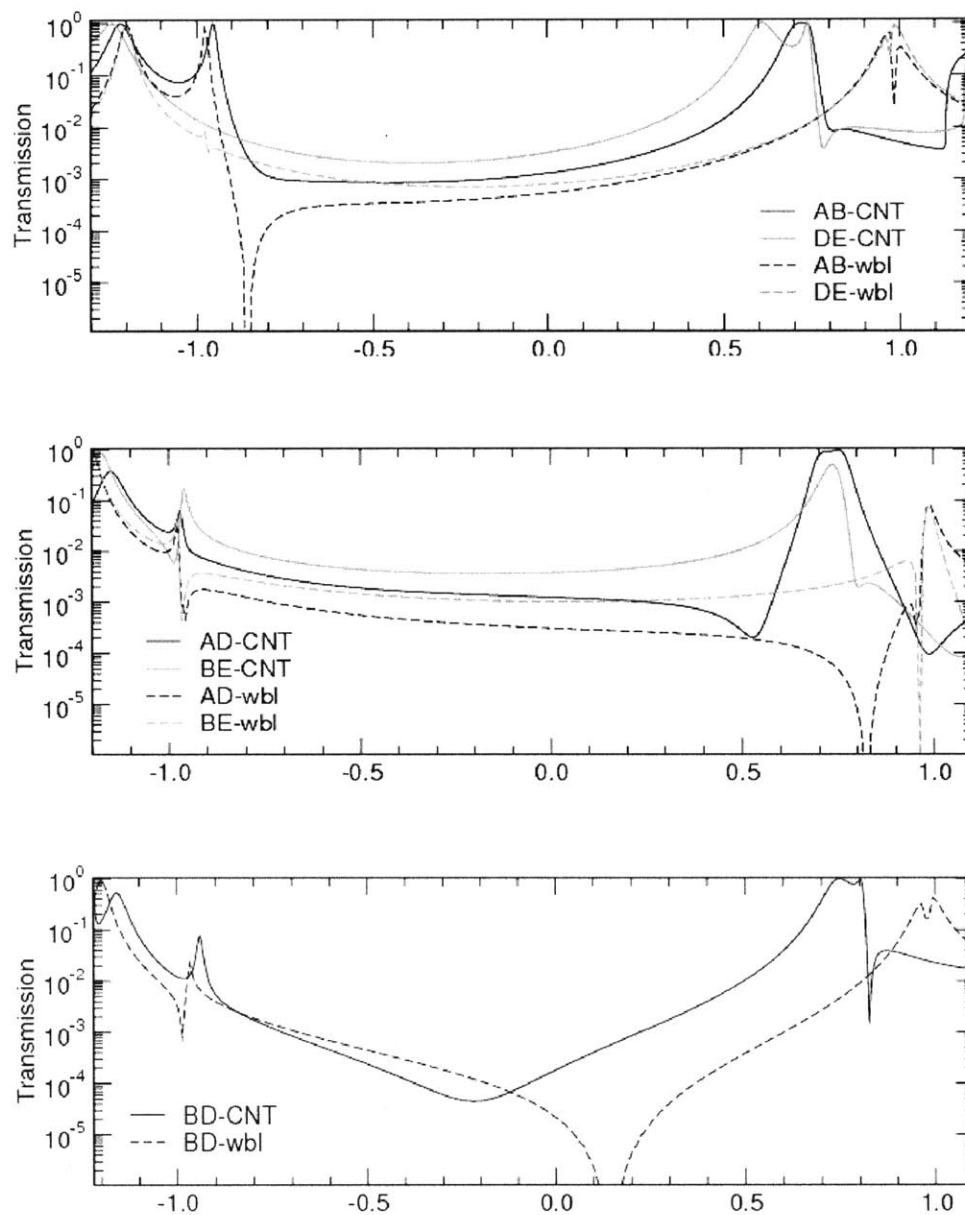


Figure 4-9: The transmission functions of (5,5)CNT-porphyrin-(5,5)CNT junctions with different linkage configurations from full DFT calculations and the lead self-energy treated atomistically. The corresponding curves of the same configurations calculated with only the porphyrin molecule and the lead part treated by wide-band-limit approximation are shown in dashed curves.

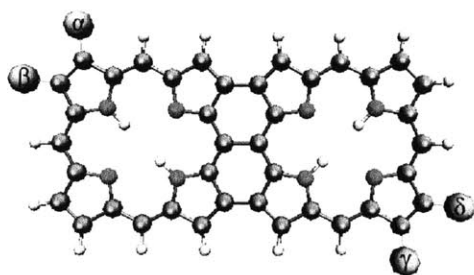


Figure 4-10: A 2-bit tape porphyrin system representing the "01" memory state ("0" and "1" for the hydrogen configuration for the left and right porphyrins, respectively).

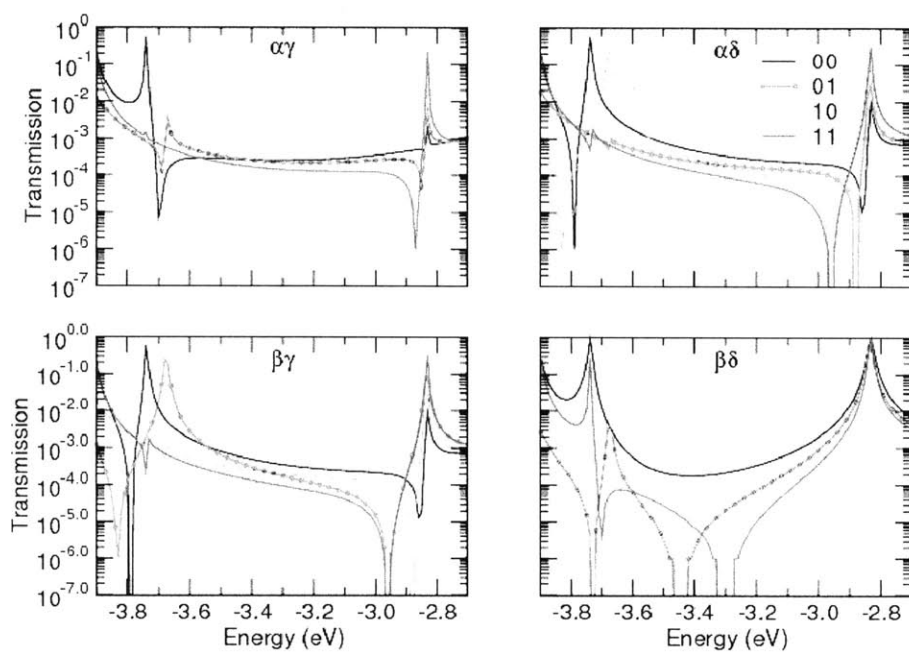


Figure 4-11: The transmission functions of four different memory states of the 2-bit tape porphyrin via different linkage sites as shown in Fig. 4-10

controlled by hydrogen tautomerization of porphyrinic systems. We have shown that a minimal Wannier basis transformation of the porphyrin system combined with WBL approximation for the lead part provide a simple and elegant approach in describ-

ing the transmission through different molecular connection points, and essentially captures all important physics without the expense of full-atomistic lead-molecule-lead calculations. The porphyrin molecule offers a variety of desirable features and is one of the most extensively studied macromolecules. Our study, based on the experimentally-proven hydrogen tautomerization mechanism, provides useful insight for important applications in molecular electronics: a fully controllable molecular switch and a memory unit, which awaits for experimental realization in the near future.

## Chapter 5

# Conductance Switching in Functionalized Carbon Nanotubes *via* Reversible Sidewall Bond Cleavage

### 5.1 Electrical conductivities in functionalized carbon nanotubes

Single-walled carbon nanotubes (SWNTs) have been investigated for manifold applications owing to their special structural, mechanical and electronic properties [60]. Chemical functionalizations of carbon nanotubes can add to their versatility serving different purposes in chemical sensing, modify the surface properties and solubilities, and facilitate the assembly, separation and purification of CNTs [61, 62, 63]. Covalent chemical functionalizations [64, 65] are especially relevant to manipulating the electronic properties of CNTs in nanoscale electric devices, such as molecular diodes or single molecular transistors.

In metallic CNTs, covalent functionalization of the sidewalls often reduces the elec-

trical conductance by orders of magnitude due to the  $sp^3$  hybridization brought upon functionalization between CNT sidewall atoms and the addends that interrupts the  $\pi$  conjugation network of CNTs. This has been verified by first-principles calculations [66, 67] as well as optical absorption spectra and electrical transport measurements [68, 69, 70, 71]. In contrast, unlike the common [2+2] or [4+2] Diels-Alder reactions where the sidewall bonds remain intact, in [1+2] cycloaddition functionalizations on armchair CNTs first-principles calculations have shown that the strain of the cyclopropane ring introduced by divalent addends such as carbenes or nitrenes leads to sidewall bond cleavage, recovering  $sp^2$  hybridization and thus preserving conductance [72, 67]. While the experimental work confirming the effect of dichlorocarbene functionalization is currently in progress, it has already been observed that the formation of an ether like oxygen bridge on the CNT sidewall in redox cycling gives high conductance due to  $sp^2$  conjugation, in contrast to the low conductance observed in other functionalities [73].

In all of these studies, it appears that a molecular switch with the capability of controlling CNT conductance in response to an external optical, chemical or electrical stimulus is highly desirable, and could have applications for molecular devices, chemical sensors, and imaging. Recent theoretical studies have revealed the possibility of tuning bond-cleavage chemistry of [1+2] cycloadditions on CNTs through the orientation of the unsaturated  $\pi$  bonds of the addend with respect to the CNT surface [74]. In our previous study on the model system of dinitrocarbene-functionalized CNTs, we found that the bond-closed configuration is greatly stabilized when the plane of the addend  $\pi$  system bisects the base of the cyclopropane ring moiety. This stabilization effect was originally attributed to the enhanced interaction between the addend  $\pi$  and the cyclopropane Walsh orbitals, which weakens the anti-bonding interaction of the sidewall bond [75]. The bridgehead carbon atoms can reversibly rehybridize from  $sp^2$  to  $sp^3$  in response to addend  $\pi$  orientation, implying a switch-like behavior. Nevertheless, for dinitrocarbene-functionalized CNTs the bond-closed configuration is unstable. The addend prefers to rotate out of cyclopropane conjugation, resulting

in only one stable open configuration that is impossible to manipulate. An isoelectronic carboxyl group was suggested to control bond-cleavage by the intramolecular hydrogen bond [74], but the hydrogen bond strength is too weak to offer bistability. The closed-bond configuration is a saddle point rather than a local minimum.

In this chapter, we systematically explore the cycloaddition functionalizations on carbon nanotubes using first-principles calculations. We characterize the structure and the electronic structure of armchair CNTs with various addends and provide an in-depth analysis of the underlying mechanisms that determine reversible bond-cleavage chemistry. We find that the high strain energy in the cyclopropane moiety can be compensated by a through-space  $\pi$  orbital interaction between the addend and the CNT, which lowers the HOMO energy significantly in the closed-bond configurations. A bond opening or closing switch marked by large conductance change can therefore be devised by modulating the proximity between the addend  $\pi$  system and the tube surface with optical, chemical or electrochemical means. We explore strategies for reversible bond cleavage using redox or hydrolysis reactions, cis-trans isomerization or excited state proton transfer and verify the marked change in CNT conductance with the addend in either the "on" or "off" configuration by quantum transport calculations.

## **5.2 Mechanisms for closed-bond stabilization in [1+2] cycloaddition functionalization**

Previous studies [72, 74] have shown that simple carbenes or nitrenes bearing only saturated moieties give an open sidewall bond, leaving very little room to maneuver for switching purposes. In this study we focus mostly on the interaction between unsaturated addends and the CNT surface, and more specifically on the closed-bond stabilization offered by unsaturated addends in the perpendicular orientation.

When considering only the cyclopropane moiety on the functionalized armchair carbon nanotubes, the simplest rationalization for closed-bond stabilization comes from the *through-bond  $\sigma$ - $\pi$  interaction* [75] (Fig. 5-1). It withdraws electron density from the HOMO of cyclopropane to the LUMO of acetylenes, causing a decrease in the bond length of the cyclopropane base but an increase for the lateral bond lengths. The bond variation in substituted cyclopropanes, however, is typically smaller than 0.05 Å, suggesting this might be a less significant effect. On the other hand, a CNT is certainly a lot more complex than a cyclopropane. The sidewall bond-breaking chemistry of functionalized armchair carbon nanotubes is reminiscent of the valence tautomerism of 1,6-methano[10]annulene and the even more relevant methanofullerenes. During the search for improved electron-accepting organofullerenes for photovoltaic applications, it was found that the quinone-type methanofullerenes or fluorenefullerenes that contain unsaturated moieties perpendicular to the surface of the fullerenes have a less negative first reduction potential than the parent C<sub>60</sub> or other type of methanofullerenes by as much as 70 mV. The peak positions can be further tuned by electron donating or withdrawing groups attached to the addend. This phenomenon was ascribed to a *through space  $\pi$ - $\pi$  interaction*, which was called "periconjugation" [76, 77, 78]. The intramolecular electronic interaction between the  $\pi$  orbitals of quinone and nearby carbon atoms of C<sub>60</sub>, separated by a spiro carbon atom, results in more extended conjugation, which possibly improves its electron accepting ability. As shown by the X-ray crystal structure, fullerene has an essentially [5]radialene-type electronic structure, i.e. the [6,6] bonds possess more double bond character while the [5,6] bonds are more single-bond like. The fact that the isolated fluorenefullerenes were exclusively [6,6] fullerenes rather than [5,6] fulleroids also implies the existence of this stabilizing interaction. As a relevant digression here, it is worth mentioning that unlike carbon nanotubes in which the sidewall bond lengths are largely affected by the addend identity, CNT curvature and chirality, in organofullerenes it is well known that experimentally only the kinetic [5,6]-open and the thermodynamic [6,6]-closed adducts were observed in most cases, whereas [5,6]-closed and [6,6]-open counterparts are almost never found due to the unfavorable endocyclic pentagon double bond con-



jugation [79]. This might be the reason why the same rotational bond-cleavage effect of dinitrocarbene substituent does not exist in fullerenes as in CNTs [74].

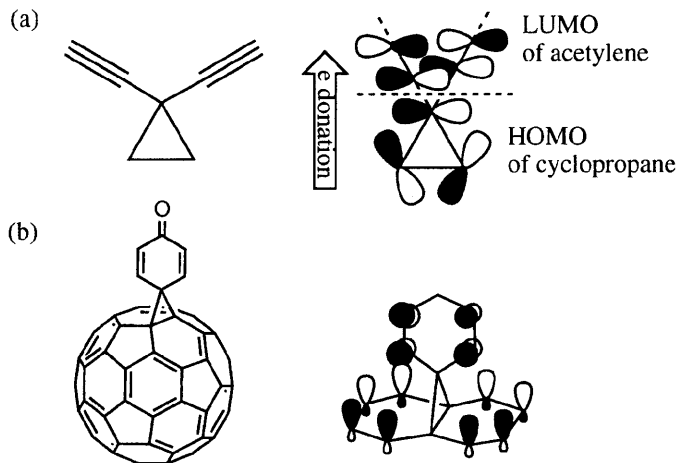


Figure 5-1: Two possible contributing effects for closed CNT sidewall bond stabilization: (a) through bond  $\sigma$ - $\pi$  interaction in cyclopropane and (b) through space  $\pi$ - $\pi$  periconjugation in quinone-type methanofullerene

### 5.2.1 Unsaturated addend orientation effect

In order to study the effect of addend  $\pi$  system orientation, we use 1,6-derivatized naphthalene (1,6-methano-[10]annulene, **1**) and pyrene (8,16-methano[2.2]metacyclophane-1,9-diene, **2**) as molecular homologues of a functionalized CNT to investigate behaviors of different addends [72]. The distance between the two bridgehead atoms 1 and 6 of **1**,  $d_{16}$ , is largely dictated by the substitutional group  $X$  [80]. The valence tautomerisation between **1** (**2**) and bisnorcaradiene (cyclopropa[e]pyrene) corresponds to the open and closed configurations of a functionalized armchair CNT. A short  $d_{16}$  around 1.6 Å would correspond to a closed sidewall bond, and an elongated  $d_{16}$  over 2 Å would correspond to a broken sidewall C-C bond in a [1+2] cycloaddition functionalized CNT. Prior to introducing more complicated effects such as the curvature of CNTs, we first study on these molecules the potential energy surface (PES) along  $d_{16}$  with different substitutional groups, in which the  $d_{16}$  is fixed at each point along

the 1D-PES and all other degrees of freedom are fully relaxed unless further specified.

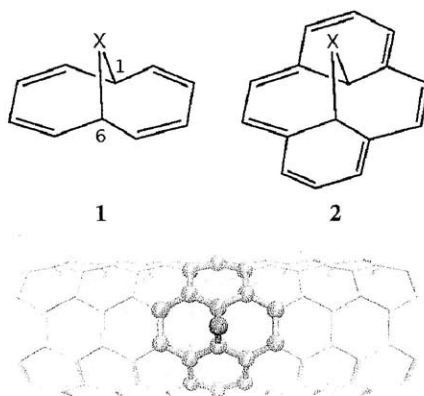


Figure 5-2: The molecular homologues of a functionalized CNT: 1,6-derivatized naphthalene (**1**) and pyrene (**2**). The bond length between the bridgehead carbon atoms  $d_{16}$  depends primarily on the identity of the addend  $X$ . The similarity between the local structure of a [1+2] cycloaddition functionalized CNT and the **2** is also shown.

First of all, to rule out the orientation effect of unsaturated substitutional groups, we look at **2** with  $X=C(CHO)_2$  (abbreviated as pyrene- $C(CHO)_2$  in the following) with the  $C=O$  double bonds pointing at different directions as shown in Fig. 5-3. As reported in previous studies, the addend prefers the unconstrained "flat"  $\pi$  plane as the most stable conformation in which the sidewall bond  $d_{16}$  is open, and in the constrained perpendicular  $\pi$  plane conformation, the  $d_{16}$  bond between two bridgehead atoms prefers closed. Between the two constrained perpendicular  $\pi$  plane conformations, however, we find that the closed bond configuration can be stabilized by about 0.2 eV more in the "O side" orientation in which the  $C=O$  double bonds lie closer to the pyrene backbone than in the "O top" orientation. This is a strong suggestion that the major closed-bond stabilization comes from periconjugation. The closed bond is stabilized the most when the addend  $\pi$  has maximal overlap with the pyrene backbone  $\pi$ -system. On the other hand, the through-bond cyclopropane conjugation would not have been affected by the proximity between the oxygen atom and the pyrene surface.

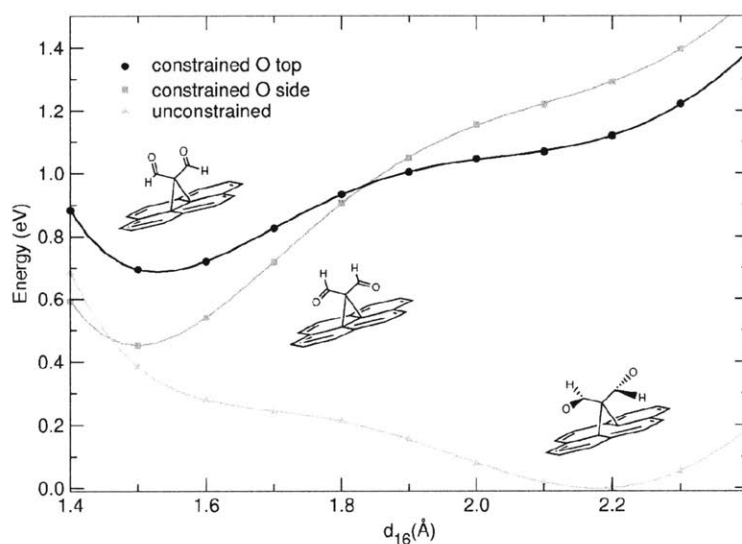


Figure 5-3: Potential energy surface as a function of  $d_{16}$  for **2** with  $X=C(CHO)_2$  in different conformations. The closed-bond configuration is stabilized more when the  $C=O$  double bonds are closer to the pyrene backbone in the constrained perpendicular "O side" orientation.

### 5.2.2 Periconjugation effect

The addend  $\pi$  bonds by nature prefer the flat orientation if they are left free to rotate, but they can be "locked" in place by a ring structure such as the cyclopentadienyl ( $C_5H_4$ ) group. To further examine the strength of the periconjugation effect, we study the potential energy profile along  $d_{16}$  of **1** and **2** with various saturated and unsaturated ring substitutional groups as shown in Fig. 5-4. Each point in Fig. 5-4 corresponds to a full relaxation with only one geometry constraint,  $d_{16}$ , and the energy minimum under this constraint would correspond to the lowest energy ground state of the system, which is also confirmed by vibrational frequency calculations.

As can be seen clearly in Fig. 5-4, for both **1** and **2**, the closed configuration is stabilized more when the addend  $\pi$  system spans longer and leans toward the aromatic plane. The stabilization strength goes in the order of  $C_5O_2H_4$ -diketone  $>$   $C_5O_2H_4$ -

dienol > C<sub>5</sub>H<sub>4</sub> diene, much greater than the saturated C<sub>5</sub>H<sub>8</sub> or CH<sub>2</sub>. For the case of **2**, the closed configuration is stabilized significantly more when X=C<sub>5</sub>O<sub>2</sub>H<sub>4</sub>-diketone than when X=C<sub>5</sub>H<sub>4</sub> by as much as 0.7 eV. This is another strong proof for the existence of the periconjugation effect as these substitutional groups are highly similar in structural motif and electronegativities. Any kind of inductive effect, if it exists, shall only differ slightly and shall not cause such a dramatic stabilization.

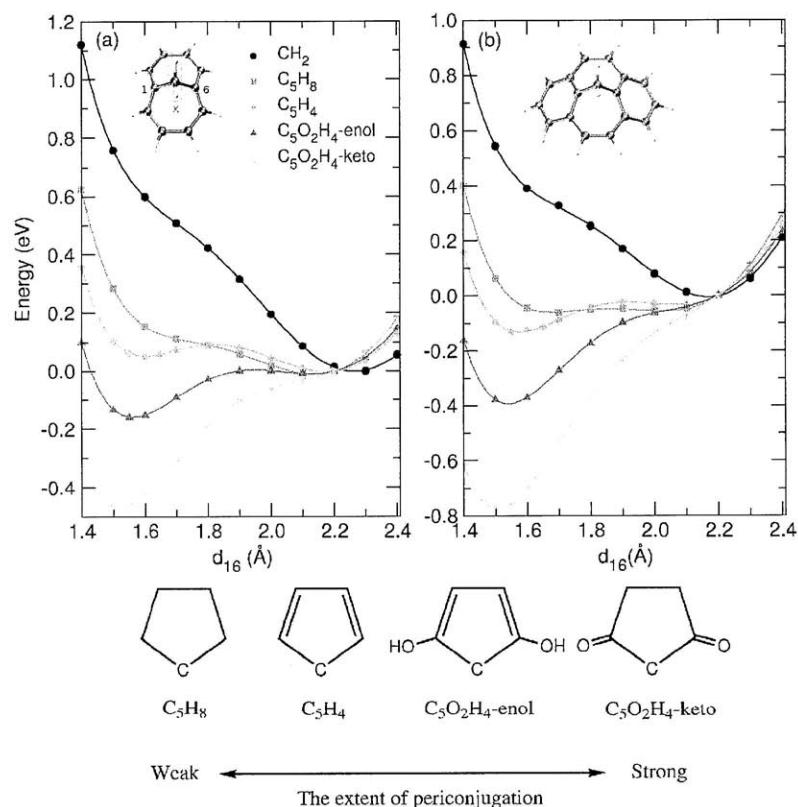


Figure 5-4: Potential energy surface as a function of  $d_{16}$  for (a) **1** (b) **2** functionalized with ring substituents. The zeros are set at  $d_{16}=2.20$  Å to mark the release of roughly same strain energy.

The origin of periconjugation stabilization can be revealed by an analysis of the eigen orbital evolution along  $d_{16}$ . The Walsh diagram of 1,6-methano[10]annulene (**1**) with X=CH<sub>2</sub> and X=C<sub>5</sub>O<sub>2</sub>H<sub>4</sub>-keto are presented in Fig. 5-5. The occupied  $a_2$  and unoccupied  $b_1$  are relatively unaffected by the  $d_{16}$  bond length and remain roughly flat.

The two  $b_2$  orbitals involve the antibonding interaction along  $d_{16}$  and are lowered in energy as the bond length increases. On the contrary, the two  $a_1$  orbitals involve the bonding interaction and are raised in energy with increasing bond opening. The most striking difference between  $X=CH_2$  and  $X=C_5O_2H_4$ -keto is the significant lowering in energy of  $b_2$  in  $X=C_5O_2H_4$ -keto. The occupied  $b_2$  orbital shows electron density delocalization between the  $\pi$  of naphthalene backbone and C=O double bonds and even switched ordering with  $a_2$ . This gives the overall stabilization of  $X=C_5O_2H_4$ -keto in closed configuration.

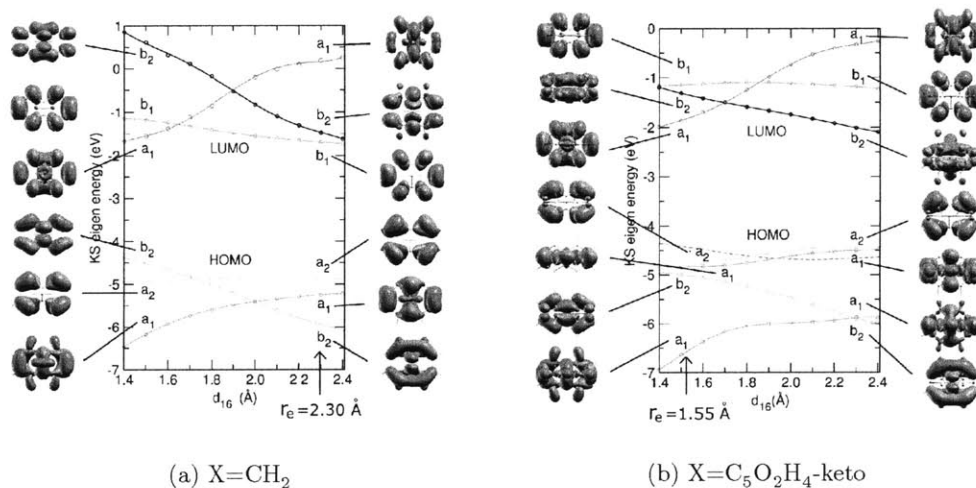


Figure 5-5: Walsh diagram along  $d_{16}$  of **1** for systems (a) without and (b) with periconjugation. The equilibrium bond lengths are also marked. The dashed curve in (b) is an orbital in the same energy window but with the density mostly located on the substituent and should be safely left out of discussion.

To this point, periconjugation is only expected to exist in perpendicular unsaturated addends. In our search among saturated addends, however, we find that for both **1** and **2**,  $X=C_5H_8$  is also more stabilized in the closed configuration than  $X=CH_2$  is. This might be caused by the difference in the relative rotational orientation of the C-H bonds adjacent to the spiro carbon atom with respect to the cyclopropane moiety. To verify this, we look at simpler substituents such as dimethylcarbene. We note that the rotation of the methyl groups also introduces a slight periconjugation

effect. The methyl groups can exist in two conformations, staggered or eclipsed with respect to the cyclopropane lateral bonds (Fig. 5-6); both conformations predict an open sidewall bond with a shallow potential energy surface. The staggered methyl groups, as expected, give a more stable structure by 0.2 eV than the eclipsed ones do, but the energy barrier for the  $d_{16}$  bond to close in the eclipsed methyl conformation (0.12 eV) is only one half of that of the staggered methyl conformation (0.19 eV). Fig. 5-6 also shows the HOMO and HOMO-1 for both structures at  $d_{16} = 1.6 \text{ \AA}$ . The staggered molecule follows the same orbital ordering as in  $X=\text{CH}_2$  and gives an  $a_2$  HOMO and a  $b_2$  HOMO-1, while in the eclipsed molecule, the two C-H  $\sigma$  bonds sticking towards the naphthalene backbone on both sides of the top C atom stabilize the  $b_2$  orbital, showing a similar, although to a minor extent, through space orbital interaction mechanism as in the case of perpendicular unsaturated substituents.

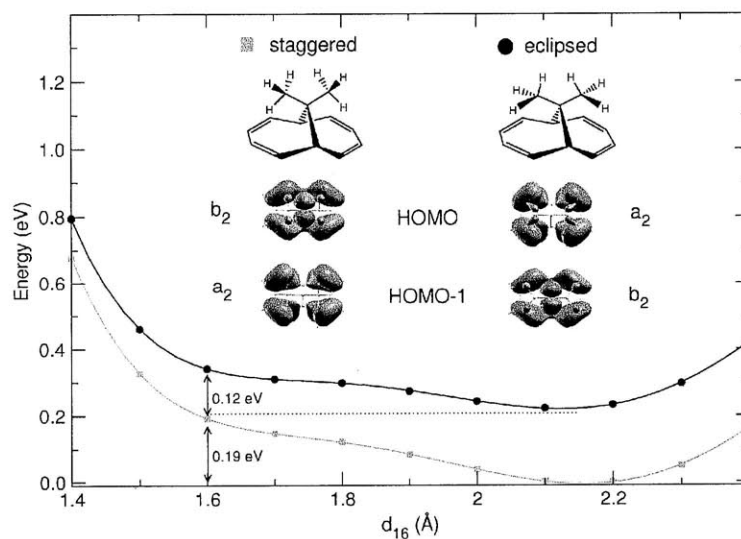


Figure 5-6: (a) Potential energy surface as a function of  $d_{16}$  for **1** with  $X=\text{C}(\text{CH}_3)_2$  in staggered and eclipsed conformations. The frontier orbitals of two conformers at  $d_{16} = 1.6 \text{ \AA}$  are also shown here.

### 5.2.3 CNT curvature effect and the bent-graphene model

The tautomerization between the bond-open and bond-closed form depends largely on the chirality and curvature of the CNT. In the case of zigzag and armchair CNTs, two types of C-C bonds exist: the "axial" bonds  $A$  (the C-C bonds that are more "parallel" to the tube axis) and the "orthogonal" bonds  $O$  (the C-C bonds that lie more "perpendicular" to the tube axis). For both types of tubes, computational studies have shown that the  $A$  bond forms a closed-bond three-membered ring upon carbene cycloaddition and the  $O$  bond undergoes a sidewall bond opening upon carbene insertion [72, 81]. The reaction energy defined as  $\Delta E = E_{CNT-func} - E_{CNT} - E_{func}$  increases linearly as the curvature increases for both modes of addition reactions, but the functionalized CNT is always more stable in the open  $O$  bond configuration than in the closed  $A$  bond configuration since the former involves a release of strain. Here we focus our discussion only on armchair CNTs, and on the [1+2] cycloaddition reactions to the orthogonal sidewall bond, which opens up in most cases upon cycloaddition reaction but may be brought back to the closed configuration in the presence of special closed-bond stabilizing effect. The orthogonal bonds in zigzag or chiral tubes should have similar behavior but also depends specifically on the angle of each C-C bond with respect to tube axis.

As mentioned above, for the orthogonal bonds in armchair CNTs, the open bond configuration is favored in high curvature CNTs so as to release the strain, but as the tube grows larger and the curvature decreases, the closed bond configuration is gradually lowered in energy and eventually becomes more stable (for tubes larger than an (18,18)-CNT [72]). For small tubes, however, the competition between periconjugation and the curvature effect determines the equilibrium between a closed and an open sidewall bond. We investigate a similar set of unsaturated substituents as in Fig. 5-4 on a bent graphene model to represent the real CNT curvature effect. The carbon backbone of the 12-angstrom wide bent graphene nanoribbons is taken from CNTs with different curvatures, with the edge hydrogenated. The curvatures of the

bent graphene nanoribbons are preserved by freezing the edge carbon atoms during later geometry optimizations. The bent-graphene model is used to study the effect of CNT curvature in a systematic and efficient way. The carbon backbone of the bent graphenes is taken from CNTs with different curvature, with the graphene edge hydrogenated. The edge carbon atoms of the graphene nanoribbon are frozen in later geometry optimizations with the addends to keep the curvature. The bent graphene derivatives are found to represent excellently the full carbon nanotubes functionalized with  $\text{CH}_2$  (Fig. 5-7) with the energy difference within 0.1 eV. In cases involving unsaturated addends such as  $\text{C}(\text{CN})_2$ , the bent graphene model shows stronger closed-bond stabilization, which can be rationalized by the fact that the narrow graphene fragments are richer in  $\pi$  electrons and would induce stronger periconjugation effect. In any case, the difference between the bent graphene model and a true CNT is within 0.2 eV in the bond-closed configurations, but extra care needs to be taken in predicting the behavior of a functionalized CNT when the bond-open and bond-closed configurations are close in energy tested on a bent graphene model.

Fig. 5-8 shows the relaxed sidewall bond length of different bent graphene derivatives as a function of curvature. For unconstrained  $\text{X}=\text{C}(\text{CHO})_2$ , the sidewall bond is always open up to the "(12,12)" bent graphene, while for  $\text{X}=\text{C}_5\text{O}_2\text{H}_4$ -keto which exhibits the strongest periconjugation effect, the sidewall bond is always closed even for the smallest (5,5) bent graphene (It should be noted here that for this particular substituent, the open and closed configurations are very close in energy for "(5,5)" bent graphene, in real (5,5) CNT  $\text{C}_5\text{O}_2\text{H}_4$ -keto actually gives an open configuration). Other addends showing intermediate periconjugation show transitions from open to closed at different critical curvatures.

Any single substituent among these on a carbon nanotube will be useless for switching purposes since it only gives one configuration rather than a bistable ground state. Instead, the substituents studied in Fig. 5-8 should be seen as basic molecular modules that can be chemically transformed between each other. For example,



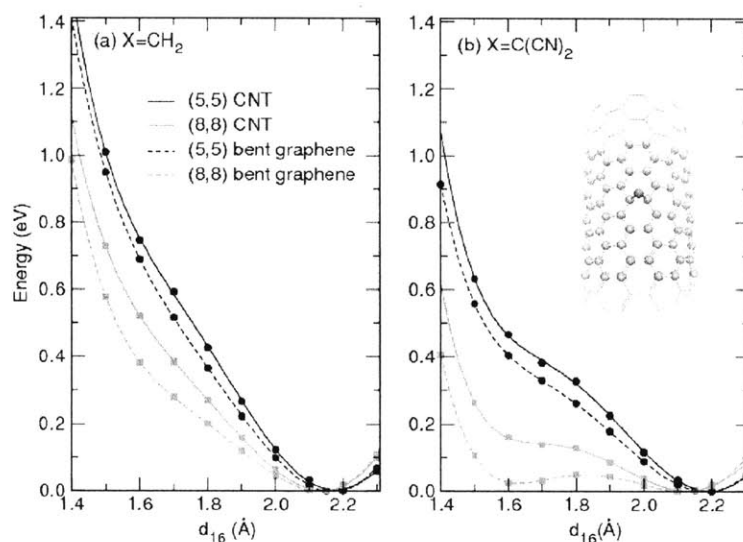


Figure 5-7: Potential energy surface as a function of sidewall bond length  $d_{16}$  for CNT and bent-graphene with (a)  $X=\text{CH}_2$  and (b)  $X=\text{C}(\text{CN})_2$ . The carbon backbone of the bent graphene nanoribbon is taken from CNTs with different curvatures. The edge carbon atoms (hydrogenated carbons) are kept fixed in later relaxations to preserve the curvature.

the cyclopentadienyl-functionalized (8,8) CNT, in principle, can be hydrogenated (if manipulated properly so that only the  $\pi$  bonds on the addend react) to give rise to the cyclopentane  $\text{C}_5\text{H}_8$  substituent accompanied by a nanotube sidewall bond opening. Similarly, the cyclopentadiene ring can be cleaved to give some structure like  $X=\text{C}(\text{CHO})_2$ , and a functionalized (10,10) or (12,12) tube shall respond with a conductance change. Indeed, two of the substituents in Fig. 5-8,  $\text{C}_5\text{O}_2\text{H}_4$ -enol and  $\text{C}_5\text{O}_2\text{H}_4$ -keto, are already tautomers to each other and could perfectly serve as a switch for a (6,6) tube if one is able to stabilize selectively either enol or keto form in different chemical environments. Overall, the tubes with diameters around 0.8 to 1.4 nm have more flexible bond lengths and can be functionalized as conductance switches based on vertical transitions between different curves in Fig. 5-8.

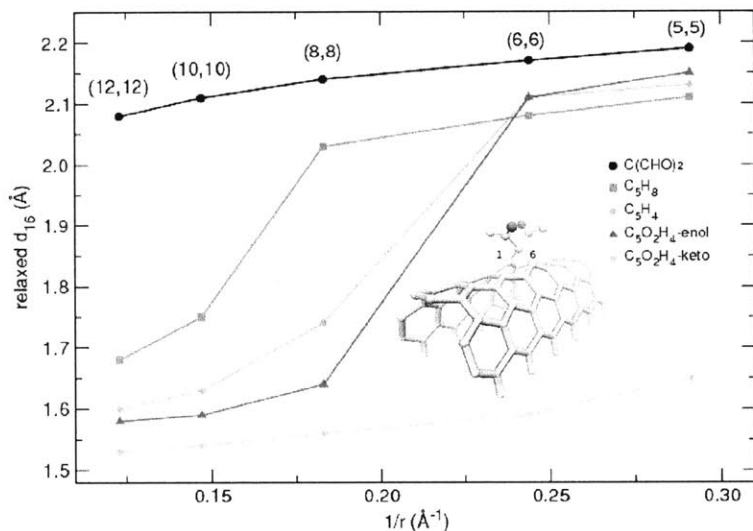


Figure 5-8: Sidewall equilibrium bond distance  $C_1$ - $C_6$  ( $d_{16}$ ) for bent graphenes representing (n,n) CNTs

When a functionalized tube is switched from the open to the closed bond configuration, another complication that may arise is the relative stability between a closed axial bond  $A$  and a closed orthogonal bond  $O$ , and the possibility for the substituent group to "migrate" to an adjacent C-C axial bond. For a carbene functionalized (5,5) tube, the fully relaxed open  $O$  configuration is 1.2 eV more stable than the closed  $A$  configuration, but even the constrained closed  $O$  bond is still more stable than the closed  $A$  bond configuration by about 0.5 eV [82]. In the presence of periconjugation, the situation can be slightly more complicated since the distance between the addend  $\pi$  system and the tube surface is different when the addend is attached to an  $A$  bond or an  $O$  bond. For a functionalized tube prepared as the "open"  $O$  bond (which is absolutely thermodynamically favored) then transformed to the "closed"  $O$  bond configuration chemically (to be discussed in the following section), we presume that as long as the chemical transformations on the addend part do not involve any biradicaloid mechanism, the addend is likely to remain on the same attachment site

(i.e. the *O* bond) and is unlikely to "walk" to an adjacent *A* bond. In any case, for conduction switching purposes, both a closed *O* and a closed *A* bond will give low conductivities since they both disrupt severely the  $\pi$  manifold of the CNT.

## 5.3 Conduction Switching on Functionalized Carbon Nanotubes

Apart from the keto-enol tautomerization mentioned in the last section, here we propose several other switching mechanisms that could suit different experimental conditions and device setups. These switches can be controlled by chemical reactions or optical excitations. Fig. 5-9 gives an overview for the switching mechanisms we propose. The switching can be achieved by breaking a bond in the 5-membered ring, e.g. in a hydrolysis reaction of an ester or an amide bond (Fig. 5-9(a)), or by removal of the C=O double bonds, e.g. by reducing the diketone to a diol (Fig. 5-9(b)). Alternatively, the switching can also take place by tuning the spatial proximity between the addend  $\pi$  system and the tube surface, e.g. by imine cis-trans isomerization (Fig. 5-9(c)), or by shifting the conjugation on the addend (keto-enol transformation) in excited-state proton transfer (ESPT) (Fig. 5-9(d)). For all the systems considered in the following, we consider the addition reaction to the orthogonal sidewall bond of the armchair (6,6) CNT, and perform in each case full structural relaxations in a supercell containing 5 primitive unite cells (i.e. 120 CNT carbon atoms).

### 5.3.1 Switching *via* chemical reactions

As shown in Fig. 5-10, hydrolysis and redox reaction products successfully give stable open and closed configurations, as expected. The CNT sidewall bond is closed with the lactone or diketone substituent, and is open with free carboxyl groups or diol addends. Based on our study of the curvature effect using the bent pyrene model (Fig.

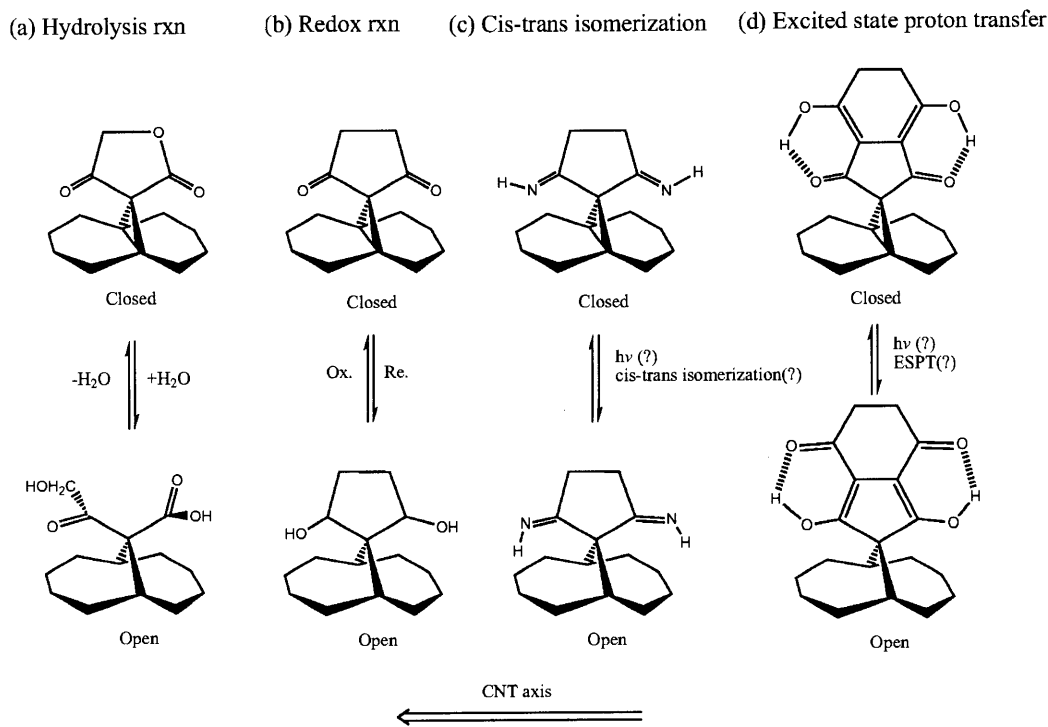


Figure 5-9: Proposed conductance switching mechanism in functionalized armchair CNTs. The addends are attached to the C-C bonds perpendicular to the CNT axis labeled on the bottom of the figure.

5-8), we predict that the hydrolysis switch should be able to work for tubes ranging from (6,6) to (12,12), and the redox switch should work for tubes from (6,6) to at least (8,8) or even (10,10). From a synthetic point of view, attaching such functional groups to a CNT sidewall should be feasible. For example, to prepare a hydrolysis switch, a malonate moiety can be introduced relatively easily by the well established Bingel reaction [83, 68]. Experimentally, the reaction process in a solution will possibly require extra care to avoid unwanted damage to the tube surface under redox or acid/base conditions.

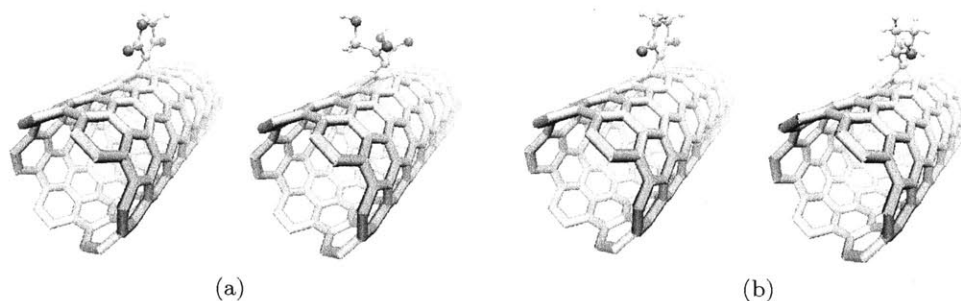


Figure 5-10: Relaxed structures of a functionalized (6,6) CNT with (a) lactone and free carboxyl groups shown in Fig. 5-9(a) and (b) diketone and diol addends shown in Fig. 5-9(b). The CNT sidewall bond is closed with the lactone or diketone substituent, and is open with free carboxyl groups or diol addends.

### 5.3.2 Switching *via* optical excitations

An optically controlled switch, in contrast, is less straightforward to design since the bond-breaking or conjugation-shifting in response to optical stimulation is more demanding on the overall molecular electronic structure. We propose tentatively the imine cis-trans isomerization and the excited state proton transfer (ESPT) as optically controlled conductance switches. In the imine cis-trans isomerization, the open-closed sidewall bond transformation is determined by the conformation of the N-H bond. This happens since the strength of periconjugation is highly sensitive to the spatial proximity between the addend double bonds and the tube surface. It is known that in the fullerene counterpart, when two benzene rings are fused to the quinone moiety in the quinone-type methanofullerenes, the first reduction potential becomes more negative rather than more positive, *i.e.* it becomes an even worse electron acceptor. This was accounted by the steric hindrance effect between the "peri" hydrogens and the surface of  $C_{60}$  [78]. We study the ground state potential energy surface of bent graphenes with X=cis or trans cyclic imines (we arbitrarily differentiate the two conformers as cis (when the peri-hydrogens point toward the tube surface) or trans (when the peri-hydrogens point away from the tube surface) isomers, see Fig. 5-11) and found that at a critical curvature (in this case the bent graphene representing (6,6) CNT), a change as simple as a cis-trans isomerization

would indeed induce a sidewall bond-cleavage, while tubes smaller or larger than this critical size will have only closed or only open configurations for both isomers. In practice, however, the imine cis-trans isomerization will be difficult, if not impossible, to manage. Unlike the well known light-initiated cis-trans isomerization of azobenzenes or stilbenes, photoinduced rotation along the C=N (or C=C, N=N) double bonds for simple imines (or ethylene and diimide) so far has not been observed experimentally due to technical difficulties (the excitation energy needs to be extremely high; around 100-200 nm far-UV light). But numerous theoretical investigations have proven that photoisomerization is likely to happen through a conical intersection between the ground and the first excited state at the femtosecond time scale [84, 85, 86].

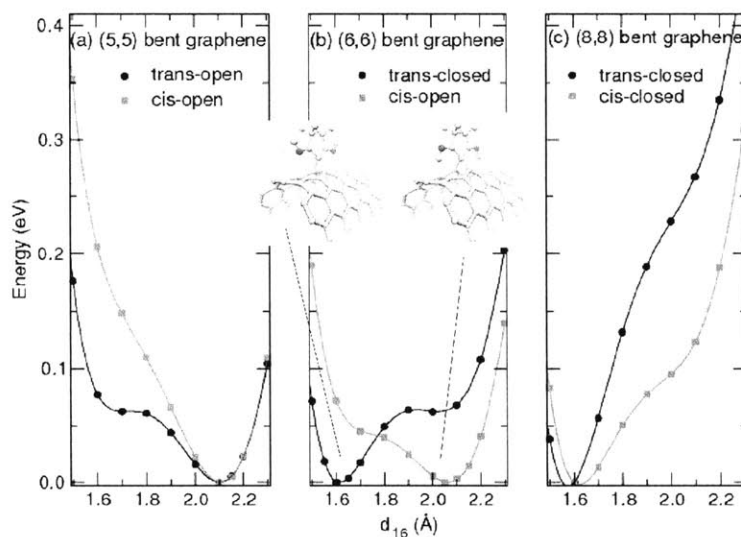


Figure 5-11: Potential energy surface as a function of  $d_{16}$  for (5,5)-, (6,6)-, or (8,8) bent graphenes functionalized with X=cis- or trans-cyclopentadiimine. The relaxed structure of functionalized (6,6) bent graphene in the equilibrium bond length are also shown.

For ESPT (shown in Fig.Fig. 5-9(d)), we are able to locate two local minima for the normal(the cyclopentadiketone) and the proton-transferred tautomer(the

cyclopentadiene-diol) for the hydrogenated substituents alone (not attached to the CNT). The forward and reverse reaction barriers in the ground state for this proton transfer reaction are 0.50 eV and 0.28 eV, respectively. Nevertheless, when these addends are attached to the CNT, both normal and tautomer substituents give an open sidewall bond for a (6,6) tube and both give a closed sidewall bond for a (7,7) tube. This again demonstrates the "spatial sensitivity" of periconjugation. When the C=O double bonds of the cyclopentadione are attracted towards the hydroxyl groups, the distance between the C=O double bonds and CNT surface increases slightly, the periconjugation decreases, and the sidewall bond opens.

### 5.3.3 Switching *via* quinone-quinol transformation

Alternatively, an intramolecular hydrogen bond can be tuned to control the distance between the C=O double bond and the tube surface. As shown in Fig. 5-12, the hydrogen bonded cyclopentadione and the quinol moiety shall render the sidewall bond of a (6,6) tube open, but the intramolecular hydrogen bonding can be easily removed by either an oxidation or an acid/base reaction. The diketone C=O double bonds are therefore released and the (6,6) CNT sidewall bond will be closed. The oxidation of a quinol into a quinone can happen in a milder condition than the diol oxidation, which should be less harmful to the CNT itself and more favorable in this respect.

## 5.4 Quantum conductance of functionalized CNTs

### 5.4.1 Singly functionalized CNTs

The conductivity of the proposed switches in the on and off states on CNTs are also investigated. Fig. 5-13 shows the quantum conductance of a singly functionalized (6,6) carbon nanotube with either lactone/acid or the diketone/diol addend pairs designed in Fig. 5-9 (a) and (b). While the conductances for the "open" configurations

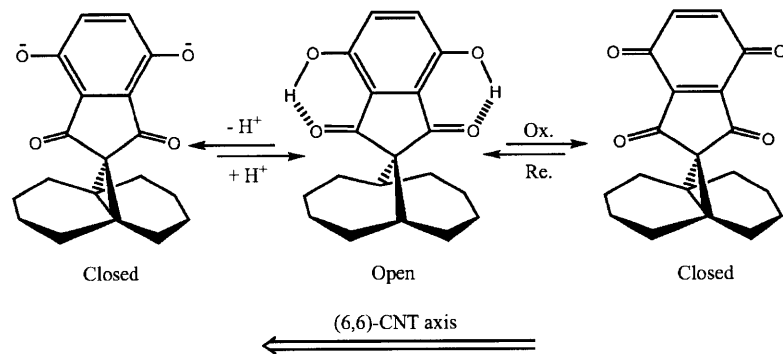


Figure 5-12: Proposed conductance switching mechanism by tuning the intramolecular hydrogen bonding between the quinol and the cyclopentadione moiety. On a (6,6) CNT, the hydrogen bonded addend (in the middle) shall render the CNT sidewall bond open, while removal of the hydrogen bonds will induce a bond closure.

(the acid and the diol) are negligibly affected and can hardly be distinguished from the pristine conductance around the Fermi level, the conductances of the "closed" configurations (the lactone and the diketone) are lower. Nevertheless, the conductances at the Fermi level for both cases remain close.

#### 5.4.2 Multiply functionalized CNTs

The quantum conductance for large scale randomly functionalized carbon nanotubes is also computed to simulate real experimental conditions. The quantum conductance is taken as an average from 20 different configurations with functional groups randomly (both translationally and rotationally) attached to a nanotube. Fig. 5-14 is an illustration of one of the 20 constructed configurations with 5 addends. The Hamiltonian matrix of the central region ( $H_C$ ) of the multiply functionalized CNT is constructed by assembling  $H_{C_i}$ 's of individual singly functionalized CNT segments, taking into account all possible rotated equivalent positions and random lengths of pristine CNT segments inserted in between. The multiply functionalized carbon nanotubes computed has an average addend density of about 1 addend for every 200 carbon atoms, comparable to the experimental density in typical [1+2] cycloaddition



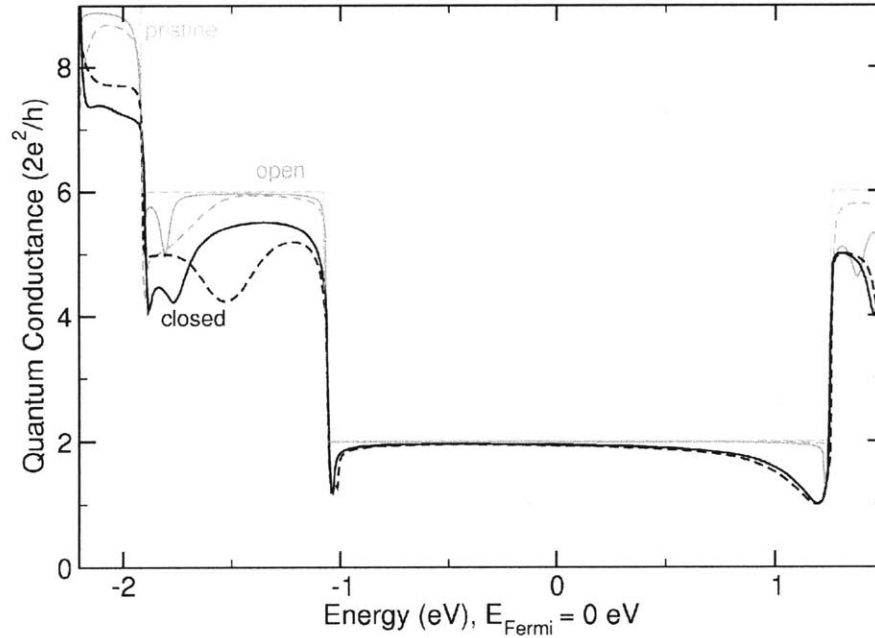


Figure 5-13: Quantum conductance of an infinitely long (6,6) carbon nanotube with a single functionalization. The solid lines correspond to the lactone/acid addend pair and the dashed lines correspond to the diketone/diol addend pair. The red color are for the "open" (acid and diol) and the black color are for the "closed" (lactone and diketone) conformations. The quantum conductance of the pristine tube is also given in the brown dashed line as a reference. The quantum conductance depends more on the "open" or "closed" conformations rather than on the specific addend identity in a wide energy range around the Fermi energy.

functionalizations. This addend density ensures no loss in transferability of each individual singly functionalized  $H_{C_i}$  matrix, and should be seen as an upper bound for the conductivity measured experimentally in more densely functionalized CNTs.

The difference is greatly magnified in multiply functionalized CNTs. Fig. 5-15 shows the quantum conductance of a 22 nm, 47 nm or 67 nm-long (6,6) CNT functionalized with 10, 20, or 30 addends, respectively, for the diketone/diol switch pair. The strong scattering of the  $\pi$  electrons in a window of about 2 eV around the Fermi energy in the "closed" conformation is evidenced by the increasing drop in quantum conductance with the degree of functionalization. The quantum conductance is reduced by about 13% from 1 to 10 addends, another 23% from 10 to 20 and at last

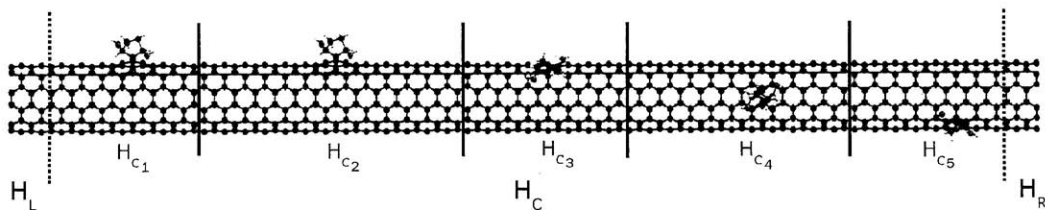


Figure 5-14: Illustration of the methodology used to construct Hamiltonian matrices for large disordered functionalized carbon nanotubes. Shown here is a carbon nanotube functionalized with 5 groups. The computed quantum conductance is an average from 20 different configurations.

another 29% from 20 to 30 addends in the "closed" (diketone) case. On the contrary, the "open" (diol) case shows only a 2% reduction from 1 to 10 addends, another 3% from 10 to 20, and another 3% from 20 to 30 addends. The average quantum conductance at the Fermi level functionalized with 30 addends in "closed" conformation drops to about 0.87 whereas it remains at about 1.84 in the "open" case. The fundamental origin of this strikingly different behavior goes back to the earliest prediction: the sidewall bond breakage in the "open" configuration preserves the  $\pi$  network, while in the "closed" conformation only a  $\sigma$ -like Wannier function is left, destroying locally the  $\pi$  conjugation, as shown in Fig. 5-16.

In summary, we have identified the role of through-space periconjugation in controlling the sidewall bond-cleavage chemistry in [1+2] cycloaddition functionalized CNTs. We have predicted that a functional group similar to the  $C_5O_2H_4$ -ketone moiety with carefully arranged  $\pi$  orientations with respect to the CNTs could strongly stabilize the closed conformation even for CNTs with the curvature as high as that of a (6,6) tube. We have proposed possible conduction switching mechanisms that cover different CNT diameters and can be applied in different experimental environments and device setups, controlled by chemical, electrochemical or optical means. Our transport calculation verifies that the quantum conductance changes significantly in the on or off state. These switches, if realized experimentally, should have practical applications in nanoscale electrical devices and sensing.

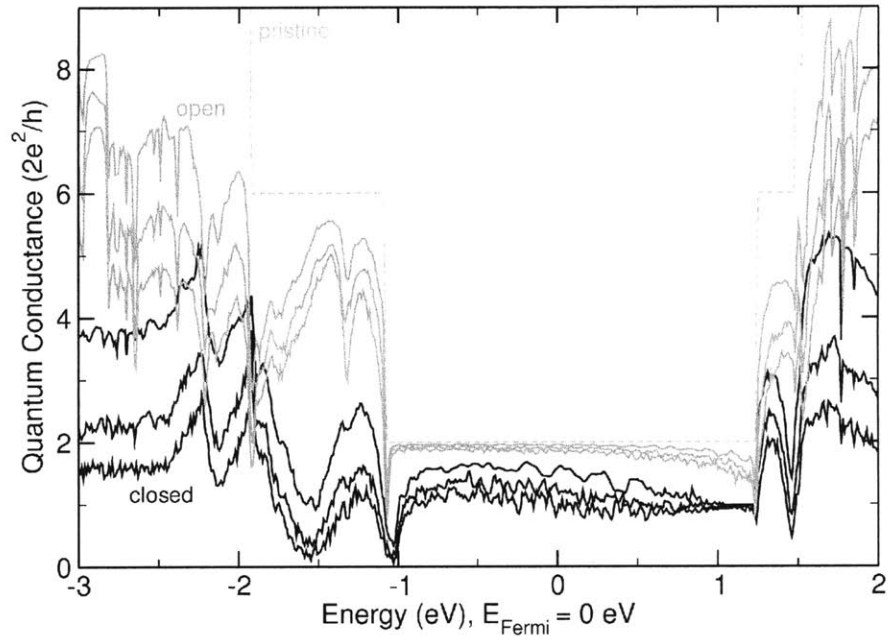


Figure 5-15: Average quantum conductance (in units of  $2e^2/h$ ) of 20 randomly functionalized (6,6) carbon nanotubes with 10, 20 or 30 addends. Both types of addends are considered (ketone in black and diol in red). Inside a given set of conductance curves (black or red), the highest curve represents 10 addends and the lowest curve represents 30 addends. The quantum conductance of a pristine (6,6) carbon nanotube is given in dashed line as a reference.

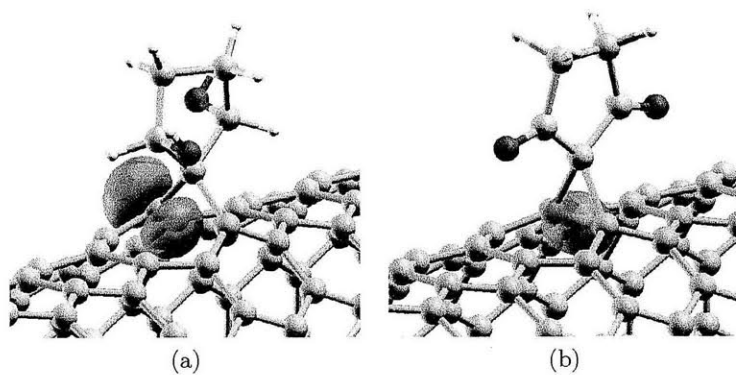


Figure 5-16: Visualization of (a) the “ $p_z$ ”-like Wannier orbitals in the “open” conformation and (b) the “ $\sigma$ ”-like orbital in the “closed” conformation in the diketone/diol addend pair. The strong scattering introduced in the “closed” conformation is caused by the disappearance of the two  $p_z$  Wannier orbitals, which disrupts the  $\pi$  manifold of the CNT.

## Chapter 6

# Improved Intertube Electrical Conductivity of Carbon Nanotube Networks Cross-Linked by Transition Metals

### 6.1 Electrical conductivities in CNT networks

While the assembly and connection of individual SWNTs to metal contacts remain a challenge and impede practical applications, carbon nanotube thin films can be readily fabricated and show reproducible characteristics [87]. As a result, there has been increasing enthusiasm for using single-walled carbon nanotube (SWNT) networks as transparent conductive thin films in various electrochemical applications, ranging from electrodes for solar cells, organic light emitting diodes, to transparent transistors [88, 89, 90]. A wide range of conductivities, from 12.5 S/cm [91] to 6600 S/cm [92] have been reported for SWNT films, but regardless of fabrication methods and SWNT types used, all experimental values are orders of magnitude lower than single SWNT fibers (axial conductivity  $\sim 10000$  to  $90000$  S/cm) owing to poor electronic tunneling at intertube junctions [92, 93]. A typical fabrication

process of SWNT thin films involves blending the nanotubes into a matrix polymer for good dispersion and suspension, which causes severe limitations in nanotube-to-nanotube carrier hopping. Chemical functionalizations with conductive polymers are commonly employed to improve conductivity as well as to make mechanically stronger nanocomposites. Nevertheless, most functionalized SWNT networks show further reduced electrical conductivity by 2 to 3 orders of magnitude due to interruption of  $\pi$ -conjugation, charge trapping, or steric hinderance of bulky functional groups [92]. In the few reported examples where the conductivity of a polymer-nanotube composite does improve, the results are controversial and depend strongly on morphology and fabrication methods [94]. While it was suspected that the conductivity was dominated by the conductive polymer alone, rather than of nanotubes [95]; neither the cooperative nature between the CNTs and the polymer linkers nor the mechanism of electron tunneling through a linker at intertube junctions has ever been addressed in detail. Therefore, the optimization of SWNT networks and a detailed understanding of their electronic properties shall offer considerable scope for the development of SWNT-based electronics.

Many first-principles studies have focused on assembling molecular electronic devices by attaching single molecules between two SWNT ends [10, 55], but few have explored the possibility of sidewall functionalizations as an alternative way to cross-link SWNTs. It has been shown that a near-transparent nanotube-molecule-nanotube junction is possible through careful arrangement of the molecular orientation and linkage sites with respect to the tube terminals [96, 97, 98, 56], but the conductivity would depend strongly on the linker identity, linkage site, molecular conformation and SWNT chirality. As a result of high experimental uncertainties and difficulties in manipulating the SWNT-molecule-SWNT junctions on the atomic scale, the observed electric conductance remains poor in most experiments [99, 10, 55, 3]. On the other hand, sidewall-functionalizations were rarely considered as a possibility to enhance intertube coupling. This can be attributed to the following two reasons: First of all, most sidewall functionalizations inevitably lead to unfavorable disrupt-

tion of the intrinsic nanotube  $sp^2$  conjugation. Second, the  $\sigma$  bonds of the sidewall functional groups, which are perpendicular to the tube, can hardly be coupled to the  $\pi$  conjugation which runs along the SWNT surface. Nevertheless, for structures like SWNT networks, sidewall functionalizations could employ much more attachment sites and can potentially increase the intertube conductance more effectively than end-functionalizations. It would be highly desirable if a sidewall linker could be designed, without the extreme specificity required for end-functionalizations, to serve the same purpose of improving intertube conductivity.

In this study, we use first-principles calculations to address the issue of low electrical conductivity in carbon nanotube networks. We first use polyacene as a prototype model system to study the effect of sidewall linkers on intertube conductivity, and then move on to large scale nanotube calculations. We briefly discuss the nature of intertube tunneling of bare SWNT junctions and the limitation of common organic polymer linkers. We then explore the effect of transition metal adsorption on CNT surfaces, and find the strong coupling between the transition metals and the sandwiching CNTs may lead to a solution that has never been considered in this field.

## 6.2 Intertube conductivity of the polyacene model

### 6.2.1 Band structure of the polyacene model

Polyacene can be seen as the narrowest possible nanoribbon which preserves the electronic structure characteristic of a metallic armchair SWNT marked by the crossing of valence and conduction bands and a quantum conductance of 2 at the Fermi level. The entire  $p_z$  manifold of polyacene is retained in the MLWF transformation to accurately describe the band dispersion around Fermi level. Fig. 6-1 shows the Wannier Function interpolated band diagram which matches perfectly to the plane wave calculation up to 3 eV above Fermi energy. The conduction band minimum of polyacene

lies 3.14 eV above the Fermi level at the  $\Gamma$  point and exhibits near free electron character. The  $\pi^*$  bands are strongly hybridized with the  $\sigma^*$  bands and cannot be clearly distinguished, as evidenced by the PDOS projection onto all carbon  $p_z$  orbitals. The MLWF transformation, containing the full  $p_z$  manifold but not the  $p_x$  or  $p_y$ 's, cannot perfectly trace the physical first unoccupied band curve close to the  $\Gamma$  point. The quantum conductance calculated following Landauer formula with MLWF basis shows the typical step-like behavior with each step corresponding to the sharp van Hove peak of the density of states (DOS).

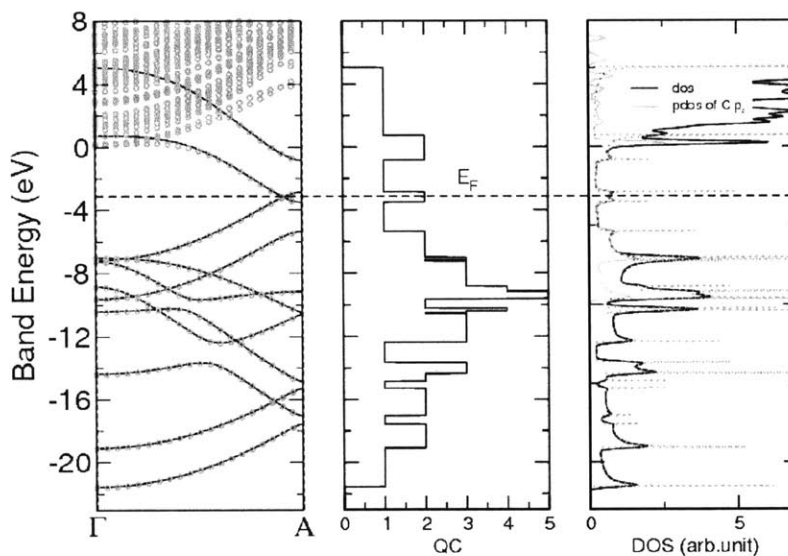


Figure 6-1: The band structure, quantum conductance, and density of states of pristine polyacene. The wannier function interpolated band structure and density of states are shown in red circles and red dashed lines, respectively. The solid curves are calculated from full plane-wave basis calculation.



### 6.2.2 Intertube tunneling without linkers

A typical van-der-Waals distance between two graphene layers in graphite or CNT tubes in SWNT mats is around 3.5 Å. The natural intertube transmission unassisted by cross-linkers is simulated by laying a short pentacene molecule on top of a broken polyacene junction with both terminals hydrogenated. When the distance between the bridging pentacene is (unphysically) brought closer than 2 Å, the substantial hybridization between the  $\pi$  orbitals of the pentacene bridge and the underlying polyacene junction preserves the majority of conductivity around Fermi level, as shown in Fig. 6-2(a). As the distance between the layers is larger than 3 Å, the interaction between the  $\pi$  orbitals of the upper and lower layers significantly decreases and the conductance reduces to discrete resonant peaks. The width of the transmission peaks reduces as the inter-plane distance increases, showing the typical resonant transport characteristics in systems where the molecules are only weakly coupled to the leads. The first peak below Fermi level (0.4 eV) corresponds well to the HOMO level (0.37 eV) of isolated pentacene and is right-shifted monotonously towards the Fermi level as the bridging oligoacenes are extended from pentacene to decacene, as can be seen in Fig. 6-2(b).

### 6.2.3 Intertube tunneling with covalent linkers

In order to improve the intertube conductivity by a sidewall functionalized organic polymer, an ideal sidewall linker must be able to couple the frontier orbitals to those of the nanotubes and must be conductive itself. It would be best if the linker could preserve the conductivity of pristine CNTs as much as possible, especially for high-degree functionalizations. To fulfill all the above criteria, we first consider the [1+2] cycloadditions of carbenes or nitrenes which are able to preserve conductance [72, 67] of the nanotube through a sidewall bond cleavage, as has been proven by first-principles calculations. [72, 67] The linker we test on the polyacene model has an aromatic moiety (as in most conductive polymers) substituted with two nitrene groups which

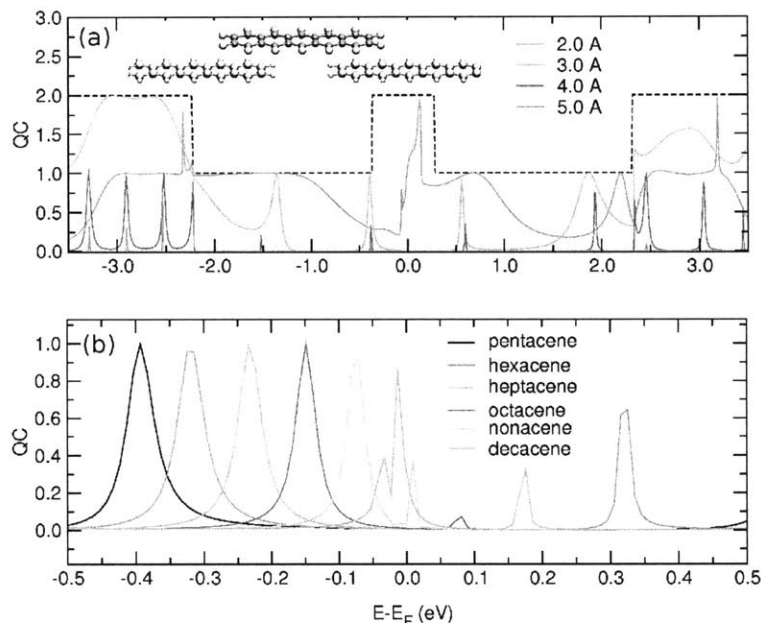


Figure 6-2: The quantum conductance of a broken polyacene junction bridged by (a) a pentacene molecule with varying adsorption distance (b) different nanoribbon fragments in which the adsorption distance is fixed as 3 Å

connect to the CNT-surface, *e.g.* a nitrene-linked pyrazine. We suspect that the long pair  $p_z$  orbital on the nitrene atoms might be able to couple the  $\pi$  orbitals of SWNT to the aromatic  $\pi$  orbitals, and thus, increase intertube tunneling. If that were true, then the orientation effect of the pyrazine group would also have an effect. We perform a relaxation calculation and find that the most stable configuration for the pyrazene-nitrene-linked polyacene junction is for the pyrazine plane to lie perpendicular rather than parallel to the polyacene axis, but both configurations give essentially zero conductance at the Fermi level. The sparse narrow peaks are also characteristic of resonant tunneling and indicate no substantial coupling between the two leads. This result could only be explained by the increase of inter-polyacene junction distance from the natural 3.5 Å to 7 Å, further deteriorating already poor tunneling. This scenario corresponds to the experimental situation where the existence of polymer cross-linkers could push CNTs further away from each other and affect negatively electrical conductivity.

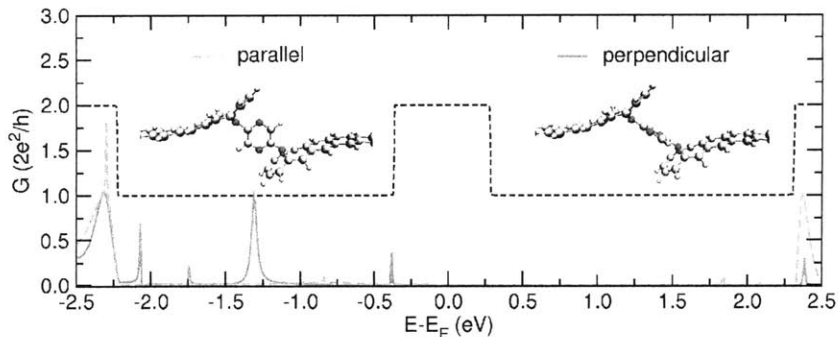


Figure 6-3: The quantum conductance of a broken polyacene junction bridged by a covalent pyrazene-nitrene linker

#### 6.2.4 Intertube tunneling with transition metal coupling

Alternatively, we temporarily shift our focus away from typical organic polymers and turn to coordination chemistry on SWNTs. We consider a sidewall functionalization via coordination with transition metals, inspired by ferrocene-based molecular wires[100]. Transition metals are well known for their versatile bonding scheme with aromatic systems, including the sandwich-type metallocenes. It was recently shown experimentally that when two extended polyphenylethynyl fragments were connected by a ferrocene unit in the middle, the conductance at zero source-drain bias  $V$  was significantly improved with respect to the ferrocene-absent analog, and a broad resonance peak 30 meV above the Fermi level was revealed by first-principles calculations. This is because the  $d$  orbitals of transition metals are close to the Fermi level and interact strongly to the  $\pi$  orbitals of the conjugated backbone. For our purpose it might be reasonable to first consider a junction containing a chromium atom since Cr is known to form the stable metallocene, bis(benzene)chromium, which shares the same hexagonal aromatic moiety as CNTs.

We examine three structures of polyacene involving Cr coordination and intertube-tunneling as shown in Fig. 6-4. The relaxed inter-plane distances are around 3.30

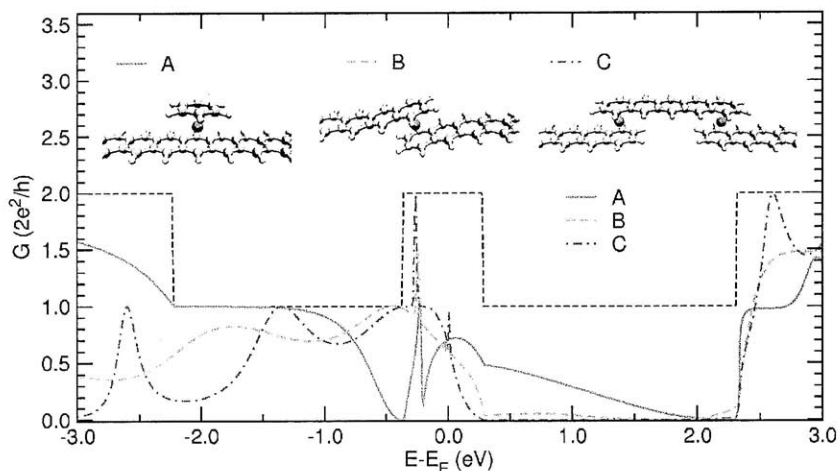


Figure 6-4: The quantum conductance of A). a pristine polyacene scattered by a bis(benzene)chromium defect, B). a broken polyacene junction bridged by a chromium atom, and C). a broken polyacene junction bridged by an adsorbed pentacene and two sandwiched chromium atoms.

Å for all three systems. The strong hybridization between Cr  $d$  orbitals with the polyacene  $\pi$  orbitals acts as a strong scattering center for the perfect polyacene chain (structure A in Fig. 6-4), decreasing the transmission to 30% of that of the undoped pristine polyacene, but also serves as an excellent electrical bridge for broken polyacene segments for the same reason. All three systems give a broad transmission feature, and show a quantum conductance around 0.6 at the Fermi level and a sharp resonant peak at 0.25 eV below Fermi energy. The eigenchannel analysis of the transmission spectrum of structure B shown in Fig. 6-5 reveals a conjugated eigenchannel traversing the entire molecule from lead to lead at Fermi level, giving rise to high transmission. It is evident to see that the broad band at Fermi level originates from the HOMO-2 in bis(benzene)chromium involving Cr  $d_{xy}$  orbital which strongly couples to the  $p$  orbitals of both benzene molecules. The resonant peak slightly below the Fermi level corresponds to the HOMO in bis(benzene)chromium with Cr  $d_{z^2}$  orbital, which only weakly interacts with the benzene  $\pi$  orbitals.

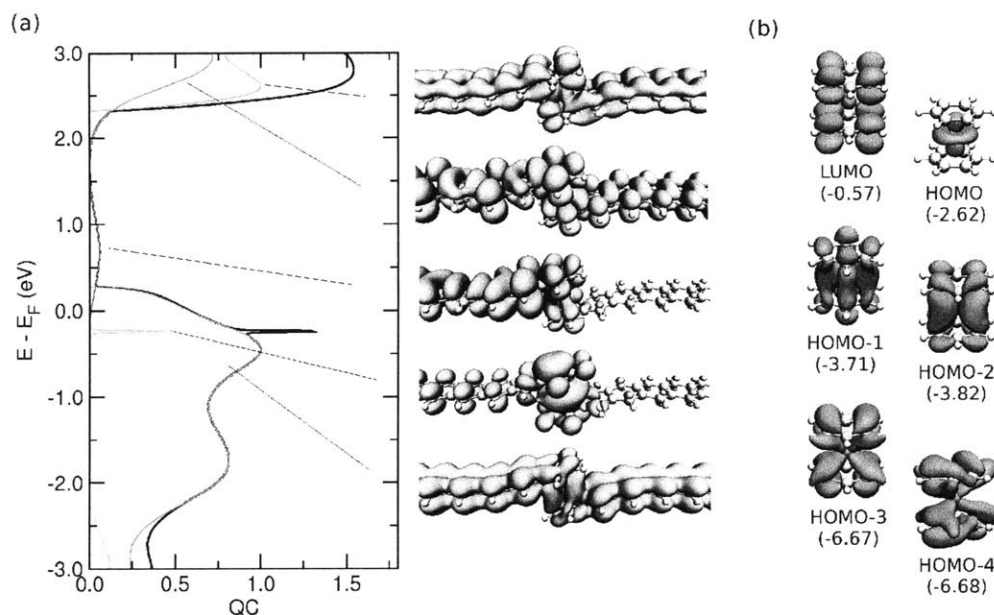


Figure 6-5: (a) The eigenchannel decomposition and the density of corresponding eigenchannels of quantum conductance of configuration B in Fig. 6-4 near the Fermi level; (b) The energy and frontier molecular orbitals of bis(benzene)chromium.

## 6.3 Intertube conductivity of carbon nanotubes

### 6.3.1 Carbon nanotube junctions cross-linked by transition metals

The bulk conductivity of a macroscopic CNT network is a very complicated quantity since it can only be described by the percolation model, which depends on the length, the morphology and the atomistic structure at the contact of CNTs. Our polyacene model system study shows that the transmission of a broken polyacene junction can be improved dramatically by a single transition metal atom doping. Nevertheless, a polyacene chain is only one-benzene wide so it should not come as a surprise after all that an  $\eta^6$ -coordinated transition metal atom could almost fully connect the  $\pi$  orbitals between the top and bottom polyacene fragments. A CNT, on the other hand, has much larger dimension and only a small fraction of the  $\pi$  orbitals between two tubes can be directly coupled by a single TM-atom doping. Thus it becomes

interesting to investigate how much improvement on the poor conductivity of CNT networks can be achieved by transition-metal coordination.

In the past coordination chemistry was a less studied topic in the field of CNTs, but recently more diverse functionalization of CNTs have been explored by decorating the CNT sidewall with transition metals. It has been experimentally shown that the CNTs nanocomposites doped by transition metal nanoparticles have great potential applications in fuel cells, sensing, catalysis, hydrogen storage and magnetic nano-devices. As for single atom transition metal complexes, experimental works incorporating iridium, rhodium, and osmium complexes with CNTs have been studied [101, 102, 103] and theoretical calculations concerning CNTs functionalized by transition metals such as  $\text{Cr}(\text{CO})_3$  and  $\text{OsO}_4$  or Vaska's complex have also been performed [104, 105, 106]. The coordination between the transition metals and the CNT  $\pi$  manifold can vary between  $\eta^2$ ,  $\eta^4$  or  $\eta^6$ , involving two, four or six  $\pi$  electrons on the CNT surface, respectively, but for most TMs the most stable configuration is the  $\eta^6$ -coordination where the TM atom lies about 1.5 Å above the center of a hexagon, which is the same configuration assumed in the polyacene model. In order for the transition metal to couple the  $\pi$  orbitals between different nanotubes, it must be able to form a local sandwich structure between neighboring CNTs.



We start by calculating the binding energies and stable geometries of a single TM atom adsorbed on a CNT, or sandwiched between two CNTs. The binding geometries are determined by optimizing all atomic positions including the adsorbate atom and 5 units of carbon atoms of a (5,5) CNT (120 or 240 atoms for one or two CNTs, respectively). The first binding energies are obtained when a single TM atom is adsorbed to the surface of a single CNT, from the expression

$$E_b^1 = E_T[\text{CNT}] + E_T[\text{TM}] - E_T[\text{TM-CNT}] \quad (6.1)$$

in terms of the total energies of the fully optimized bare nanotube ( $E_T[\text{CNT}]$ ), the free transition metal atom ( $E_T[\text{TM}]$ ), and the TM adsorbed SWNT ( $E_T[\text{TM}+\text{CNT}]$ ), of the lowest magnetic ground states, respectively. We define the second binding energy as the energy further released when a second tube is absorbed to a TM-decorated CNT, giving rise to a "sandwich" structure. The secondary binding energy  $E_b^2$  is calculated with the equation:

$$E_b^2 = E_T[\text{CNT}] + E_T[\text{TM-CNT}] - E_T[\text{CNT-TM-CNT}] \quad (6.2)$$

---

Atom	$d_{TM-C}$ (Å)	$E_b^1$ (eV)	$\mu$ ( $\mu_B$ )	$d_{TM-C}$ (Å)	$E_b^2$ (eV)	$\mu$ ( $\mu_B$ )
Sc	2.34	2.04	1.03(1)	2.42	2.10	1.03(1)
Ti	2.28	1.97	2.36(2)	2.34	2.27	2.12(2)
V	2.31	1.50	4.30(3)	2.31	2.08	3.46(3)
Cr	2.47	0.37	6.20(4)	2.34	1.37	4.85(2)
Mn	2.54	0.42	6.29(5)	2.38	1.06	4.99(3)
Fe	2.25	0.96	4.40(4)	2.31	1.45	3.09(2)
Co	2.15	1.26	1.98(1)	2.29	1.28	3.24(3)
Ni	2.16	1.56	0	2.39	1.01	0
Cu	2.40	0.38	1.04(1)	2.42	0.82	1.03(1)
Zn	4.04	0.05	0	4.11	0.12	0

Table 6.1: Calculated binding energies ( $E_b^1$ ,  $E_b^2$  as defined in Eq. 6.1 and Eq. 6.2), average carbon-TM atom distances ( $d_{TM-C}$ ), and the absolute magnetization per unit cell  $\mu_B$  (the number of unpaired electrons is listed inside the parenthesis) of a single TM atom adsorbed on (Left): the surface of a (5,5) CNT or (Right): between two (5,5) CNTs.

The geometry, binding energy, and magnetic moment of the single TM atom ad-

sorbed to the CNT are presented in Table 6.1. The calculated values for  $E_b^1$  are comparable to a single TM atom adsorbed on to a (8,0) or a (6,6) CNT in other studies [107]. Owing to the curvature effect, the binding energies are higher for single transition metals adsorbed on SWNT surfaces than on the graphene surfaces and are in the range of 0 to 2 eV, indicating significant chemisorption. The binding is the strongest for early transition metals such as Sc, Ti, and V, and is the weakest for half-filled (Cr, Mn and Fe), or fully-filled TM metals (Cu and Zn). Surprisingly, although Cr is known to form the stable bis(benzene)metallocene, it gives the smallest binding energy (0.37 eV) other than zinc when it binds to a single CNT. A further detailed examination reveals that the small binding energy comes from the fact that a free Cr atom has an extremely stable half-filled configuration  $4s^13d^5$ , rather than the formation of a specifically unstable adsorption structure. The second binding energy  $E_b^2$  is comparable to  $E_b^1$  for most metal atoms, except in the case of half-filled metals (Cr, Mn, and Fe), where the second adsorption event could release 0.5 to 1 eV more energy than the first one since the initial state involves no particularly stable free metal atoms. The intertube distance in a sandwich structure is around 3.4 Å, which is also close to the natural *pi-pi* stacking distance in graphite.

The interaction strength between a single TM to the CNT surface is directly reflected by the conductance calculation of a pristine CNT adsorbed by a single TM atom as shown in Fig. 6-6. The quantum conductance in the spin up channel in Fig. 6-6(a) shows strong scattering for partially filled 3d transition metals Sc, Ti, V, Cr, Co, Ni and weak to negligible scattering when the spin up 3d orbitals are completely filled as in Mn, Fe, Zn. In the spin down channel, the transport shows strong scattering characteristic for all partially filled 3d metals except for Cu and Zn (Fig. 6-6(b)). The interaction strength could be correlated to the half width of the transmission "valleys" which represents the extent of scattering when the  $\pi$  channel of a pristine CNT is perturbed by the 3d orbital of the TM. The early transition metals, Sc, Ti, V, Cr, show broad scattering features in both spin up and down channels compared to other 3d atoms and are expected to offer a stronger coupling between



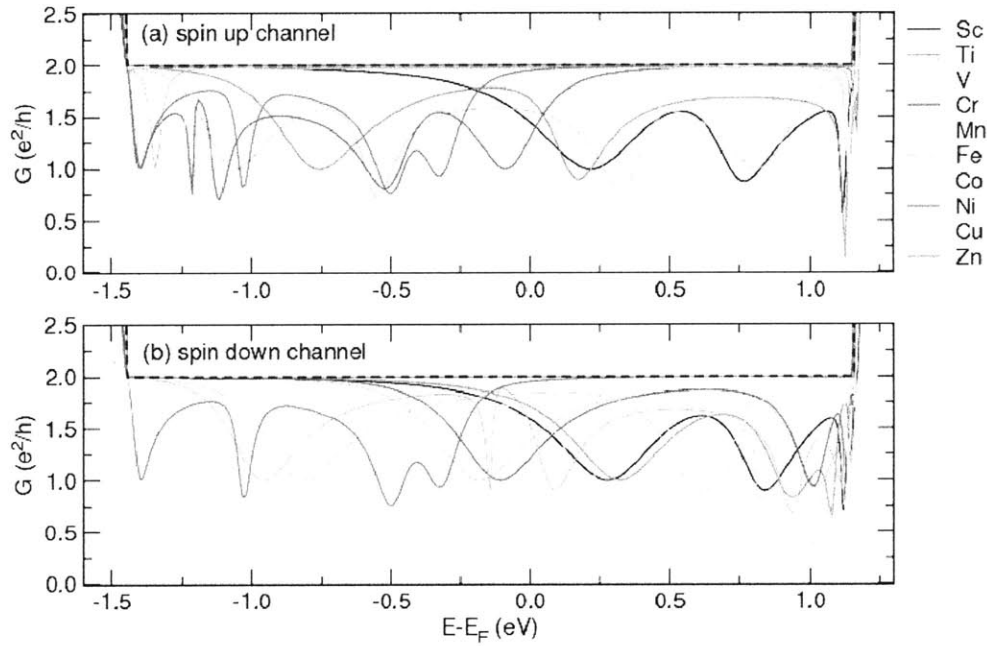


Figure 6-6: The (a) spin up and (b) spin down quantum conductance near the Fermi level of a (5,5)-CNT scattered by a single first-row transition metal adsorption (in the configuration of the left of Table 6.1. The quantum conductance of a pristine (5,5) CNT is shown in the black dashed curve.

adjacent nanotubes and a better intertube conductivity in a nanotube junction. Selected atoms are studied in the CNT-TM-CNT sandwich connection configuration as shown in Fig. 6-7. At a first glance it is already stunning to see such high intertube quantum conductance could ever be achieved in a SWNT junction. Of the few metal atoms tested, Ti, V, Cr shows particularly broad transport features around the Fermi level and could recover the quantum conductance up to about  $0.8 G_0$  (the quantum conductance of a pristine armchair CNT in this energy window is  $2 G_0$ ). This is a dramatic improvement over unconnected nanotube junctions, which shows essentially zero conductance at the Fermi level. Note that in Fig. 6-7 the configuration of the "no TM" junction is taken directly from the CNT-Cr-CNT structure by removing the

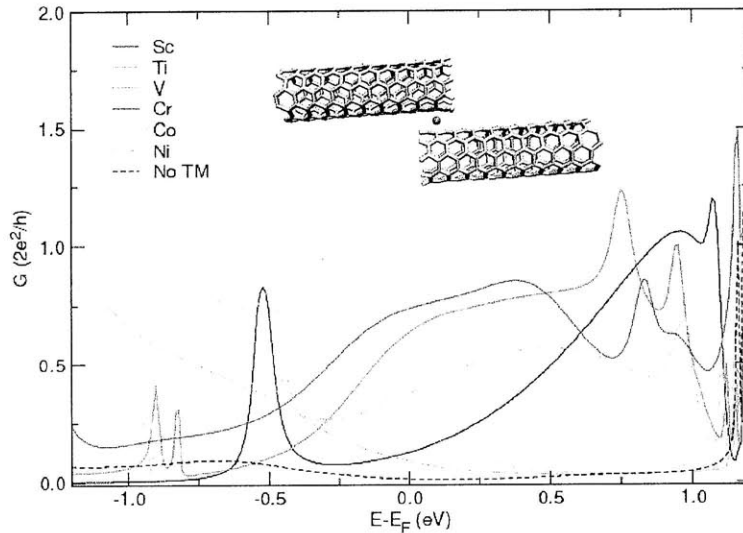
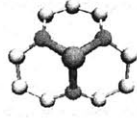


Figure 6-7: Quantum conductance near the Fermi level of a (5,5)-CNT junction connected by a 3d transition metal. The quantum conductance of the same junction without the transition metal is shown in the "no TM" curve, with the geometry directly taken from the CNT-Cr-CNT structure by removing the central Cr atom, to show the contribution of through space tunneling between the  $\pi$  orbitals unassisted by TM coordination.

central Cr atom. In realistic scenarios the intertube conductance of a SWNT junction is likely to be even lower since the tubes would slightly push each other away from the  $3.2 \text{ \AA}$ , the surface distance between adjacent tubes pulled by the transition metals in the CNT-TM-CNT junction.

### 6.3.2 Nitrogen doped carbon nanotube junctions cross-linked by transition metals

If the intertube conductivity of SWNT networks can be improved by transition metal coordination, then the main question left would be that if one is able to disperse the TM metals in a CNT networks in the way that neighboring tubes are coupled



Atom	$d_{TM-N}$ (Å)	$E_b^1$ (eV)	$\mu$ ( $\mu_B$ )	$d_{TM-N}$ (Å)	$E_b^2$ (eV)	$\mu$ ( $\mu_B$ )
Sc	2.01	6.83	0	2.19	5.14	1.20(1)
Ti	1.93	6.69	1.45(1)	2.12	5.37	0
V	1.91	6.11	3.23(2)	2.08	4.96	2.71(3)
Cr	1.88	4.24	4.48(3)	2.06	4.87	4.06(4)
Mn	1.94	4.19	5.59(4)	2.02	3.92	3.19(3)
Fe	1.87	4.97	4.65(3)	2.01	3.97	0
Co	1.85	5.20	2.66(2)	2.02	3.04	1.11(1)
Ni	1.84	5.04	1.66(1)	2.11	2.80	2.36(2)
Cu	1.88	3.81	0	2.17	1.95	1.23(1)
Zn	2.01	1.73	1.08(1)	2.18	3.26	0

Table 6.2: Calculated binding energies ( $E_b^1$ ,  $E_b^2$  as defined in Eq. 6.1 and Eq. 6.2), average nitrogen-TM atom distances ( $d_{TM-N}$ ), and the absolute magnetization per unit cell  $\mu_B$  (the number of unpaired electrons is listed inside the parenthesis) of a single TM atom adsorbed on (Left): the surface of a (5,5)  $CN_xNT$  or (Right): between two (5,5)  $CN_xNT$ s.

efficiently to each other through the local sandwich junction formation, or, in other words, whether such a junction is experimentally possible. SWNTs have been used as support material for the dispersion and stabilization of metal nanoparticles and the hybrid materials offer several applications in catalysis, nanoelectronics, and optics [108, 109]. Nevertheless, most studies are limited to noble metal nanoparticles, *e.g.*  $Au$ ,  $Ag$ ,  $Pt$ ,  $Pd$  and involve pre-treatment on the CNTs such as acid oxidations, which could impair the electrical and mechanical properties of the CNTs. Alternatively, it has recently been proposed to utilize N-doped CNTs (the  $CN_xNT$ s) as a support material to immobilize various TM nanoparticles. The pyridine-like nitrogen configurations, which have been found to be the favorable structure in  $CN_xNT$ s both from first-principles calculations and XPS measurements [110], could lead to a strong

hybridization between the TM atom and the nitrogen atoms even in the absence of pre-modifications. This could be a promising and useful characteristic for enhancing intertube conductivity by TM coordination.

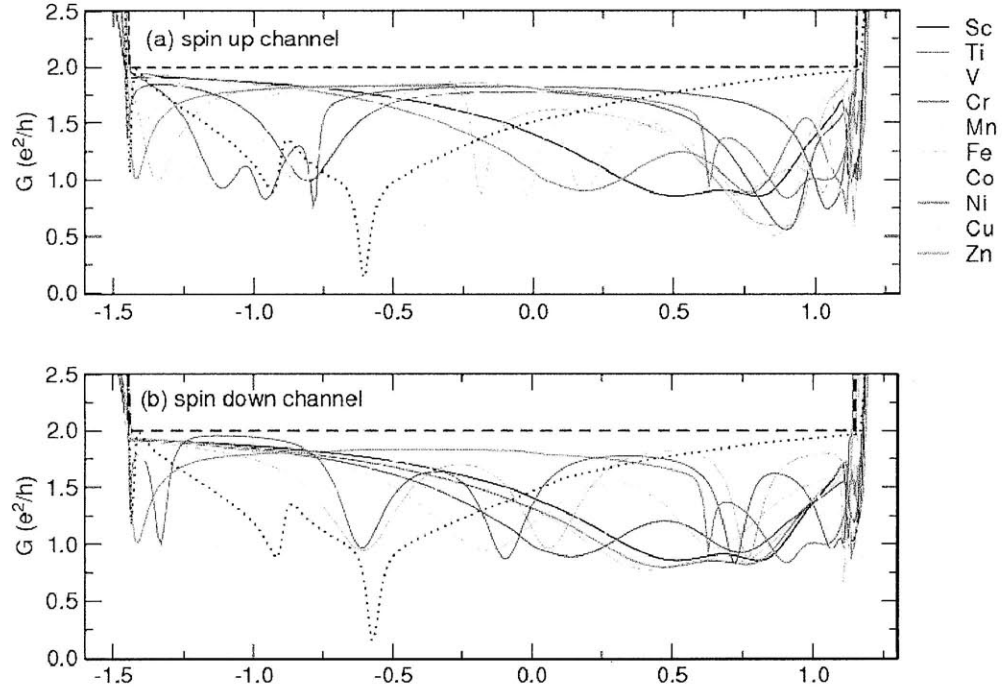


Figure 6-8: The (a) spin up and (b) spin down quantum conductance near the Fermi level of a (5,5)- $\text{CN}_x\text{NT}$  scattered by a single first-row transition metal adsorption (in the configuration of the left of Table 6.2). The quantum conductance of a pristine (5,5) CNT is shown in the black dashed curve; the quantum conductance of a (5,5)  $\text{CN}_x\text{NT}$  is shown in the black dotted curve.

To quantify the effect of pyridine-like defects in nanotube-TM coupling, we again study the geometry, binding energy, and magnetic moment of the single TM atom adsorbed to  $\text{CN}_x\text{NTs}$  as presented in Table 6.2. The obtained binding energy, geometry and magnetic structure are comparable to previous studies of TM metals attached to a pyridine defect on a (10,0) CNT [111]. The first thing to note is that the binding energies of most 3d transition metals to the (5,5)  $\text{CN}_x\text{NT}$  range from 4 to 6 eV and are on average three times or higher compared to a pristine (5,5) CNT, due to the

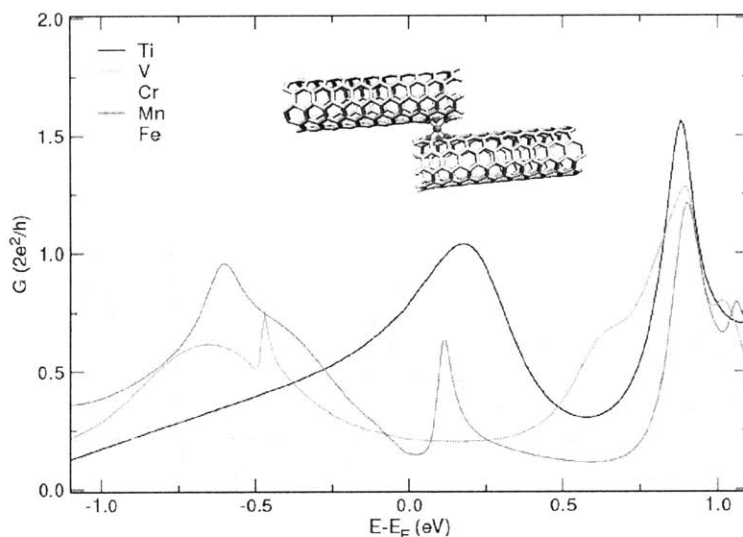


Figure 6-9: Quantum conductance near the Fermi level of a (5,5)-CNT junction connected by a 3d transition metal. The quantum conductance of a pristine (5,5) CNT is shown in the black dashed curve.

multiple TM-N bonds formed at the pyridine vacancy sites. Recent first-principles calculation predicts high possibility of forming single TM atom adsorption on these pyridine sites. The energy barrier for a metal to disperse to another position on the tube surface was estimated to as high as 7 eV [111] and thus such is unlikely to happen. The secondary binding energies are also on average two times higher than those of CNTs. One thing to note is that the intertube distance of a sandwich structure in the  $CN_xNT$  could be bring to as close as 3 Å by the transition metals, which is at least 0.5 Å shorter than the natural  $\pi - \pi$  stacking distance. This indicates that the bonding between the TM atom and the pyridine moiety is strong enough to overcome the natural repulsion between neighboring tubes.

Typically N-doped CNTs are expected to show n-type or metallic behavior and greater electron mobility since the extra electron from the graphitic nitrogen atoms would create a donor state close to the Fermi level, but a pyridine-like nitrogen doping

does not contribute to electron carriers. Rather, the local pyridine structure induces a highly defective trap state [112] and appears a large dip near the Fermi level in the transport of a (5,5)  $\text{CN}_x\text{NT}$  as in Fig. 6-8. Nevertheless, the quantum conductance of a  $\text{CN}_x\text{NT}$  is largely recovered by the adsorption of a metal atom to the pyridine site, indicating that the broken  $\pi$  bands of the tube is reconnected by the TM  $3d$  - nitrogen  $2p$  bonding. Unlike the case of TM-CNTs where only some of the metal atoms would induce strong scattering in the transport (Fig. 6-6), the transmission of the  $\text{CN}_x\text{NT}$  is affected by all transition metals significantly, including zinc. Nevertheless, the transmission "dips" of TM-adsorbed  $\text{CN}_x\text{NT}$ s have narrower half-widths comparing to TM-doped CNTs since the TM metal does not interfere directly to the  $\pi$  orbitals of a CNT atop as in a TM-doped CNTs in the metallocene configuration. The quantum conductance calculation of the  $\text{CN}_x\text{NT}$  junction connected through the pyridine-TM-pyridine sandwich structure also shows significant improvement, as high as  $1.0 G_0$ , as shown in Fig. 6-9. It was found that in this configuration the two tube terminals come extremely close to each other and are only  $2.6 \text{ \AA}$  apart. Therefore it can be expected that the conductance would also include substantial contribution from direct intertube tunneling. Such a short intertube distance is unlikely to exist in real SWNT networks, but even an intermediate intertube distance and a TM sandwiching moiety (*e.g.* a TM coordinated to the  $\eta^6$  ring of one tube and the pyridine site of the other tube) should offer much better intertube conductance.

In summary, we have studied the intertube conductivity in a SWNT network with first-principle calculations on SWNT junctions. We have shown the limitations of intertube tunneling in bare CNTs or CNTs functionalized with common organic polymers. Alternatively, we find the intertube tunneling can be greatly enhanced by transition metal adsorption on CNT surfaces. The adsorption geometries and binding energies of first-row transition metals on a (5,5) CNT or sandwiched between two (5,5) CNTs are studied systematically. We also find that the nitrogen-doped CNT binds with TM atoms three times stronger than pure CNT does. Such sandwich structures are thus more likely to exist in TM-doped  $\text{CN}_x\text{NT}$  networks and could offer significant

enhancement on electrical conductivities of SWNT networks by orders of magnitude from current experimental findings.





# Chapter 7

## Conclusions

In this work, we apply the Landauer formalism in a basis of maximally localized Wannier functions to study the electronic structure and quantum conductance of nanoscale materials. We perform detailed studies on transmission of single molecules governed by quantum interference effect, conductance switching of functionalized carbon nanotubes controlled by sidewall bond cleavage, and intertube conductivity of nanotube junctions bridged by transition metal atoms. We demonstrate how minute differences in the atomistic details could have a huge impact on transport properties throughout different scales, ranging from a few nanometers in a single molecule to micrometers in an extended carbon nanotube or carbon nanotube networks.

For single-molecule transport, we show that a minimal Wannier basis transformed Hamiltonian for the molecular part in conjunction with the wide band limit approximation for the lead part is sufficient to provide quantitative results and is able to capture all important physics without the expense of full-atomistic lead-molecule-lead calculations. A detailed study of the quantum interference effect controlled by hydrogen tautomerization of porphyrinic systems is performed. We also show that the frontier orbital symmetry interpretation for quantum interference effect is the zeroth order approximation to the recently proposed molecular conductance orbital analysis. In porphyrin family molecules, the quantum interference effect could lead to orders of magnitude in transmission at or near the Fermi level when hydrogen tautomerization

occurs, which essentially marked the behavior of a single molecular switch. The on/off electrical transmission of porphyrin molecules may also be used as a novel memory device in which each porphyrin unit in the organically assembled "tape-porphyrin" systems serves as one "quantum bit" and has two hydrogen tautomeric states representing "0" and "1". This could lead to important breakthroughs in the fabrication of molecular memory circuit.

In the second study we identify the role of through-space periconjugation in controlling the sidewall bond-cleavage chemistry in [1+2] cycloaddition functionalized CNTs. While almost all divalent functionalizations on CNTs break the sidewall bonds in response to the high tension in the cyclopropane moiety formed in [1+2] cycloaddition reactions, a carefully arranged  $\pi$  orientations of the functional group with respect to the CNT surface could strongly stabilize the closed bond conformation even for CNTs with very high curvature. Exploiting the periconjugation effect, we investigate major classes of chemical functionalizations well within reach of experimental capabilities that allow for instantaneous and reversible control of conductance controlled by chemical or electrochemical means. As opposed to most of the work in molecular electronics, where microscopic control and repeatability remain major issues even under the most careful conditions, this study applies directly to nanotube-based devices, covering broad classes of chemical functionalizations, and resulting in effects that are extremely robust.

Although the conductivity of single nanotubes can be manipulated by chemical functionalizations, at present most realistic applications of CNTs are carried out in the form of CNT networks or thin films, in which the transmission is dominated by intertube rather than intratube conductivity. We offer potential solutions to a realistic experimental problem in carbon nanotube networks that has rarely been considered in theoretical studies. The CNT junction cross-linked by transition metals shows an increase in transmission over 2 orders of magnitude compare to bare (un-linked) junctions, where the only mechanism of electron transport is tunneling which quickly

decays exponentially with intertube distance. The strong hybridization between the  $d$  orbitals in transition metals with the  $\pi$  orbitals in a CNT serves as an excellent electrical bridge for broken polyacene or CNT junctions, as shown in the eigenchannel analysis. We find that the binding energies between single transition metal adatoms and SWNT can even be improved to three times or higher when a pyridine-like defect is involved in the nitrogen-doped CNTs. Even though the pyridine defect is a strong scattering defect compare to the pristine CNT, the transition metal adsorption recovers largely the transmission at the Fermi level, and couples as efficiently the  $\pi$  systems of adjacent nanotubes as in the CNT-TM-CNT system.

Finally, we would like to emphasize that in choosing and designing our model systems, we have been especially careful in ensuring that the systems we studied are well within reach of experimental capabilities or can be directly related to current experimental setup. Throughout the course of our pursuit, we have come to realize that although the unconstrained imagination of theoreticians could lead to undiscovered territories, overly impractical (or even incorrect) assumptions would only result in meaningless calculations and may not provide much substantial information regarding realistic breakthrough. Therefore it is our sincere hope that the studies carried out in this thesis could contribute to a novel paradigm for molecular and nanoscale electronics, and serve as a reference and a source of inspiration for future experimental studies.



# Bibliography

- [1] A. Aviram and M. A. Ratner. Molecular rectifiers. *Chem. Phys. Lett.*, 29(2):277–283, 1974.
- [2] A. Nitzan and M. A. Ratner. Electron transport in molecular wire junctions. *Science*, 300(5624):1384–1389, 2003.
- [3] A. K. Feldman, M. L. Steigerwald, X. Guo, and Colin Nuckolls. Molecular electronic devices based on single-walled carbon nanotube electrodes. *Acc. Chem. Res.*, 41(12):1731–1741, 2008.
- [4] B. Ulgut and H. D. Abruna. Electron transfer through molecules and assemblies at electrode surfaces. *Chem. Rev.*, 108(7):2721–2736, 2008.
- [5] C. A. Martin, D. Ding, J. K. Sørensen, T. Bjørnholm, J. M. van Ruitenbeek, and H. S. J. van der Zant. Fullerene-based anchoring groups for molecular electronics. *J. Am. Chem. Soc.*, 130(40):13198–13199, 2008.
- [6] G. K. Ramachandran, T. J. Hopson, A. M. Rawlett, L. A. Nagahara, A. Primak, and S. M. Lindsay. A bond-fluctuation mechanism for stochastic switching in wired molecules. *Science*, 300(5624):1413–1416, 2003.
- [7] C. Li, I. Pobelov, T. Wandlowski, A. Bagrets, A. Arnold, and F. Evers. Charge transport in single au — alkanedithiol — au junctions: Coordination geometries and conformational degrees of freedom. *J. Am. Chem. Soc.*, 130(1):318–326, 2008.
- [8] S. M. Lindsay and M. A. Ratner. Molecular transport junctions: Clearing mists. *Adv. Mater.*, 19(1):23–31, 2007.
- [9] J. Ulrich, Donna Esrail, W. Pontius, L. Venkataraman, D. millar, and L. H. Doerrer. Variability of conductance in molecular junctions. *J. Phys. Chem. B*, 110(6):2462–2466, 2006.
- [10] X. Gue, J. P. Small, J. E. Klare, Y. Wang, M. S. Purewal, I. W. Tam, B. H. Hong, R. Caldwell, L. Huang, S. O’Brien, J. Yan, R. Breslow, S. J. Wind, J. Hone, P. Kim, and C. Nuckolls. Covalently bridging gaps in single-walled carbon nanotubes with conducting molecules. *Science*, 311(5759):356–359, 2006.

- [11] S. Datta. *Electronic Transport in Mesoscopic Systems*. Cambridge University Press, 1995.
- [12] S. Datta. *Quantum Transport: Atom to Transistor*. Cambridge University Press, 2005.
- [13] D. Q. Andrews, G. C. Solomon, R. P. Van Duyne, and M. A. Ratner. Single molecule electronics: Increasing dynamic range and switching speed using cross-conjugated species. *J. Am. Chem. Soc.*, 130(51):17309–17319, 2008.
- [14] S. Y. Quek, L. Venkataraman, H. J. Choi, S. G. Louie, M. S. Hybertsen, and J. B. Neaton. Amine-gold linked single-molecule circuits: Experiment and theory. *Nano. Lett.*, 7(11):3477–3482, 2007.
- [15] A. Szabo and N. S. Ostlund. *Modern Quantum Chemistry*. Dover Publications, 1996.
- [16] R. G. Parr and W. Yang. *Density-Functional Theory of Atoms and Molecules*. Oxford University Press, 1989.
- [17] W. Koch and M. C. Holthausen. *A Chemist's Guide to Density Functional Theory*. Wiley-VCH, 2000.
- [18] P. Hohenberg and W. Kohn. Inhomogeneous electron gas. *Phys. Rev. B*, 136(3):864871, 1964.
- [19] W. Kohn and L. J. Sham. Self-consistent equations including exchange and correlation effects. *Phys. Rev. A*, 140(4):1133–1138, 1965.
- [20] J.P. Perdew, K. Burke, and M. Ernzerhof. Generalized gradient approximation made simple. *Phys. Rev. Lett.*, 77(18):3865–3868, 1996.
- [21] P. Giannozzi, S. Baroni, N. Bonini, M. Calandra, R. Car, C. Cavazzoni, D. Ceresoli, G. L. Chiarotti, M. Cococcioni, I. Dabo, and *et. al.* Quantum-espreso: A modular and open-source software project for quantum simulations of materials. *J. Phys.: Condens. Matter*, 21(39):395502, 2009.
- [22] R. M. Martin. *Electronic Structure: Basic Theory and Practical Methods*. Cambridge University Press, 2004.
- [23] M. C. Payne, M. P. Teter, D. C. Allan, T. A. Arias, and J. D. Joannopoulos. Iterative minimization techniques for *Ab Initio* total-energy calculations: Molecular dynamics and conjugate gradients. *Rev. Mod. Phys.*, 64(4):1045–1097, 1992.
- [24] H. J. Monkhorst and J. D. Pack. Special points for brillouin-zone integrations. *Phys. Rev. B*, 13(12):5188–5192, 1976.
- [25] G. H. Wannier. The structure of electronic excitation levels in insulating crystals. *Phys. Rev.*, 52(3):191–197, 1937.

- [26] N. Marzari and D. Vanderbilt. Maximally localized generalized wannier functions for composite energy bands. *Phys. Rev. B*, 56(20):12847–12865, 1997.
- [27] S. F. Boys. Construction of some molecular orbitals to be approximately invariant for changes from one molecule to another. *Rev. Mod. Phys.*, 32(2):296–299, 1960.
- [28] E. I. Blount. Formalisms of band theory. *Surf. Sci.*, 13:305–373, 1962.
- [29] I. Souza, N. Marzari, and D. Vanderbilt. Maximally localized wannier functions for entangled energy bands. *Phys. Rev. B*, 65(3):035109, 2002.
- [30] L. E. Ballentine. *Quantum Mechanics*. World Scientific, 1998. Chapter 6: Scattering.
- [31] R. Landauer. Electrical resistance of disordered one-dimensional lattices. *Phil. Mag.*, 21(172):863–867, 1970.
- [32] D. S. Fisher and P. A. Lee. Relation between conductivity and transmission matrix. *Phys. Rev. B*, 23(12):6851–6854, 1981.
- [33] M. B. Nardelli. Electronic transport in extended systems: Application to carbon nanotubes. *Phys. Rev. B*, 60(11):7828–7833, 1999.
- [34] M. B. Nardelli and J. Bernholc. Mechanical deformations and coherent transport in carbon nanotubes. *Phys. Rev. B*, 60(24):R16338, 1999.
- [35] M. B. Nardelli, J.-L. Fattebert, and J. Bernholc. O(n) real-space method for *Ab Initio* quantum transport calculations: Application to carbon nanotubemetal contacts. *Phys. Rev. B*, 64(24):245423, 2001.
- [36] D. H. Lee and J. D. Joannopoulos. Simple scheme for surface-band calculations. i. *Phys. Rev. B*, 23(10):4988, 1981.
- [37] D. H. Lee and J. D. Joannopoulos. Simple scheme for surface-band calculations. ii. the green’s function. *Phys. Rev. B*, 23(10):4997, 1981.
- [38] M. P. LÓpez Sancho, J. M. LÓpez, and J. Rubio. Quick iterative scheme for the calculation of transfer-matrices-application to mo(100). *J. Phys. F*, 14(5):1205–1215, 1984.
- [39] M. P. LÓpez Sancho, J. M. LÓpez, and J. Rubio. Highly convergent schemes for the calculation of bulk and surface green-functions. *J. Phys. F*, 15(4):851–858, 1985.
- [40] Y. Meir and N. S. Wingreen. Landauer formula for the current through an interacting electron region. *Phys. Rev. Lett.*, 68(16):2512–2515, 1992.
- [41] M. Paulsson and M. Brandbyge. Transmission eigenchannels from nonequilibrium green’s functions. *Phys. Rev. B*, 76(11):115117, 2007.

- [42] M. Mayer, H. B. Weber, J. Reichert, M. Elbing, C. von Hnisch, D. Beckmann, and M. Fischer. Electric current through a molecular rod—relevance of the position of the anchor groups. *Angew. Chem. Intl. Ed.*, 42(47):5834–5838, 2003.
- [43] C. Patoux, C. Coudret, J.-P. Launay, C. Joachim, and A. Gourdon. Topological effects on intramolecular electron transfer *via* quantum interference. *Inorg. Chem.*, 36(22):5037–5049, 1997.
- [44] S.-H. Ke, W. Yang, and H. U. Baranger. Quantum-interference-controlled molecular electronics. *Nano. Lett.*, 8(10):3257–3261, 2008.
- [45] D. M. Cardamone, C. A. Stafford, and Sumit Mazumdar. Controlling quantum transport through a single molecule. *Nano. Lett.*, 6(11):2422–2426, 2006.
- [46] T. Markussen, R. Stadler, and K. S. Thygesen. The relation between structure and quantum interference in single molecule junctions. *Nano. Lett.*, 10(10):4260–4265, 2010.
- [47] G. C. Solomon, D. Q. Andrews, T. Hansen, R. H. Goldsmith, M. R. Wasielewski, R. P. Van Duyne, and M. A. Ratner. Understanding quantum interference in coherent molecular conduction. *J. Chem. Phys.*, 129(5):054701, 2008.
- [48] N. D. Lang and Ph. Avouris. Electrical conductance of individual molecules. *Phys. Rev. B*, 64(12):125323, 2001.
- [49] K. Yoshizawa, T. Tada, and A. Staykov. Orbital views of the electron transport in molecular devices. *J. Am. Chem. Soc.*, 130(29):9406–9413, 2008.
- [50] M. del Valle, R. Gutiérrez, C. Tejedor, and G. Cuniberti. Tuning the conductance of a molecular switch. *Nature Nanotechnology*, 2(3):176–179, 2007.
- [51] Y. Tsujia, A. Staykova, and K. Yoshizawa. Orbital control of the conductance photoswitching in diarylethene. *J. Phys. Chem. C*, 113(52):21477–21483, 2009.
- [52] T. Markussen, J. Schiötz, and K. S. Thygesen. Electrochemical control of quantum interference in anthraquinone-based molecular switches. *J. Chem. Phys.*, 132(22):22104, 2010.
- [53] P. Liljeroth, J. Repp, and G. Meyer. Current-induced hydrogen tautomerization and conductance switching of naphthalocyanin molecules. *Science*, 317(5842):1203–1206, 2007.
- [54] D. Q. Andrews, G. C. Solomon, R. P. Van Duyne, and M. A. Ratner. Single molecule electronics: Increasing dynamic range and switching speed using cross-conjugated species. *J. Am. Chem. Soc.*, 130(51):17309–17319, 2008.
- [55] D. Wei, Y. Liu, L. Cao, Y. Wang, H. Zhang, and G. Yu. Real time and *In Situ* control of the gap size of nanoelectrodes for molecular devices. *Nano. Lett.*, 8(6):1625–1630, 2008.



- [56] T. B. Martins, A. Fazzio, and A. J. R. da Silva. Organic molecule assembled between carbon nanotubes: A highly efficient switch device. *Phys. Rev. B*, 79(11):115413, 2009.
- [57] L. Grill. Functionalized molecules studied by stm: Motion, switching and reactivity. *J. Phys. : Condes. Matter*, 20(5):053001, 2008.
- [58] Y. Nakamura, N. Aratani, H. Shinokubo, A. Takagi, T. Kawai, T. Matsumoto, Z. S. Yoon, D. Y. Kim, T. K. Ahn, D. Kim, A. Muranaka, N. Kobayashi, and A. Osuka. A directly fused tetrameric porphyrin sheet and its anomalous electronic properties that arise from the planar cyclooctatetraene core. *J. Am. Chem. Soc.*, 128(12):4119–4127, 2006.
- [59] A. Tsuda and A. Osuka. Fully conjugated porphyrin tapes with electronic absorption bands that reach into infrared. *Science*, 193(5527):79–82, 2001.
- [60] W. A. de Heer. Nanotubes and the pursuit of applications. *MRS Bull.*, 29(4):281–285, 2004.
- [61] M. Burghard and K. Balasubramanian. Chemically functionalized carbon nanotubes. *Small*, 1(2):180–192, 2005.
- [62] D. Tasis, N. Tagmatarchis, A. Bianco, and M. Prato. Chemistry of carbon nanotubes. *Chem. Rev.*, 106(3):1105–1136, 2006.
- [63] M. Prato. Controlled nanotube reactions. *Nature*, 465(7295):172–173, 2010.
- [64] Y.-P. Sun, K. Fu, Y. Lin, and W. Huang. Functionalized carbon nanotubes: Properties and applications. *Acc. Chem. Res.*, 35(12):1096–1104, 2002.
- [65] C. A. Dyke and J. M. Tour. Covalent functionalization of single-walled carbon nanotube for materials applications. *J. Phys. Chem. A*, 108(51):11151–11159, 2004.
- [66] Y.-S. Lee and N. Marzari. Band structure and quantum conductance of nanostructures from maximally localized wannier functions: The case of functionalized carbon nanotubes. *Phys. Rev. Lett.*, 95(7):076804, 2005.
- [67] A. Lopez-Bezanilla, F. Triozon an dS. Latil, X. Blase, and S. Roche. Effect of the chemical functionalization on charge transport in carbon nanotubes at the mesoscopic scale. *Nano. Lett.*, 9(3):940–944, 2009.
- [68] K. Kamaras, M. E. Itkis, H. Hu, B. Zhao, and R. C. Haddon. Covalent bond formation to a carbon nanotube metal. *Science*, 301(5639):1501, 2003.
- [69] M. S. Strano, C. A. Dyke, M. L. Usrey, P. W. Barone, M. J. Allen, H. Shan, C. Kittrell, R. H. Hauge, J. M. Tour, and R. E. Smalley. Electronic structure control of single-walled carbon nanotube functionalization. *Science*, 301(5639):1519–1522, 2003.

- [70] C. Klinke, J. B. Hannon, A. Afzali, and P. Avouris. Field-effect transistors assembled from functionalized carbon nanotubes. *Nano. Lett.*, 6(5):906–910, 2006.
- [71] M. Kanungo, H. Lu, G. G. Malliaras, and G. B. Blanchet. Suppression of metallic conductivity of single-walled carbon nanotubes by cycloaddition reactions. *Science*, 323(5911):234–237, 2009.
- [72] Y.-S. Lee and N. Marzari. Cycloaddition functionalizations to preserve or control the conductance of carbon nanotubes. *Phys. Rev. Lett.*, 97(11):116801, 2006.
- [73] B. R. Goldsmith, J. G. Coroneus, V. R. Khalap, A. A. Kane, G. A. Weiss, and P. G. Collins. Conductance-controlled point functionalization of single-walled carbon nanotubes. *Science*, 315(5808):77–81, 2007.
- [74] Y.-S. Lee and N. Marzari. Cycloadditions to control bond breaking in naphthalenes, fullerenes, and carbon nanotubes: A first-principles study. *J. Phys. Chem. C*, 112(12):4480–4485, 2008.
- [75] L. T. Scott, M. J. Cooney, C. Otte, C. Puls, T. Haumann, R. Boese, P. J. Carroll, A. B. Smith, and A. de Meijere. Enhancement of through-space and through-bond  $\pi$ -orbital interactions - syntheses and properties of permethylated and perspirocyclopropanated cyclotetradeca-1,3,6,9,12-pentayne. *J. Am. Chem. Soc.*, 116(22):10275–10283, 1994.
- [76] M. Eiermann, R. C. Haddon, B. Knight, Q. C. Li, M. Maggini, N. Martin, T. Ohno, M. Prato, T. Suzuki, and F. Wudl. Electrochemical evidence for through-space orbital interactions in spiromethanofullerenes. *Angew. Chem. Int. Ed. Engl.*, 34(15):1591–1594, 1995.
- [77] M. Keshavarz-K, B. Knight, R. C. Haddon, and F. Wudl. Linear free energy relation of methanofullerene c61-substituents with cyclic voltammetry: Strong electron withdrawal anomaly. *Tetrahedron*, 52(14):5149–5159, 1996.
- [78] B. Knight, N. Martin, T. Ohno, E. Orti, C. Rovira, J. Veciana, J. Vidal-Gancedo, P. Viruela, R. Viruela, and F. Wudl. Synthesis and electrochemistry of electronegative spiroannulated methanofullerenes: Theoretical underpinning of the electronic effect of addends and a reductive cyclopropane ring-opening reaction. *J. Am. Chem. Soc.*, 119(41):9871–9882, 1997.
- [79] F. Diederich and C. Thilgen. Covalent fullerene chemistry. *Science*, 271(5247):317–323, 1996.
- [80] C. H. Choi and M. Kertesz. New interpretation of the valence tautomerism of 1,6-methano[10]annulenes and its application to fullerene derivatives. *J. Phys. Chem. A*, 102(19):3428–3437, 1998.

- [81] H. F. Bettinger. Addition of carbenes to the sidewalls of single-walled carbon nanotubes. *Chem. Eur. J.*, 12(16):4372–4379, 2006.
- [82] Y.-S. Lee. *Electronic Structure and Quantum Conductance of Nanostructures*. PhD thesis, Massachusetts Institute of Technology, Cambridge, Massachusetts, 2006.
- [83] K. S. Coleman, S. R. Bailey, S. Fogden, and M. L. H. Green. Functionalization of single-walled carbon nanotubes *via* the Bingel reaction. *J. Am. Chem. Soc.*, 125(29):8722, 2003.
- [84] N. L. Doltsinis and D. Marx. Nonadiabatic car-parrinello molecular dynamics. *Phys. Rev. Lett.*, 88(16):166402, 2002.
- [85] J. Handta, T. Kunertb, and R. Schmidt. Fragmentation and cis-trans isomerization of diimide in fs laser-pulses. *Chem. Phys. Lett.*, 428(1), 2006.
- [86] M. Ben-Nun and T. J. Martinez. Photodynamics of ethylene: *Ab Initio* studies of conical intersections. *Chem. Phys.*, 259(2), 2000.
- [87] Z. Wu, Z. Chen, X. Du, J. M. Logan, J. Sippel, M. Nikolou, K. Kamaras, J. R. Reynolds, D. B. Tanner, A. F. Hebard, and A. G. Rinzler. Transparent, conductive carbon nanotube films. *Science*, 305(5868):1273–1276, 2005.
- [88] E. Artukovic, M. Kaempgen, D. S. Hecht, S. Roth, and G. Gruner. Transparent and flexible carbon nanotube transistors. *Nano. Lett.*, 5(4):757–760, 2005.
- [89] J. Li, L. Hu, L. Wang, Y. Zhou, G. Gruner, and T. J. Marks. Organic light-emitting diodes having carbon nanotube anodes. *Nano. Lett.*, 6(11):2472–2477, 2006.
- [90] G. Gruner. Carbon nanotube films for transparent and plastic electronics. *J. Mater. Chem.*, 16(35):3533–3539, 2006.
- [91] M. A. Meitl, Y. Zhou, A. Gaur, S. Jeon, M. L. Ursey, M. S. Strano, and J. A. Rogers. Solution casting and transfer printing single-walled carbon nanotube films. *Nano. Lett.*, 4(9):1643–1647, 2004.
- [92] E. Bekyarova, M. E. Itkis, N. Cabrera, B. Zhao, A. Yu, J. Gao, and R. C. Haddon. Electronic properties of single-walled carbon nanotube networks. *J. Am. Chem. Soc.*, 127(16):5990–5995, 2005.
- [93] S. I. Cha, K. T. Kim, K. H. Lee, C. B. Mo, Y. J. Jeong, and S. H. Hong. Mechanical and electrical properties of cross-linked carbon nanotubes. *Carbon*, 46(3):482–488, 2008.
- [94] Y. Ma, W. Cheung, D. Wei, A. Bogozi, P. L. Chiu, L. Wang, F. Pontoriero, A. Mendelsohn, and H. He. Improved conductivity of carbon nanotube networks by *In Situ* polymerization of a thin skin of conducting polymer. *ACS Nano*, 2(6):1197–1204, 2008.

- [95] M.-C. Hermant, P. van der Schoot, B. Klumperman, and C. E. Koning. Probing the cooperative nature of the conductive components in polystyrene/poly(3,4-ethylenedioxythiophene): Poly(styrene sulfonate)-single-walled carbon nanotube composites. *ACS Nano*, 4(4):2242–2248, 2010.
- [96] S.-H. Ke, H. U. Baranger, and W. Yang. Contact transparency of nanotube-molecule-nanotube junctions. *Phys. Rev. Lett.*, 99(14):146802, 2007.
- [97] Z. Qian, S. Hou, J. Ning, R. Li, Z. Shen, X. Zhao, and Z. Xue. First-principles calculation on the conductance of a single 1,4-diisocyanatobenzene molecule with single-walled carbon nanotubes as the electrodes. *J. Chem. Phys.*, 126(8):084705, 2007.
- [98] N. A. Bruquel and M. K. Ashraf, G. J. O. Beran, T. R. Helander, and R. K. Lake. Conductance of a conjugated molecule with carbon nanotube contacts. *Phys. Rev. B*, 80(15):155455, 2009.
- [99] P. Qi, A. Javey, M. Rolandi, Q. Wang, E. Yenilmez, and H. Dai. Miniature organic transistors with carbon nanotubes as quasi-one-dimensional electrodes. *J. Am. Chem. Soc.*, 126(38):11774–11775, 2004.
- [100] S. A. Getty, C. Engtrakul, L. Wang, R. Liu, S.-H. Ke, H. U. baranger, W. Yang, M. S. Fuhrer, and L. R. Sita. Near-perfect conduction through a ferrocene-based molecular wire. *Phys. Rev. B*, 71(24):241401, 2005.
- [101] S. Banerjee and S. S. Wong. Functionalization of carbon nanotubes with a metal-containing molecular complex. *Nano. Lett.*, 2(1):49–53, 2002.
- [102] S. Banerjee and S. S. Wong. Structural characterization, optical properties, and improved solubility of carbon nanotubes functionalized with wilkinson’s catalyst. *J. Am. Chem. Soc.*, 124(30):8940–8948, 2004.
- [103] S. Banerjee and S. S. Wong. Selective metallic tube reactivity in the solution-phase osmylation of single-walled carbon nanotubes. *J. Am. Chem. Soc.*, 126(7):2073–2081, 2004.
- [104] F. Nunzi, F. Mercuri, and A. Sgamellotti. The coordination chemistry of carbon nanotubes: a density functional study through a cluster model approach. *J. Phys. Chem. B*, 106(41):10622–10633, 2002.
- [105] F. Nunzi, F. Mercuri, F. De Angelis, A. Sgamellotti, N. Re, and P. Giannozzi. Coordination and haptotropic rearrangement of  $\text{Cr}(\text{CO})_3$  on  $(n,0)$  nanotube side-walls: A dynamical density functional study. *J. Phys. Chem. B*, 108(17):5243–5249, 2004.
- [106] F. Mercuri and A. Sgamellotti. Functionalization of carbon nanotubes with vaska’s complex: A theoretical approach. *J. Phys. Chem. B*, 110(31):15291–15294, 2006.

- [107] E. Durgun, S. Dag, V. M. K. Bagci, O. Gülseren, T. Yildirim, and S. Ciraci. Systematic study of adsorption of single atoms on a carbon nanotube. *Phys. Rev. B*, 67(20):201401, 2003.
- [108] V. Georgakilas, D. Gournis, V. Tzitzios, L. Pasquato, D. M. Guldi, and M. Prato. Decorating carbon nanotubes with metal or semiconductor nanoparticles. *J. Mater. Chem.*, 17(26):2679–2694, 2007.
- [109] G. W. Wildgoose, C. E. Banks, and R. G. Compton. Metal nanoparticles and related materials supported on carbon nanotubes: Methods and applications. *Small*, 2(2):182–193, 2006.
- [110] Y.-S. Min, E. J. Bae, U. J. Kim, E. H. Lee, N. Park, C. S. Hwang, and W. Park. Unusual transport characteristics of nitrogen-doped single-walled carbon nanotubes. *Appl. Phys. Lett.*, 93(4):043113, 2008.
- [111] Y. Shang, J.-X. Zhao, H. Wu, Q.-H. Cai, X.-G. Wang, and X.-Z. Wang. Chemical functionalization of pyridine-like and porphyrin-like nitrogen-doped carbon (cnx) nanotubes with transition metal (tm) atoms: a theoretical study. *Theor. Chem. Acc.*, 127(5):727–733, 2010.
- [112] K. Xiao, Y. Q. Lui, P. A. Hu, G. Yu, W. P. Hu, D. B. Zhu, X. Y. Liu, H. M. Liu, and D. X. Wu. Electronic transport characteristic of an individual cnx/c nanotube schottky junction. *Appl. Phys. A*, 83(1):53–56, 2006.